Orbital Signatures of Ultralight Scalars in Binary Black Holes

Dissertation
zur Erlangung des Doktorgrades
an der Fakultät für Mathematik, Informatik und Naturwissenschaften
Fachbereich Physik
der Universität Hamburg

vorgelegt von

Matthias Koschnitzke

Hamburg
2025

Declaration of Authorship/ Eidesstattliche Versicherung

Hiermit versichere ich an Eides statt, die vorliegende Dissertationsschrift selbst verfasst und keine anderen als die angegebenen Hilfsmittel und Quellen benutzt zu haben. Sofern im Zuge der Erstellung der vorliegenden Dissertationsschrift generative Künstliche Intelligenz (gKI) basierte elektronische Hilfsmittel verwendet wurden, versichere ich, dass meine eigene Leistung im Vordergrund stand und dass eine vollständige Dokumentation aller verwendeten Hilfsmittel gemäß der Guten wissenschaftlichen Praxis vorliegt. Ich trage die Verantwortung für eventuell durch die gKI generierte fehlerhafte oder verzerrte Inhalte, fehlerhafte Referenzen, Verstöße gegen das Datenschutz- und Urheberrecht oder Plagiate.

Unterschrift des Doktoranden:

Ort, Datum:

Gutachter/innen der Dissertation:	Prof. Dr. Géraldine Servant Dr. Rafael A. Porto
Zusammensetzung der Prüfungskommission:	Prof. Dr. Oliver Gerberding Dr. Hyungjin Kim Prof. Dr. Jochen Liske Dr. Rafael A. Porto Prof. Dr. Géraldine Servant
Vorsitzende/r der Prüfungskommission:	Prof. Dr. Jochen Liske
Datum der Disputation:	08.09.2025
Vorsitzender des Fach-Promotionsausschusses PHYSIK:	Prof. Dr. Wolfgang J. Parak
Leiter des Fachbereichs PHYSIK:	Prof. Dr. Markus Drescher
Dekan der Fakultät MIN:	Prof. Dr.-Ing. Norbert Ritter

"*Oh my god particle! [...] You can tell your grandchildren you were here when humanity finally learned that this accelerator is much too small to tell us anything important.*"

- Professor John Frink Jr.

Abstract

Matthias Koschnitzke

Orbital Signatures of Ultralight Scalars in Binary Black Holes

We extend the study of black hole superradiance in binary systems, also known as gravitational atomic physics, to include eccentric and inclined orbits. Such systems exhibit Landau-Zener-like transitions between bound states of the bosonic cloud. We uncover new resonance phenomena, such as early and late resonances, which can grow orbital eccentricity and leave measurable imprints on gravitational-wave signals.

To model dynamically formed binaries whose orbital angular momentum is misaligned with the spin of the central black hole, we develop a framework based on Hamiltonian mechanics that couples the full orbital dynamics to the bosonic cloud via multipole interactions. This method resolves limitations of previous balance-law approaches and reveals novel dynamics such as floating on counter-rotating orbits and overlapping resonances. For the first time, we also include non-resonant mixing with states that decay back into the black hole, showing how this alters resonance conditions and suppresses perfect floating, while still leaving significant orbital signatures.

For masses of scalar particles from $\sim 10^{-13}$ to 10^{-11} eV, these dynamics leave observable signatures on binary black hole populations, particularly at gravitational-wave frequencies accessible to upcoming detectors such as the Laser Interferometer Space Antenna LISA, as well as future mid-band and decihertz detectors.

Zusammenfassung

Matthias Koschnitzke

Orbital Signatures of Ultralight Scalars in Binary Black Holes

Wir erweitern die Untersuchung der Superradianz von Schwarzen Löchern in Binärsystemen, auch bekannt als gravitationale Atomphysik, auf exzentrische und geneigte Umlaufbahnen. Solche Systeme zeigen Landau-Zener-ähnliche Übergänge zwischen gebundenen Zuständen der bosonischen Wolke. Wir identifizieren neue Resonanzphänomene, wie frühe und späte Resonanzen, die die Bahnexzentrizität anwachsen lassen und messbare Spuren im Gravitationswellensignal hinterlassen können.

Zur Modellierung dynamisch entstandener Binärsysteme, bei denen der Bahndrehimpuls nicht parallel zur Rotationsachse des zentralen Schwarzen Lochs ausgerichtet ist, entwickeln wir einen Formalismus auf Basis der Hamiltonschen Mechanik, der die vollständige Dynamik des Orbits über Multipolwechselwirkungen mit der bosonischen Wolke koppelt. Diese Methode überwindet Einschränkungen früherer Energie- und Impulsbilanzansätze und offenbart neuartige Dynamiken wie das „Floating“ auf anti-parallen Ausrichtungen des Orbits, sowie überlappende Resonanzen. Erstmals berücksichtigen wir auch nicht-resonante Übergänge zwischen den Zuständen, die dabei wieder in das Schwarze Loch zurückfallen. Das beeinflusst die Resonanzbedingungen, unterdrückt perfektes Floating und hinterlässt dennoch signifikante Signaturen in den Bahneigenschaften.

Für skalare Teilchen mit Massen im Bereich von etwa 10^{-13} bis 10^{-11} eV hinterlassen diese Dynamiken beobachtbare Spuren in Populationen von binären Schwarzen Löchern, insbesondere bei Gravitationswellenfrequenzen, die mit zukünftigen Detektoren wie der Laser Interferometer Space Antenna LISA, sowie geplanten Mid-Band- und Deci-Hertz-Detektoren zugänglich sein werden.

Publications and Contributions

The research presented in this thesis is based on the work I have done during the time as PhD-student at the University of Hamburg and DESY under the supervision of Dr. Rafael A. Porto (DESY). Ch. 5 and Ch. 6 of this thesis contains material included in the following publication:

- Mateja Bošković, Matthias Koschnitzke, Rafael A. Porto: **"Signatures of ultralight bosons in the orbital eccentricity of binary black holes"**, *Phys.Rev.Lett. 133 (2024) 12, 12* [arXiv: 2403.02415] [1]

The following are papers I worked on during my PhD with topics distinct from the main focus of my PhD research and are therefore not included in this thesis:

- Aleksandr Chatrchyan, Cem Eröncel, Matthias Koschnitzke, Géraldine Servant: **"ALP dark matter with non-periodic potentials: parametric resonance, halo formation and gravitational signatures"**, *JCAP 10 (2023) 068* [arXiv: 2305.03756] [2]
- HECAP+ Initiative: **"Environmental sustainability in basic research: a perspective from HECAP+"**, *JINST 20 (2025) P03012* [arXiv: 2306.02837] [3]

Author's Contributions. In the following I declare my contributions to the results presented in this thesis, which are based on the collaborative work with Mateja Bošković (MB) and Rafael A. Porto (RAP).

The general idea to study eccentric orbits in the context of superradiance in BBHs was proposed by RAP, who realized that this will lead to additional overtones. I was taking part in the discussions that improved the theoretical understanding of the project during the entire time, which among others led to the discovery of the fixed points. Many of the analytic results and estimates presented in Ch. 5 were derived by MB, who also produced the figures in that chapter. The population study from Ch. 6, which includes setting up the population, programming the *Mathematica* notebook for the pipeline evolving individual binaries through the resonances, was carried out by me. Consequentially, I produced all the figures in that chapter with the exception of Fig. 6.7.

While the idea to use Lagrange's equations to describe the orbital parameters of the BBHs for inclined orbits presented in Ch. 7 came from MB, who also worked out the details of how to use the worldline EFT approach, I actively contributed to the theoretical discussions and was responsible for identifying that counter-rotating orbits can also experience fine resonances. I implemented all the numerical simulations of non-eccentricity-expanded inclined orbits in time- and frequency-space using *Python*, and produced all the figures in Ch. 7 and Ch. 8.

Notations and Conventions

We work, unless otherwise stated, in *natural units*, where we set the speed of light in vacuum and the reduced Planck constant to unity, i.e.

$$c_0 = \hbar = 1\,,$$

such that the only base quantity becomes energy, usually given in electronvolt (eV) or GeV $= 10^9$ eV. For this page, we keep factors of c_0 and $\hbar$ explicit and give comparisons between values in S.I. units and natural units.

We will keep Newton's gravitational constant G explicit. This constant is related to the definition of the Planck mass $M_{\rm pl}$ by [4]

$$G \equiv \frac{\hbar c_0}{M_{\rm pl}^2} = 6.674 \times 10^{-11}\,\frac{\rm m^3}{\rm kg\,s^2} = 6.709 \times 10^{-39}\,\frac{\hbar c_0^5}{\rm GeV^2}\,.$$

One of the most important quantities will be the gravitational radius $r_g \equiv GM/c_0^2$ of a black hole of mass M. For a black hole with the mass of the Sun

$$M_\odot = 1.989 \times 10^{31}\,{\rm kg} = 1.116 \times 10^{57}\,\frac{\rm GeV}{c_0^2}$$

this is

$$r_{g,\odot} \equiv \frac{GM_\odot}{c_0^2} = 1.477\,{\rm km} = 7.49 \times 10^{18}\,\frac{\hbar c_0}{\rm GeV}\,.$$

A common system of units used in general relativity are *geometrized units*, where $G = c_0 = 1$, but $\hbar \neq 1$. In these, the only base unit is length, usually given in cm. A black hole mass then becomes equivalent to its gravitational radius, while particle masses are usually given in terms of their inverse Compton wavelength

$$1\,{\rm eV}|_{\hbar=c_0=1} \cong 5.069 \times 10^4\,{\rm cm^{-1}}\big|_{G=c_0=1}\,.$$

List of Abbreviations

ALP	**A**xion-**L**ike **P**article
BBH	**B**inary **B**lack **H**ole
BH	**B**lack **H**ole
com	**c**entre **o**f **m**ass
CP	**C**harge and **P**arity
DECIGO	**Dec**i-hertz **I**nterferometer **G**ravitational-Wave **O**bservatory
eom	**e**quation **o**f **m**otion
EFT	**E**ffective **F**ield **T**heory
EMRI	**E**xtreme **M**ass **R**atio **I**nspiral
ET	**E**instein **T**elescope
GA	**G**ravtiational **A**tom
GR	**G**eneral Theory of **R**elativity
GUT	**G**rand **U**nified **T**heory
GW	**G**ravitational **W**ave
IAA	**I**solated **A**tom **A**pproach
IPTA	**I**nternational **P**ulsar **T**iming **A**rray
ISCO	**I**nnermost **S**table **C**ircular **O**rbit
LHC	**L**arge **H**adron **C**ollider
LIGO	**L**aser **I**nterferometer **G**ravitational-Wave **O**bservatory
LISA	**L**aser **I**nterferometer **S**pace **A**ntenna
LZ	**L**andau-**Z**ener
ODE	**o**rdinary **d**ifferential **e**quation
PBH	**P**rimordial **B**lack **H**ole
PN	**P**ost **N**ewtonian
pNGB	**p**seudo-**N**ambu **G**oldstone **B**oson
PQ	**P**eccei and **Q**uinn
RR	**R**adiation **R**eaction
QCD	**Q**uantum **C**hromo**d**ynamics
SM	**S**tandard **M**odel of Particle Physics
STF	**s**ymmetric (&) **t**race-**f**ree
UV	**U**ltra**v**iolet

Contents

List of Figures

Chapter 1 Invitation and Outline

When the LIGO and Virgo collaborations discovered the gravitational wave (GW) signal of a merging binary black hole (BBH) in September of 2015 [5, 6], it marked nothing less than the beginning of a new era in astrophysics. Observing the sky via detection of GWs opens an entirely new window into the cosmos, bringing phenomena into reach that are not observable via electromagnetic radiation, and also makes multi-messenger astronomy, observing events in both electromagnetic and gravitational waves, possible.
While the first generation of GW observatories can only observe the merger-phase of stellar mass BBHs, planned future observatories like the Laser Interferometer Space Antenna (LISA) [7], Einstein Telescope (ET) [8, 9], Cosmic Explorer (CE) [10], as well as other Mid-band [11] and decihertz detectors [12], will be able to observe more of the history of the binaries due to the extension of the sensitivity to lower frequencies and lower GW strain [5, 8]. This will make it possible to use the observation of the inspiral phase of BBHs, binaries of a black hole (BH) and a neutron star, or neutron star binaries to test, among others, general relativity, modifications thereof, tidal deformation effects, the equation-of-state of neutron stars and to better understand astrophysical environments [13]. Perhaps less obviously, but no less intriguingly, BBHs can also be testing facilities for beyond Standard Model particles, which is the topic of this thesis.

The Standard Model of particle physics, which has been observationally completed by the 2012 discovery of the Higgs boson at the Large Hadron Collider (LHC) at CERN [14, 15], has been extremely successful in predicting almost all physical, non-gravitational processes we observe, from astrophysical to microscopic scales. And yet it is agreed upon that it must be incomplete, since it cannot integrate gravity, explain neutrino masses [16, 17], the only-gravitationally-observed dark matter [18], dark energy [19], and gives rise to conceptual problems like the strong CP problem, the cosmological constant problem [20], the naturalness/hierarchy problem of the Higgs [21], as well as a seemingly metastable state of the Higgs vacuum [22]. Since the experiments at the LHC so far gave no hint towards the viability of supersymmetric theories, in which the lightest neutral supersymmetric particles would be natural dark matter candidates [23], light scalar particles, like the QCD-axion or other axion-like-particles (ALPs), have gotten a lot of attention as possible dark matter candidates. Among other reasons this is due to the prediction of an abundance of ALPs in the low energy effective theories arising from string theory [24].

If the spectrum of nature contains fundamental low-mass (but not massless) scalar or vector particles, they can be bound to a rotating BH in hydrogen-like states and amplified via the *superradiant instability*, resulting in a dense cloud of these bosons around the BH, both together forming a *gravitational atom*. If a BH in a binary carries such a cloud, the tidal forces introduced by the companion can give rise to a plethora of effects that change the state of the cloud as well as the parameters of the orbit. The main process here is that the oscillatory perturbation of the second object causes transitions between the discrete energy states of the cloud, resonantly or non-resonantly.

If the bosonic cloud changes the history of the inspiral of BBHs significantly, it will be directly imprinted into the GW signal. This gives rise to the fascinating opportunity to learn via GW astrophysics about particles that could be impossible to investigate experimentally on Earth.

The topic of this thesis is first to show how resonant effects of the bosonic clouds that have been missed under simplified assumptions of the orbits can drastically influence the dynamics of the orbit, and second to provide steps towards building a consistent theoretical framework to understand these effects for general BBH orbits, which, as we will show, has not been done coherently in the existing literature. We will provide some robust phenomenological aspects for important and specific cases.

The outline of this thesis is the following:

- Part 1 acts as an introduction. We give an overview of the theoretical motivations of ultralight scalars in Ch. 2. Ch. 3 gives a brief theoretical overview over BH superradiance in isolated BHs. For the basics of superradiance in binary BHs given in Ch. 4, we follow the chronology of the phenomenon's investigation from the erroneous idea of Rabi oscillations [25] to Landau-Zener transitions in equatorial and circular orbits [26], as well as to ionization [27], i.e., transitions to unbound states.

- Part 2, continuing the chronological approach, covers the extension of the previous results to incorporate eccentric, but still equatorial, orbits and corresponding phenomenological consequences. Also for the first time, we take into account that the state the cloud transfers to is actually decaying. This part is adapted from work previously published by the author and collaborators as Ref. [1].

- Part 3 applies Hamiltonian mechanics to treat the interaction of the binary companion and the gravitational atom for general orbits, where spin of the gravitational atom and the orbit are misaligned. We develop a fully self-consistent formalism that is readily applicable for more detailed studies in the future, and also investigate, why previous approaches have produced erroneous results for general orbits in Ch. 7. In Ch. 8, we study the most important aspects of the dynamics of the system when all orbital parameters are considered, and also incorporate non-resonant, perturbative mixing with strongly decaying states, which challenges all former results on superradiance in BBHs, including the ones in Ref. [1]. This part contains content to appear in Ref. [28].

- Part 4 consists solely of Ch. 9, in which we summarize the results, draw conclusions and give an outlook by discussing open questions and further directions for BH superradiance in binaries.

Part I

Introduction

Chapter 2 Ultralight Scalars

This chapter is going to provide an overview over the motivations to study ultralight scalar particles like the QCD-axion and axion-like-particles (ALPs). While the details of this chapter are not needed to study BH superradiance of ultralight particles, it helps us understand the recent surge in research interest. To this day, the lightest known bosonic particle is the pion. The Compton wavelength of pions is many orders of magnitude smaller than the horizon radius of stellar mass BHs. Hence, when BH superradiance of massive bosonic particles was first studied, researchers speculated that bosonic clouds, made of pions, could be found only around low mass primordial black holes (PBHs) [29, 30] or when stellar mass BHs have lost most of their mass through Hawking radiation [31, 32]. Because PBHs are still a vital area of research, the discussion of BH superradiance of ultralight particles also led to a resurgence of pion superradiance [33].

The *QCD-axion*, as the prototypical ultralight scalar particle, has been known since the late 1970s and identified as a valid dark matter candidate in the early 1980s [34–36]. However, the realization that compactifications in string theory naturally gives rise to many ALPs with different masses, colloquially referred to as the *string-axiverse*, has resurrected the interest in BH superradiance [24, 37], because BH superradiance gives rise to the opportunity to link an observable parameter, i.e., the spin of BHs, to particles that could be impossible to probe with experiments on Earth due to their weak interactions.

2.1 The Strong CP Problem and Axions

The Standard Model of particle physics (SM) is a non-abelian quantum field theory with gauge group $SU(3)_c \times SU(2)_L \times U(1)_Y$. It unifies Quantum Chromodynamics (QCD) describing the strong interaction and electroweak theory which governs weak and electromagnetic interactions. One of the most important unsolved problems of the SM is the *strong CP problem* of QCD. The non-trivial vacuum structure of QCD is due to the existence of pure gauge field configurations $|n\rangle$, i.e., zero-energy solutions, that differ by their topological integer winding number n. Non-perturbative solutions called instantons mediate tunneling between these vacua. This implies that the physical QCD vacuum necessarily must be a superposition of all topological sectors, the θ-vacuum $|\theta\rangle \equiv e^{n\theta_{\mathrm{QCD}}} |n\rangle$, where θ_{QCD} in principle is a free parameter. Due to this structure, one finds in the path integral formalism that the effective QCD Lagrangian density includes the

so-called θ-term [38, 39]:

$$\mathcal{L}_{\theta_{\rm QCD}} = \frac{\theta_{\rm QCD}}{32\pi^2}{\rm Tr}\left[G_{\mu\nu}\tilde{G}^{\mu\nu}\right] , \tag{2.1}$$

where $G_{\mu\nu}$ is the gluon field strength tensor and $\tilde{G}^{\mu\nu} \equiv \epsilon^{\mu\nu\alpha\beta}G_{\alpha\beta}/2$ is its dual. The θ-term violates charge and parity (CP) symmetry, and gives rise to an electric dipole moment of the neutron [40]:

$$d_n \approx 3.6 \times 10^{-16}\theta_{\rm QCD} e\,{\rm cm}\,, \tag{2.2}$$

where e is the charge of the electron. The experimental constraint $|d_n| < 2.9 \times 10^{-26} e\,{\rm cm}$ [41] implies $\theta_{\rm QCD} \lesssim 10^{-10}$. If at least one of the quarks were massless, we could perform a chiral rotation on that massless quark to remove $\theta_{\rm QCD}$ entirely from the Lagrangian, since there is no mass term to pick up a complex phase. In this case, $\mathcal{L}_{\theta_{\rm QCD}}$ would become unphysical. However, since all quarks are massive, such chiral rotations shift the phase into the quark mass matrix, and the relevant physical quantity is actually the sum of the free parameter from the QCD-vacuum $\bar{\theta}$ and the phase of the quark mass matrices. To go to a physical basis in the full electroweak theory, one must diagonalize the quark mass matrix via a chiral transformation. This renders the physical relevant $\theta_{\rm QCD}$ to be

$$\theta_{\rm QCD} \to \bar{\theta}_{\rm QCD} + \arg\det\left[M_u M_d\right] . \tag{2.3}$$

Unless one of the quarks would be actually massless, it cannot be explained why these two unrelated terms coming from different sectors of the theory should cancel to almost zero, and therefore a fine-tuning problem arises, called the strong CP problem.

By far the most prominent solution was introduced by Peccei and Quinn Ref. [42]. They proposed a new global U(1)-symmetry that is spontaneously broken and renders $\theta_{\rm QCD}$ to be dynamically driven to zero. Weinberg and Wilczek realized that this breaking gives rise to a Nambu-Goldstone boson, the *axion* [43, 44].[I] In the the original Peccei-Quinn-Weinberg-Wilczek (PQWW) model, one assumes that the full Lagrangian is to be taken invariant under a global chiral $\mathrm{U}(1)_{\rm PQ}$ symmetry. Here, ϕ gives masses to the fermions via the standard Brout-Englert-Higgs mechanism [45, 46]. The invariance of ϕ under $\mathrm{U}(1)_{\rm PQ}$ rotations then fixes the PQ charges of the fermions [47]. The PQ symmetry is spontaneously broken below the energy scale f_a. The axion, being the pseudo Nambu-Goldstone boson of this broken symmetry, couples to the SM via the PQ charges and the chiral PQ rotations. The latter shifts the angular part of ϕ by a constant. While the axion classically possesses a shift symmetry, these chiral rotation changes the path integral measure and hence QCD has a so-called *chiral anomaly*. This induces couplings of the axion a to the gauge bosons. With that, the part of the Lagrangian including $\theta_{\rm QCD}$ and the axion becomes [48]

$$\mathcal{L}_{\theta_{\rm QCD}+a} = \frac{\theta_{\rm QCD}}{32\pi^2}{\rm Tr}G_{\mu\nu}\tilde{G}^{\mu\nu} - \frac{1}{2}\partial_\mu a \partial^\mu a + \mathcal{L}\left[\partial^\mu a/f_a;\Psi\right] + \xi\frac{a}{f_a}g^2 32\pi^2 {\rm Tr}G_{\mu\nu}\tilde{G}^{\mu\nu}\,, \tag{2.4}$$

where $\mathcal{L}\left[\partial^\mu a/f_a;\Psi\right]$ denotes the interaction terms between axions and fermions, e.g., derivative

[I] The axion has been named by Frank Wilczek after a laundry detergent, metaphorically cleaning up the strong CP problem.

couplings to axial currents, and $\xi = 1$ in the PQWW-model. In the low energy limit of QCD, using the chiral Lagrangian, it can be shown that the instanton-related terms in Eq. (2.4) give rise to an effective axion potential that is invariant under $a \to a + 2\pi f_a$ [48]:

$$V_{\text{eff}} \sim \cos\left(\theta_{\text{QCD}} + \xi \frac{a}{f_a}\right) . \tag{2.5}$$

Minimizing this potential with respect to a gives

$$a_{\text{min}} = -\theta_{\text{QCD}} \frac{f_a}{\xi} . \tag{2.6}$$

Redefining the physical axion field to $a_{\text{phy}} = a_{\text{min}} - a$, one gets rid of the θ_{QCD} term in Eq. (2.4) and this solves the strong CP problem [48]. One says that the axion field dynamically drives the value of θ_{QCD} to zero [47]. The effective potential for the axion gives also rise to a mass for the axion which scales as

$$m_a \sim \frac{\Lambda_{\text{QCD}}^4}{f_a^2}, \tag{2.7}$$

where $\Lambda_{\text{QCD}} \approx 200\,\text{MeV}$ is the confinement scale of QCD.

In this original PQWW-model, the axion was the angular degree of freedom of an additional Higgs doublet ϕ, so this rendered the scale of the symmetry breaking f_a to be of the order of the electroweak scale [47]. This made it possible to excluded this model by experiments. However, there are viable axion models with a larger breaking scale, called *invisible axions*, which also solve the strong CP problem, but that are not experimentally excluded. Examples are the Kim-Shifman-Vainshtein-Zakharov (KSVZ) model [49, 50], which features the introduction of additional heavy quarks to which the scalar field ϕ couples. The Dine-Fischler-Srednicki-Zhitnitsky (DFSZ) model [51, 52] in turn contains two Higgs doublets and the scalar field ϕ, where the latter gives rise to the axion. In both of these models, f_a is a free parameter and therefore both models are still not excluded by experiments in a large part of the possible parameter space. Since f_a is usually assumed to be much larger than the QCD confinement scale, this renders the axion to be very light. Soon after the introduction of these models, it was realized that the invisible axions are vital dark matter candidates [34–36], which motivates the ongoing intense research efforts.

2.2 Axion-Like Particles

As we already mentioned, NGBs arise naturally when a global symmetry is spontaneously broken. NGBs that arise from other global symmetries than the PQ symmetry and that not necessarily solve the strong CP problem have been called *axion-like particles (ALPs)* [53]. In these more general models there is no fixed relation between symmetry breaking scale f_a and mass m_a and both can be treated as independent parameters [54].

A strong motivation for the existence of axions and ALPs comes from *String Theory*. String Theory is considered to be a promising theory to describe all known forces, the three forces described

by the SM and gravity, up to arbitrarily high energies.[II] *Superstring Theory* describes both bosons and fermions as excitations of one-dimensional elementary *strings*, but is only consistent in ten space-time dimensions [55, 56], while *M-Theory* is a theory in eleven dimensions [57]. Our physical world only has three large dimensions, so this implies that all but four spacetime dimensions (three space and one time) must be small and compact, in Superstring Theory typically compactified on Calabi-Yau manifolds which preserve supersymmetry in the low-energy 4D theory [58], and as G_2-manifolds in M-Theory [59]. ALPs do not arise directly as fundamental string excitations, but they emerge in the 4D low-energy effective theory from compactification, specifically as Kaluza-Klein zero modes [60, 61], of higher-dimensional gauge or form fields. The latter are themselves low-energy fields arising from the massless modes of string excitations [53].

The ALPs arise when a p-form gauge potential is integrated over a non-trivial p-cycle in the compact manifold. For example [62], in type IIB string theory, axions arise as $b_I = \int_{\Sigma_I^{(2)}} B$, which is the integral of the Neveu-Schwarz two-form potential B_{MN} over two-cycles $\Sigma_I^{(2)}$. By integrating the Ramond-Ramond two-form C_{MN} one similarly finds $c_I = \int_{\Sigma_I^{(2)}} C$. These ALPs also respect a shift symmetry. In general, the symmetry breaking scale f_a of the ALPs arising in String Theory is related to the geometry of the compact manifold in a non-trivial way [63] and the theories predict a wide range of possible values. Typically it is assumed to be near the scale of Grand-Unified-Theories at $f_a \sim 10^{16}\,\text{GeV}$ [64], while lower values of $f_a \sim 10^{10}\,\text{GeV} - 10^{12}\,\text{GeV}$ are also possible [65]. An upper bound is given by the Planck energy scale, i.e., $f_a < M_{\text{Pl}}$ [47, 66]. The number of different axions is related to the topology of the compact dimensions, and it is not uncommon to expect several ALPs [47], possibly also including the QCD-axion described in the last section [64, 67, 68]. The term *string-axiverse* [24, 65, 69, 70] refers to the prediction that many different ALPs could exist, with masses that are roughly distributed evenly on a logarithmic scale.

[II] One says that it is complete in the ultraviolet, i.e., UV-complete.

Chapter 3 Basics of Gravitational Atoms

Rotational superradiant scattering, referred to as *superradiance*, is the process of amplification of waves scattered off a rotating medium that moves faster than the wave's phase velocity and provides a mechanism for dissipation. Through this process, rotational energy is transferred from the medium to the wave. In the case of *black hole (BH) superradiance*, the dissipative medium is the rotating spacetime itself.

The concept of extracting energy from a rotating BH was first proposed by Penrose [71], who showed that a particle entering the ergoregion of a rotating BH can exit with more energy than it had initially, thereby extracting energy and angular momentum from the BH. Zel'dovich first argued [72, 73] that wave amplification could occur when a rotating object, exerting friction or dissipation, scatters incident waves. A rotating BH provides such a medium.

However, for massless fields such as electromagnetic waves, this would result in just a single scattering event. To create a sustained instability, Press and Teukolsky proposed to put a BH inside a reflective cavity, a mirror, confining the scattered waves to the BH and causing repeated superradiant amplification. This theoretical setup has been called a BH-bomb [74].

In contrast, if the field possesses a non-zero mass, the mass itself provides a natural confining potential. This results in a *superradiant instability* which leads to the exponential growth of long-lived bound states around the BH, until the latter has been spun down [32, 74–77]. Because the spectrum of these bound states in the Kerr metric resembles hydrogenic states, these superradiant clouds around BHs are often referred to as *gravitational atoms*.

This chapter gives an overview of the basics of BH superradiance in isolated BHs, while the effects of a companion will be discussed in Ch. 4. The most important results in this chapter will be the energy levels of the superradiant cloud, as well as its growth and decay rates. For completeness, we will also briefly discuss the phenomenological aspects of isolated gravitational atoms.

Superradiant instabilities are also possible for massive vector as well as for tensor fields, which have been studied both analytically and numerically [26, 78–84]. The superradiance rate for vectors is much faster than for scalars, leading to a smaller separation of scales in the full problem, making it easier to study them numerically [85]. Some peculiar results for these include numerical results showing the spherical state of massive tensor fields to be unstable even for Schwarzschild, i.e., non-rotating, BHs [86]. In this thesis, we are only going to focus on superradiance of scalars,

and are not going to include superradiance of vectors and tensors. For a review discussing these, consult Ref. [87].

Another interesting avenue is the possibility of superradiance for scalar fields that allow self-interactions. The latter can induce mixing between the states, changing the evolution of the superradiant state or shutting it of completely if the self-interactions are strong enough. This admits the peculiar effect that while most other experimental or observational constrains rely on self-interactions to be *strong* enough, superradiance has been used to exclude *weak* interactions, because only then the cloud can form and potentially make observation of highly spinning BHs impossible [88–93]. For an introduction to how these exclusions arise, see Sec. 3.5.

If the scalar particle couples to photons, it enables *stimulated emission*, where spontaneous decay into photons can trigger an avalanche effect when the photon triggers new decays before leaving the cloud. The detailed phenomenology of this effect has been controversially discussed under names like *blast* and *burst*, either describing the effect as periodically ramping up superradiance until a strong and short emission of photons happens, or leading to an equilibrium state of constant photon emission and cloud density lower than expected for non-interacting bosons. For details see Refs. [94–99]. In this thesis, we are neither going to take effects of self-interactions, nor effects of coupling to other particles into account, effectively assuming the breaking scale f_a to be close enough to the Planck scale to make these interactions negligible.

3.1 Rotational Superradiance - The Zel'dovich Argument

To build intuition for the phenomenon of superradiance, we begin with a very simple, non-relativistic analogy in one-dimension that still captures the key elements dissipation, motion, and energy transfer: If a person runs and jumps off from the ground with initial horizontal velocity v_i and lands again on a ground that provides some friction, the final velocity v_f will be reduced, $v_f < v_i$. If a person jumps onto a treadmill that runs with velocity v_t in the same direction as the person jumps, but slower than the horizontal initial speed $v_t < v_i$ and provides friction, the treadmill will pull that person back with it, again resulting in $v_f < v_i$. However, when the treadmill runs faster than the initial horizontal speed, $v_t > v_i$, in the rest frame of the running treadmill the person's initial speed will be negative, i.e., $v_i' < 0$. This means, when the person lands, friction will drag the person along and hence make this negative velocity less negative. For a realistic treadmill, it will reduce it to zero in the treadmill's frame. Returning to the "lab"-frame, this leads to $v_f > v_i$. The treadmill is a dissipative medium in the sense that it absorbs kinetic energy of persons landing on it. However, if it moves fast enough, this dissipation actually increases the kinetic energy of the person jumping onto it. The energy increasing the person's speed is provided by the treadmill. See Fig. 3.1 for a visualization.

We can now apply this to a rotating surface and a rotationally symmetric, dissipative field. This is the essence of the Zel'dovich argument given in Ref. [72]. We consider a massless scalar field ψ propagating in a dissipative medium, modeled by a damping coefficient $\tilde{c}$. In the rest frame

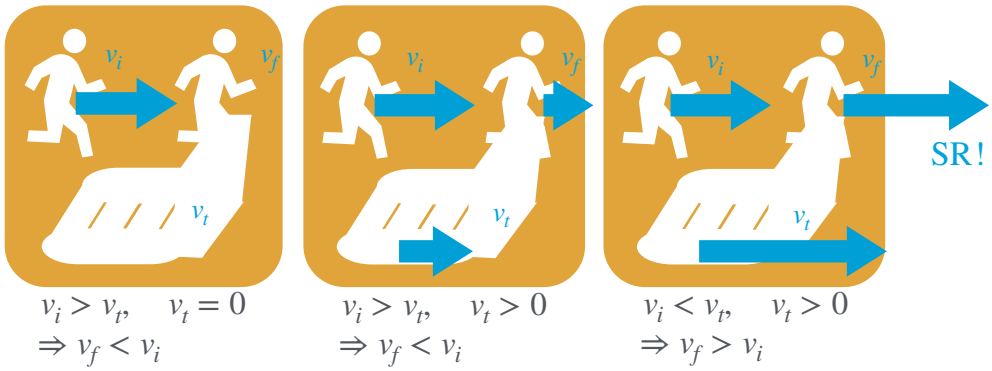

FIG. 3.1: Heuristic example for linear "superradiance" on a treadmill: In the first two pictograms, the treadmill either does not move ($v_t = 0$), or moves slower than the person jumping onto it ($v_t < v_i$), so friction slows the movement down ($v_f < v_i$). In the third pictogram, the treadmills moves so fast that w.r.t to the treadmill the person moves backwards ($v_t > v_i$), so that the friction increases the speed ($v_f > v_i$).

of the medium, the equation of motion for ψ is

$$\Box\psi - \tilde{c}\dot{\psi} = 0\,, \tag{3.1}$$

where the dot denotes a derivative with respect to time in the medium's rest frame. We now consider the case where the medium rotates with constant angular velocity Ω. For a cylindrically symmetric configuration, we make the ansatz

$$\psi(t, r, \phi) = f(r)\, e^{-i(\omega t - m\phi)}\,, \tag{3.2}$$

where ω is the field's frequency in the laboratory frame, $m \in \mathbb{Z}$ is the azimuthal quantum number, and r, ϕ are polar coordinates in the plane perpendicular to the rotation axis. To simplify the analysis, we evaluate the field at a fixed radius $r = R$ and define a local Cartesian coordinate $x \equiv R\phi$, representing the arc length along the circular path of rotation. Although the full system involves rotation, at a fixed radius we can approximate the motion along x as linear. We can then apply the Lorentz transformation with velocity $v \equiv \Omega R$ into the lab frame in which the medium rotates. In this frame, the damping term changes to

$$\begin{aligned}
\tilde{c}\partial_t\psi &\to \tilde{c}\gamma(\partial_t\psi - v\partial_x\psi) \\
&= \tilde{c}\gamma(\partial_t - v\frac{1}{R}\partial_\phi)\psi \\
&= -i\tilde{c}\gamma(\omega - \frac{\Omega R}{R}m)\psi \\
&= -i\tilde{c}\gamma(\omega - \Omega m)\psi\,.
\end{aligned} \tag{3.3}$$

This demonstrates that when $\Omega m > \omega$, i.e., when the medium rotates faster than the spherical modes of the wave oscillate, the effective damping in the lab frame becomes negative, leading to wave amplification. This happens because in the rotating frame the frequency becomes $\omega' = \omega - m\Omega$.

We found the general superradiance condition

$$\omega < m\Omega\,. \tag{3.4}$$

If this is satisfied, then $\omega' < 0$, so from the perspective of the rotating frame it corresponds to a negative-energy state. This means that dissipation actually makes the energy less negative, i.e., brings it closer to zero. From the point of view of the lab frame, this corresponds to an increase in the wave's energy, resulting in an amplification of the wave. The energy gain comes at the expense of the medium's rotational kinetic energy. Physically, this corresponds to the medium amplifying the wave rather than absorbing it. We see that all the important characteristics of the amplification have a clear analogue in our initial heuristic treadmill argument. The rotational medium can dissipate energy, like the treadmill via friction. However, the dissipation can actually amplify states when in the moving frame the state that scatters effectively has negative energy, like a person jumping on a treadmill that moves fast. We will see in the next section, that for rotating BHs, the horizon provides the dissipation, while the ergoregion can provide the negative energy states, so BH superradiance becomes possible if the superradiance condition Eq. (3.4) is fulfilled.

3.2 Black Hole Superradiance

3.2.1 Rotating Black Holes - The Kerr Metric

BHs are vacuum solutions of general relativity (GR) [100] that possess a singularity hidden behind an event horizon, a region inside of which all future-directed timelike curves end at the singularity. Vacuum solutions in GR are metric tensors g obeying the Einstein field equations in vacuum, written in local coordinates x^μ as

$$R_{\mu\nu} - \frac{1}{2} g_{\mu\nu} R = 0\,, \tag{3.5}$$

where $R_{\mu\nu}$ is the Ricci tensor defined as $R_{\mu\nu} \equiv \partial_\rho \Gamma^\rho_{\mu\nu} - \partial_\nu \Gamma^\rho_{\mu\rho} + \Gamma^\rho_{\rho\lambda}\Gamma^\lambda_{\mu\nu} - \Gamma^\rho_{\nu\lambda}\Gamma^\lambda_{\mu\rho}$, in terms of the metric itself and the Christoffel symbols $\Gamma^\rho_{\mu\nu} = \frac{1}{2} g^{\rho\sigma}\left(\partial_\mu g_{\nu\sigma} + \partial_\nu g_{\mu\sigma} - \partial_\sigma g_{\mu\nu}\right)$. We also introduced the Ricci scalar (scalar curvature) $R \equiv g^{\mu\nu} R_{\mu\nu}$. Solutions are often written in terms of the line element defined by $ds^2 \equiv g_{\mu\nu} dx^\mu dx^\nu$.

While the first solution to Eq. (3.5) was found in 1916, very shortly after the introduction of GR, in form of the Schwarzschild solution describing a non-rotating BH [101], closely followed by the first solutions for homogeneous and isotropic universes, the *Kerr metric*, describing a rotating BH was published only much later, in 1963 in Ref. [102]. Some authors contributed this to its notoriously hard derivation, see Ref. [103] for details.

The metric describes a rotating BH with fixed angular momentum, and is given in the so-called Boyer-Lindquist coordinates [104][I] and after setting $c = 1$ by

$$ds^2 = -\left(1 - \frac{2GMr}{\Sigma}\right) dt^2 - \frac{4GMr\sin^2(\theta)}{\Sigma} dt d\phi + \frac{\Sigma}{\Delta} dr^2 + \Sigma d\theta^2 + \frac{(r^2+a^2)^2 - a^2\Delta\sin^2\theta}{\Sigma}\sin^2(\theta) d\phi^2 \,, \tag{3.6}$$

with

$$\Sigma = r^2 + a^2\cos^2(\theta)\,, \tag{3.7}$$

$$\Delta = (r - r_+)(r - r_-) = r^2 + a^2 - 2GMr\,, \tag{3.8}$$

$$a = \frac{J}{M}\,, \tag{3.9}$$

where G is Newton's gravitational constant, and M and J can be identified with the BH's mass and spin, respectively. We define the *gravitational radius* $r_g = GM$. However, note that compared to the horizon in the static limit, the event horizon for the rotating BH is modified by a, and is given by

$$r_\pm = r_g \pm \sqrt{r_g^2 - a^2}\,, \tag{3.10}$$

with $\pm$ referring to the outer and inner event horizon, respectively.[II] These are the two roots of Δ. The radii for which g_{tt} becomes zero are $r_e = r_g \pm \sqrt{r_g^2 - a^2\cos^2(\theta)}$ and they define the *ergoregion*. In this region, no observer can stay static, but instead is forced to move in the same direction the BH rotates. In this region, the sign of g_{tt} flips and ∂_t becomes spacelike. We will understand in a moment, why this is crucial for the mechanism of superradiance around BHs.

The spin of the BH has an upper bound. Assuming that the horizon r_g is physical, and it actually hides the singularity[III], the term in the root of Eq. (3.10) must be positive, and therefore $a < r_g$, which immediately gives

$$J_{\max} = GM^2 \tag{3.11}$$

for an extremal BH. One then introduces $\tilde{a} \leqslant 1$ as a dimensionless quantity to express the spin relative to the spin of the extremal BH,[IV] i.e., $J = \tilde{a}J_{\max} = \tilde{a}GM^2$. This is obviously related to the parameter a in the Kerr metric by $\tilde{a} \equiv a/r_g$.

Another important quantity is the is the angular velocity of the horizon Ω_H. The Kerr metric is stationary and axisymmetric, which means that ∂^t and ∂^ϕ are Killing vector of this metric. We can define the combination $\chi^\mu\partial_\mu = \partial_t + \Omega_H\partial_\phi$ that is also a Killing vector field, and must be null

[I] In these coordinates, the surfaces of constant r and t are not spheres, but oblate spheroids, with the degree of flattening determined by the parameter a from the metric.

[II] Only the outer horizon will be important for our purposes.

[III] This is the cosmic censorship conjecture that no "naked" singularities can exist [105].

[IV] In the literature this is also often labeled χ.

on the horizon by the definition of the latter, i.e., $\chi^\mu \chi_\mu|_{r=r_+} = 0$. This condition gives

$$\Omega_H = \frac{a}{r_+^2 + a^2} = \frac{a}{2(r_g^2 + r_g\sqrt{r_g^2 - a^2})} \,. \tag{3.12}$$

Relating this to the results of Sec. 3.1, the angular velocity of the horizon will be crucial for the process of superradiance.

3.2.2 BH Superradiance

The first proposed mechanism to make use of the special properties of the ergoregion was the Penrose mechanism [71]. In this, a particle enters the ergoregion and splits into two in a specific way: One fragment moves so fast towards the horizon, that its energy is negative for an observer at infinity, which is only possible in the ergoregion. Because energy is conserved during the splitting, the other half of the particle can escape the BH with more energy than both of them had together initially. The negative energy fragment falls into the horizon, feeding negative energy into the BH, i.e., extracting positive energy. Hence, the BH loses mass and angular momentum.

We are interested in the wave analogue of the Penrose process. We again invoke the Killing vector χ^μ and write it as sum of the Killing vector related to time translations $\mathcal{H}^\mu \partial_\mu \equiv \partial_t$ and rotational invariance $\mathcal{J}^\mu \partial_\mu \equiv \partial_\phi$ and write [37]

$$\chi = \mathcal{H} + \Omega_H \mathcal{J} \,. \tag{3.13}$$

We now consider an incoming wave of a massless scalar field with the ansatz

$$\psi = e^{-i\omega t + im\phi} f(r,\theta) + h.c. \,. \tag{3.14}$$

We can find the conserved energy flux of this field by

$$P_\mu = -T_{\mu\nu}\mathcal{H}^\nu = -\partial_\mu\psi\partial_t\psi + \frac{1}{2} g_{\mu t}\mathcal{L} \,, \tag{3.15}$$

where $T_{\mu\nu}$ is the field's energy momentum tensor and $\mathcal{L}$ is the Lagrangian density. If we consider a space-time region between two constant time slices, the conservation of the current P_μ implies that the time-averaged energy flux at infinity must be equal to the time-averaged energy flux through the BH horizon. The latter can be derived considering χ_μ via [37]:

$$\begin{aligned} \langle P_\mu \chi^\mu \rangle &= -\langle (\partial_t\psi + \Omega_H \partial_\phi \psi)\partial_t\psi) \rangle \\ &= \omega(\omega - m\Omega_H)|f|^2 \,. \end{aligned} \tag{3.16}$$

Here, the $g_{\mu\nu}$-term in the energy-momentum tensor vanished, because the vectors χ and $\mathcal{H}$ are perpendicular at the horizon. Again, when the superradiance condition $\omega < m\Omega_H$ holds, then $\langle P_\mu \chi^\mu \rangle$ becomes negative, indicating that energy is extracted from the horizon. This occurs because, for observers co-moving with the null Killing vector χ^μ at the horizon, the mode fulfilling the

superradiance condition has negative energy, even hough its frequency is measured to be positive, $\omega > 0$, at infinity. Implicitly this is only possible due to the existence of the ergoregion, where ∂_t becomes spacelike. This allows modes with positive energy at infinity to have negative Killing energy near the horizon. Dissipation of these negative-energy modes at the horizon leads to amplification of the reflected wave at infinity, thereby enabling superradiance. The horizon's angular velocity Ω_H explicitly encodes this effect: At the horizon, deep inside the ergoregion, everything is forced to co-rotate along the BH with Ω_H, making negative energy states possible. Without rotation, the ergoregion disappears, rendering Ω_H zero, and making superradiance impossible.

Now that we have introduced superradiance in three different scenarios, we make a final comparison of the key elements to trigger successful superradiance in Tab. 3.1. From now on superradiance will always refer to BH superradiance.

Aspect	**Treadmill**	**Zel'dovich**	**BH Superradiance**
Dissipation mechanism	Surface Friction	Dissipative Medium	BH horizon
Negative energy mechanism	Treadmill movement	Rotating frame	Ergoregion
SR condition	$v_i < v_t$	$\omega < m\Omega$	$\omega < m\Omega_H$

TABLE 3.1: A summary comparison of superradiance mechanisms and analogies. Outside of the superradiance regime, a dissipative medium/object just reduces energy for a moving object or wave. Configurations that fulfill the superradiance condition effectively have negative energy, so for these, the dissipation leads to amplification.

We note that the above argument works fine for massless states that have a finite flux at infinity. If we are treating bound states, and the frequency ω corresponds to a discrete spectrum, then the energy flux at the infinity necessarily vanishes. It will turn out that in this case the only possibility to reconcile the flux at the horizon with the energy conservation argument is for ω to acquire an imaginary part, so that the time-averaged energies on the two constant time slices are not equal any longer [37]. For the research presented in this thesis, it will be sufficient to use the imaginary part of the bound states' frequencies by the Detweiler approximation laid out in Sec. 3.3.3.

3.2.3 BH Thermodynamics and the Area Law

It might seem counter-intuitive at first that superradiance is possible for BHs, because the process extracts angular momentum and mass from it, while the one commonly assumed "fact" about BHs is that supposedly nothing can escape from it. However, what is actually true classically, i.e., in GR, is that the area of the BH horizon can never shrink. Involving quantum mechanics, this law seems to be violated by Hawking radiation [31], but we will ignore that here. The first two laws of BH thermodynamics are [106]:

- The *Energy Conservation Law* states that infinitesimal mass changes δM obey

$$\delta M = \frac{\kappa}{8\pi G}\delta A_H + \Omega_H \delta J + \Phi_H \delta Q\,. \tag{3.17}$$

Here $\kappa = 1/(4GM) - GM\Omega_H^2$ is the surface gravity, A_H is the area of the horizon, Ω_H is again the angular velocity at the horizon, Φ_H is the electrostatic potential at the horizon and Q the charge of the BH.

- The Area Law, also referred to as *Entropy Law* states that if matter obeys the weak energy condition, that is for any time-like vector v^μ the energy-momentum tensor fulfills $T_{\mu\nu}v^\mu v^\nu \geqslant 0$, we have

$$\delta A_H \geqslant 0\,. \tag{3.18}$$

We are now going to confirm that when Eq. (3.17) is assumed to be fulfilled, we also still fulfill Eq. (3.18) during superradiance, although we extract energy and angular momentum from the BH. We set $\Phi_H = 0$ from here on, assuming the BH to be uncharged.

To find the extracted mass and angular momentum, we again use the Killing vector fields $\mathcal{H}$ and $\mathcal{J}$. The contravariant version of the conserved energy flux vector for $T_{\mu\nu}$ is

$$P^\mu = -T^\mu{}_\nu\,\mathcal{H}^\nu\,, \tag{3.19}$$

while the conserved angular momentum flux vector is

$$L^\mu = T^\mu{}_\nu\,\mathcal{J}^\nu\,. \tag{3.20}$$

We find the extracted energy and angular momentum by calculating the flux through a surface $\vec{d\Sigma}_\mu$:

$$\delta E = P^\mu \vec{d\Sigma}_\mu, \quad \delta J = L^\mu \vec{d\Sigma}_\mu\,. \tag{3.21}$$

If we take as a surface $\vec{d\Sigma}_\mu = n_\mu r^2 dt d\Omega$, where n_μ is the radial outgoing normal to the surface, we have

$$\delta E = P^\mu n_\mu r^2 dt d\Omega = -T^\mu{}_\nu\,\mathcal{H}^\nu n_\mu r^2 dt d\Omega = -T^r{}_t\, r^2\,, \tag{3.22}$$

and similarly $\delta J = T^r{}_\phi\, r^2$. This gives

$$\frac{\delta J}{\delta E} = -\frac{T^r{}_\phi}{T^r{}_t}\,. \tag{3.23}$$

We now again take the ansatz for a scalar field Eq. (3.14). The components of $T^\mu{}_\nu$ important for our argument will then be given by

$$T^r{}_\phi = g^r{}_\alpha \partial^\alpha\psi\partial^\phi\psi = g^r{}_r \frac{df}{dr} e^{-2i\omega t+2im\phi} im\,, \tag{3.24}$$

$$T^r{}_t = g^r{}_\alpha \partial^\alpha\psi\partial^t\psi = g^r{}_r \frac{df}{dr} e^{-2i\omega t+2im\phi}(-i\omega)\,, \tag{3.25}$$

This leads to

$$\frac{\delta J}{\delta E} = \frac{m}{\omega}\,. \tag{3.26}$$

We can identify δE with δM, so for a scalar field interacting with a BH, this gives $\delta J = (m/\omega)\delta M$. With that, Eq. (3.17) becomes

$$\delta M \frac{8\pi}{\omega\kappa}\left(\omega - m\Omega_H\right) = \delta A_H, \tag{3.27}$$

We have found in the last section that if the superradiance condition Eq. (3.4) is fulfilled, mass will be extracted from the BH:

$$\delta M < 0 \quad \Longleftrightarrow \quad \omega < m\Omega_H\,, \tag{3.28}$$

With that we find that the left hand side of Eq. (3.27) is positive, which means that although mass is extracted from the BH, the area of the horizon grows, as is expected from BH thermodynamics.

It should be noted here that we have assumed that the weak energy condition holds. This is violated for fermions in asymptotically flat spacetimes, and ultimately this is the reason why they cannot experience superradiance [87].

3.2.4 Extraction Bound

We just showed that the area law is fulfilled during superradiance. It is possible to extract both angular momentum and mass from the BH without reducing the area of the horizon because reducing angular momentum while keeping mass constant increases the horizon area of the rotating BH. The latter is given by

$$A_H = 8\pi\left(r_g^2 + r_g\sqrt{r_g^2 - a^2}\right)\,. \tag{3.29}$$

For any giving rotating BH, the corresponding *irreducible mass* $M_{\rm irr}$ is the mass of a Schwarzschild BH that would leave the area of the horizon unchanged. It is found by equating the area given above with $8\pi(GM_{\rm irr})^2$ and hence is given by

$$M_{\rm irr} = \frac{1}{G}\sqrt{\frac{1}{2}\left(r_g^2 + r_g\sqrt{r_g^2 - a^2}\right)}\,. \tag{3.30}$$

The theoretical upper bound on the amount of mass any process, including superradiance, can extract from the BH is given by the difference between the initially mass of the rotating BH and the irreducible mass:

$$M - M_{\rm irr} = M\left(1 - \frac{1}{\sqrt{2}}\sqrt{1 - \sqrt{1 - \tilde{a}^2}}\right)\,. \tag{3.31}$$

Starting with an extremal BH for which $\tilde{a} = 1$, we find as strong upper bound $(1 - \frac{1}{\sqrt{2}})M \approx 0.29M$. However, because the superradiant condition will not be fulfilled anymore at one point during the spin-down, this strict upper bound will not be reached. We will discuss the extraction bound and corresponding cloud mass in Sec. 3.4.1 after introducing the important parameters, and in most detail in Ch. 8.

3.3 Massive Scalar Field in the Kerr Metric

So far we have discussed superradiance as a phenomenon for massless fields, which would experience superradiance once during scattering and then escape to infinity. This also works for photons of

the correct wavelength. One technological idea to turn this into a runaway process and with that continuously extract energy from a rotating BH is the *BH-bomb* proposed in Ref. [74]. There, a rotating BH would be placed inside a reflective cavity, like a mirror. Then a seed of initial photons would be injected and could be periodically amplified by superradiance scattering and reflected at the mirror back to the BH. It was realized soon after that the gravitational coupling of a massive field provides a confining potential by itself. A massive field experiences superradiant scattering, but is also gravitationally bound to the BH, and therefore could built up over time, even from a quantum fluctuation producing a single particle in the vicinity of the BH. In this section we will discuss, how the approximate solution for a scalar field in the Kerr metric is found, and how their superradiance rates can be derived.

The action for a massive scalar field Ψ with mass μ is given by

$$S = \int d^4x\sqrt{-g}\mathcal{L} = \int d^4x\sqrt{-g}\left[\frac{1}{2}\partial_\mu\Psi g^{\mu\nu}\partial_\nu\Psi - \frac{1}{2}\mu^2\Psi^2\right] . \tag{3.32}$$

In a general curved space-time, the Euler-Lagrange equation is

$$\frac{\partial\mathcal{L}}{\partial\Psi} - \frac{1}{\sqrt{-g}}\partial_\mu\left(\sqrt{-g}\frac{\partial\mathcal{L}}{\partial(\partial_\mu\Psi)}\right) . \tag{3.33}$$

For the Kerr metric, the inverse metric, defined by $g^{\mu\nu}g_{\mu\nu} = \delta_{\mu\nu}$ is given by

$$g^{tt} = -\frac{1}{\Delta}\left(r^2 + a^2 + \frac{2r_g r a^2\sin^2(\theta)}{\Sigma}\right) , \tag{3.34}$$

$$g^{t\phi} = -\frac{2r_g r a}{\Sigma\Delta} , \quad g^{rr} = \frac{\Delta}{\Sigma} , \tag{3.35}$$

$$g^{\theta\theta} = \frac{1}{\Sigma} , \quad g^{\phi\phi} = \frac{\Delta - a^2\sin^2(\theta)}{\Sigma\Delta\sin^2(\theta)} , \tag{3.36}$$

with all other components being zero, and $\sqrt{-g} = \Sigma\sin(\theta)$. Inserting this into the Euler-Lagrange equation, we arrive at the full equation of motion for a scalar field in the Kerr metric

$$\begin{aligned} 0 =& \mu^2\Sigma\Psi + \left[\frac{(r^2+a^2)^2}{\Delta} - a^2\sin^2(\theta)\right]\partial_t^2\Psi - \partial_r(\Delta\partial_r\Psi) \\ &- \frac{\Delta - a^2\sin^2(\theta)}{\Delta\sin^2(\theta)}\partial_\phi^2\Psi - \frac{1}{\sin(\theta)}\partial_\theta(\sin(\theta)\partial_\theta\Psi) + \frac{2a}{\Delta}(r^2+a^2-\Delta)\partial_t\partial_\phi\Psi . \end{aligned} \tag{3.37}$$

There is no known analytical solution to the full equation, so to continue, we are going to have to make some simplifying assumptions.

3.3.1 Spectra of Gravitational Atoms

We assume that we can isolate non-relativistic dynamics of the field by factoring out the rapid oscillations with the Compton frequency, $\exp(i\mu t)$, and average over them later, and that the

remaining field ψ changes on times scales much longer. Hence, we write

$$\Psi(t,\boldsymbol{r}) = \frac{1}{\sqrt{2\mu}}\left(\psi(t,\boldsymbol{r})e^{-i\mu t} + \psi^*(t,\boldsymbol{r})e^{i\mu t}\right) , \tag{3.38}$$

where ψ is a complex scalar field that varies on timescales much longer than μ^{-1}. The action for ψ then reads [25]:

$$S = \int d^4x\sqrt{-g}\left[-\frac{1}{2\mu}\left(\nabla_a\psi^*\nabla^a\psi + i\mu g^{0a}(\psi^*\nabla_a\psi - \psi\nabla_a\psi^*) + \mu^2(g^{00}+1)\psi^*\psi\right)\right] . \tag{3.39}$$

Since we already imposed that the cloud is non-relativistic, and we are looking for bound states, we can assume that the energy must be given by $\omega \approx \mu + \frac{\boldsymbol{p}^2}{2\mu}$ where $\boldsymbol{p}^2 < 0$. To find the size of the cloud, r_c, we insert that we expect the kinetic energy to be of the same order as the potential energy of a single particle by the virial theorem, which gives

$$\frac{|\boldsymbol{p}|^2}{\mu} \sim \frac{GM\mu}{r_c} . \tag{3.40}$$

For the lowest bound state energy level, the wavelength should match the circumference of the cloud. If the energy states are discrete, labeled by quantum number n, higher n-states should have wavelengths that are multiples of this fundamental. With the usual relation between wavelength and momentum this leads to

$$n\lambda \sim 2\pi r_c \Rightarrow n\frac{2\pi}{|\boldsymbol{p}|} \sim 2\pi r_c . \tag{3.41}$$

Solving this for $|\boldsymbol{p}|$ and inserting it back into Eq. (3.40), we can solve for the radius of the cloud:

$$r_c = \frac{n^2}{GM\mu^2} \equiv \frac{n^2}{\mu\alpha} = \frac{n^2 r_g}{\alpha^2} , \tag{3.42}$$

Henceforth, this will act as the definition of r_c. We defined the dimensionless quantity

$$\alpha \equiv GM\mu = r_g\mu . \tag{3.43}$$

This is called the *gravitational fine-structure constant* for a reason that will become obvious in a moment. It gives the ratio of the event horizon to the Compton wavelength of the scalar field. For $n = 1$, Eq. (3.42) defines the *gravitational Bohr radius* $r_b \equiv (\mu\alpha)^{-1}$. Typical values for BH mass and ultralight scalar for small α are

$$\alpha \approx 0.07\left(\frac{M}{10M_\odot}\right)\left(\frac{\mu}{10^{-12}\,\mathrm{eV}}\right) . \tag{3.44}$$

We now assume $\alpha \ll 1$, which in the following sections will both allow us to find the growth and decay rates of the states, as well as to form gravitational atoms with astrophysically relevant formation- and lifetimes. Since we are interested in the behavior of the cloud where it peaks, at r_c, and for $\alpha \ll 1 \rightarrow r_c \gg r_g$, we can write out all the terms in Eq. (3.39) and do an expansion

in $r_g/r_b = r_g\mu\alpha = \alpha^2$. Since we are interested in distances $r \sim r_c$, a factor of r will effectively contribute like α in the power-counting. For terms with derivatives with respect to time we will acknowledge that for a non-relativistic field, the time derivative should be proportional to kinetic energy, which again by Eq. (3.40) we can relate to α:

$$\partial_t\psi \sim \frac{\boldsymbol{p}^2}{\mu}\psi \sim \left.\frac{GM\mu}{r}\right|_{r=r_B}\psi = \mu\alpha^2\psi\,. \tag{3.45}$$

This makes it possible to write out the Lagrangian of Eq. (3.39) as $\mathcal{L} = \mathcal{L}_2 + \mathcal{L}_4 + \mathcal{O}(\alpha^5)$, where the subscript refers to the power of α in the expansion. The quadratic Lagrangian $\mathcal{L}_2$ gives the equation of motion

$$i\frac{\partial}{\partial t}\psi(t,\boldsymbol{r}) = \left(-\frac{1}{2\mu}\boldsymbol{\nabla}^2 - \frac{\alpha}{r}\right)\psi(t,\boldsymbol{r})\,. \tag{3.46}$$

This is the Schrödinger equation of a hydrogen atom, with α substituting the electromagnetic fine-structure constant. This dubbed the term gravitational atom. The solutions are superpositions of

$$\psi_{nlm}(t,r,\theta,\phi) \simeq e^{-(\omega-\mu)t}\mathcal{R}_{nl}(r)Y_{lm}(\theta,\phi)\,, \tag{3.47}$$

where $\mathcal{R}_{nl}(r)$ are the radial wavefunctions of the hydrogen atom with r_B substituting the atomic Bohr radius. $Y_{lm}(\theta,\phi)$ are the spherical harmonics. The radial wavefunctions are given by

$$\mathcal{R}_{nl}(r) = \sqrt{\left(\frac{2\mu\alpha}{n}\right)^3\frac{(n-l-1)!}{2n(n+l)!}}\left(\frac{2\mu\alpha r}{n}\right)^l\exp\left(-\frac{\mu\alpha r}{n}\right)L^{2l+1}_{n-l-1}\left(\frac{2\mu\alpha r}{n}\right)\,, \tag{3.48}$$

where $L^{2l+1}_{n-l-1}(x)$ is the associated Laguerre polynomial. As in atomic physics [107], the states are distinguished by the general quantum number n, their angular momentum l and the magnetic quantum number m, i.e., the value of the angular momentum in z-direction. The states are written in terms of these quantum numbers $|nlm\rangle \equiv \psi_{nlm}(t,r,\theta,\phi)$.

As in quantum mechanics, these discrete states also have discrete energy levels. Just considering the leading order terms, states solving Eq. (3.46) have energy $\omega_{nlm} = \mu\left(1-\frac{\alpha^2}{2n^2}\right)$, independent of l and m. To find the so-called fine and hyperfine corrections, we have to include terms of higher order in α from Eq. (3.39). The full spectrum including Bohr, fine and hyperfine energy splitting is given by [25, 83]

$$\omega_{nlm} = \mu\left[1 - \frac{\alpha^2}{2n^2} - \left(\frac{1}{8n} + \frac{6}{2l+1} - \frac{2}{n}\right)\frac{\alpha^4}{n^3} + \frac{16}{2l(2l+1)(2l+2)}\frac{\tilde{a}m\alpha^5}{n^3}\right]\,. \tag{3.49}$$

This derivation works only in the limit far from the horizon. Therefore it does not capture the effect of the horizon. This will lead to non-zero imaginary parts of the frequency, and hence growing and decaying modes. Before discussing the derivation of these, we will give some heuristic arguments.

3.3.2 Growing the Cloud: Superradiance Rates

The last section did only consider the behavior of the cloud far away from the horizon and for small α. However, compared to atomic physics, where the wavefunctions must be regular at $r = 0$, for the gravitational atom, the wavefunction must be purely ingoing at the horizon. As already hinted in Sec. 3.2.2, matching this condition with the large distance behavior will lead to non-zero imaginary parts of the frequency. We start with an heuristic argument to find the scaling of the decay rates, and then sketch the Detweiler approximation [32] to find the non-relativistic growth and decay rates in the small α-limit.

The superradiance rate necessarily must be equal to the ratio of (negative) energy change of the BH and total energy of the cloud, the latter for non-relativistic clouds being its mass M_c:

$$\Gamma_\mathrm{SR} \simeq -\frac{\dot{E}_\mathrm{BH}}{M_\mathrm{c}} \,. \tag{3.50}$$

$\dot{E}_\mathrm{BH}$ has to be proportional to the superradiance condition and the density of the cloud at the horizon, which is $\psi^2\big|_{r_+}$, integrated over the horizon area. We approximate this integral via multiplication by r_+^2, which gives

$$\dot{E}_\mathrm{BH} \sim (\omega - m\Omega_H)\, \psi^2\big|_{r_+}\, r_+^2 \,. \tag{3.51}$$

The radial wavefunction of the cloud scales as $\psi^2\big|_{r_+} \sim \psi|_{r_c}\,(r/r_c)^l e^{-r/r_c}$. We find the mass of the cloud via $M_\mathrm{c} \simeq \mu \int dr r^2 \psi^2$. Integrating this gives the scaling

$$M_\mathrm{c} \sim \mu r_c^3\, \psi^2\big|_{r_c} \,. \tag{3.52}$$

Neglecting the exponential part of the radial wavefunction, inserting all of this into Eq. (3.50) gives

$$\begin{aligned} \frac{\dot{E}_\mathrm{BH}}{M_\mathrm{c}} &\sim (\omega - m\Omega_H) \frac{\left(\frac{r_+}{r_c}\right)^{2l} r_+^2}{r_c^3 \mu} \\ &\sim (\omega - m\Omega_H) \frac{r_+^{2l+2}}{\mu r_c^{3+2l}} \,. \end{aligned} \tag{3.53}$$

We can now use $r_+ = r_g(1 + \sqrt{1 - \tilde{a}^2}) \approx r_g$ and again that $r_c \sim r_g/\alpha^2$, and find

$$\begin{aligned} \frac{\dot{E}_\mathrm{BH}}{M_\mathrm{c}} &\sim (\omega - m\Omega_H) \frac{(r_g)^{2l+2} \alpha^{4l+6}}{\mu (r_g)^{2l+3}} \\ &\sim (\omega - m\Omega_H) \frac{\alpha^{4l+6}}{r_g \mu} \,. \end{aligned} \tag{3.54}$$

Hence, the scaling of the superradiance rate is

$$\Gamma_\mathrm{SR} \sim -(\omega - m\Omega_H) \alpha^{4l+5} \,. \tag{3.55}$$

We see that the rate is extremely sensitive to the value of α, which leads to the important fact that

for every given BH mass, there is only a finite frame of possible scalar masses where the cloud can grow on astrophysical time-scales. If α is closer to one, the growth will be extremely fast, and, as we will see later, then decay fast due to decay into gravitational waves. The combination of these two phenomena leaves, for every given BH mass, only a small window in the scalar mass parameter space where superradiance is viable.

3.3.3 Detweiler Approximation

The best-known derivation of the superradiance rates for $\alpha \ll l$, which is not necessarily $\alpha \ll 1$ has been done by Detweiler in Ref. [32]. We will only sketch the derivation here.

Even the full equation of motion of the scalar field, before expanding into powers of α^2, is separable into spherical and radial part, and the equation for the radial wavefunction is found to be

$$\Delta \frac{d}{dr}\left(\Delta \frac{dR}{dr}\right) + [\Omega^2(r^2+a^2)^2 - 4aGMrm\Omega + a^2m^2 - \Delta(\mu^2 r^2 + a^2\Omega^2 + \lambda)]R = 0\,, \tag{3.56}$$

where λ is a separation constant coming from the spherical wavefunction. We seek solutions that are outgoing at infinity and ingoing at the horizon. Detweiler then approximates the radial equation for small α with momentum $p^2 \equiv \mu^2 - \omega^2$, and identical to our initial calculation to find r_c, $n \equiv GM\mu^2/p$ and $x \equiv 2pr$ as

$$\frac{d^2(xR)}{dx^2} + \left[-\frac{1}{4} + \frac{n}{x} - \frac{l(l+1)}{x^2}\right] xR = 0\,. \tag{3.57}$$

which resembles the radial equation for the hydrogen atom and has the analytic solution

$$R(x) = x^l e^{-x/2} U(l+1-n, 2l+2, x)\,, \tag{3.58}$$

where U is a confluent hypergeometric function. For the hydrogen atom, n corresponds to the principal quantum number and satisfies $n = l + 1 + \nu$, where ν is also integer. However, due to boundary condition at the horizon, we expect an instability and therefore a small imaginary part in n, δn:

$$n - l - 1 \equiv \nu + \delta n\,. \tag{3.59}$$

The solution for $R(x)$ can be expanded into real and imaginary part. The full radial equation is then simplified in the near horizon limit, i.e., limit of $r \ll 1$, which again admits analytic solutions, this time in terms of hypergeometric functions. This solution admits independent solutions that describe ingoing and outgoing waves at the horizon. Both approximations have overlapping regions of validity. This can be used to do a matching of the lowest terms of the Taylor expansion for the $r \gg 1$ solution, but at the smallest r still valid, with the asymptotic behavior of the near horizon, $r \ll 1$ solution. This matching can be done in a way that finds a value of δn such that the outgoing

solution for the near horizon limit vanishes. This enforces the purely ingoing boundary conditions. Successful matching is only possible if δn is non-zero and imaginary.

Defining the complex frequency $\omega = \omega_{\mathrm{R}} + i\Gamma$ gives the superradiance rate via

$$i\Gamma = \frac{\delta n}{GM}\left(\frac{GM\mu}{l+1+\nu}\right)^3 . \tag{3.60}$$

The full result is

$$\Gamma_{nlm} \simeq 2\tilde{r}_+ C_{nl}\, g_{lm} \alpha^{4l+5}(m\Omega_H - \omega_{nlm}) , \tag{3.61}$$

with

$$g_{lm} \equiv \prod_{k=1}^{l}\left[k^2(1-\tilde{a}^2) + (\tilde{a}m - 2r_+\omega)^2\right] , \tag{3.62}$$

$$C_{nl} \equiv \frac{2^{4l+1}(n+l)!}{n^{2l+4}(n-l-1)!}\left(\frac{l!}{(2l)!(2l+1)!}\right)^2 , \tag{3.63}$$

$$\tilde{r}_+ = 1 + \sqrt{1-\tilde{a}^2} , \quad GM\Omega_H = \tilde{a}/(2\tilde{r}_+) . \tag{3.64}$$

For reference, typical inverse superradiance rates for extremal spinning BHs are

$$\Gamma_{211}^{-1} \approx 4.6\times 10^6 \left(\frac{M}{10\,M_\odot}\right)\left(\frac{0.1}{\alpha}\right)^9 \mathrm{s} , \tag{3.65}$$

$$\Gamma_{322}^{-1} \approx 1.8\times 10^5 \left(\frac{M}{10\,M_\odot}\right)\left(\frac{0.1}{\alpha}\right)^{13} \mathrm{yrs} . \tag{3.66}$$

However, note that these rates depend on the dimensionless spin, and will go to zero when the cloud reached the corresponding saturation. Due to the l-dependence of the scaling of Eq. (3.61) with α, low l modes grow fastest, assuming the superradiance condition is fulfilled. That means for an extremal BH, the $l = 1$ modes grow first, dominated by $n = 2, l = 1, m = 1$, and only when the BH angular momentum is exhausted, such that the superradiance condition is not fulfilled anymore, the higher l-modes can become dominant. Fig. 3.2 shows the growth regions in the BH *Regge plane* showing mass and spin for a fixed scalar mass, and also gives an example how a single BH moves through this plane.

3.3.4 $\alpha \gg 1$-limit

In the limit where $\alpha \gg 1$ it is also possible to find analytical results, for details see Ref. [37, 108]. In this case, a WKB approximation can be used, which reduces the problem to a Schrödinger equation for $\Psi \equiv (r^2+a^2)^{1/2}R$ with a potential:

$$\frac{d^2\Psi}{dr_*^2} - V\Psi = 0 , \tag{3.67}$$

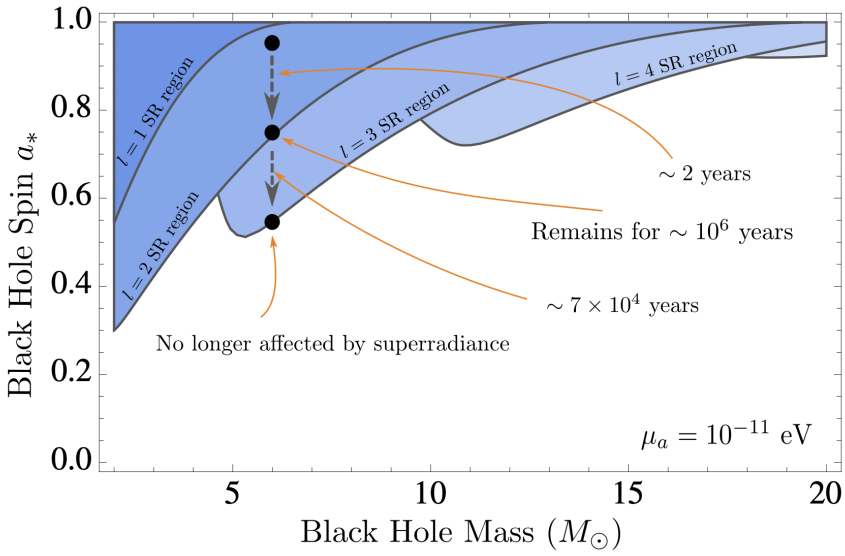

FIG. 3.2: Effect of superradiance for an ultralight scalar with mass $\mu_a = 10^{-11}$ eV. Shaded regions correspond to the BH parameter in which superradiance would spin down the BH in shorter than 10^6 years, for $l = 1$ (dark blue) to $l = 5$ (light blue) levels. The plot also shows an example evolution of a $6\,M_\odot$ BH with initial spin $\tilde{a} = 0.95$. Graphic taken from Ref. [88].

where $dr_* = \frac{r^2+a^2}{\Delta}dr$ is the tortoise coordinate, and where

$$V = -\omega^2 + \frac{4r_g r a m\omega - a^2m^2}{(r^2+a^2)^2} + \frac{\Delta}{r^2+a^2}\left(\mu^2 + \frac{l(l+1)+k^2a^2}{r^2+a^2} + \frac{3r^2-4r_g r+a^2}{(r^2+a^2)^2} - \frac{3\Delta r^2}{(r^2+a^2)^2}\right), \quad (3.68)$$

and r is assumed to be a function of r_*. Plotted for typical parameters as in Fig. 3.3 the potential reveals, how the potential actually provides the confinement mechanism that is necessary to transform single superradiant scattering events into an exponential instability. The potential provides the natural "mirror" missing for massless fields. In this limit, the calculation of the superradiance rates basically reduces to finding the tunneling exponent describing the suppression of the axion outside of the barrier compared to the near horizon region at $r_* = -\infty$, which is the horizon. See Ref. [37] for more details.

3.4 Spin Down and Mass Loss

The superradiance rate depends on the superradiance condition $(m\Omega_H - \omega)$. Since the BH loses spin during the growth of the cloud, superradiance for a specific l will stop at one point. We will estimate when this happens.

The energy for scalars in the n-th level is $\omega = \mu\left(1 - \frac{\alpha^2}{2n^2}\right) + \mathcal{O}(\alpha^4)$, but for now it is just set to $\omega = \mu$ again.[V] Plugging in the expression for Ω_H into the superradiance condition and and

[V] Including terms with α-dependence will make the result more precise, and we will do a full analysis considering also the α-dependence of the mass in Ch. 8.

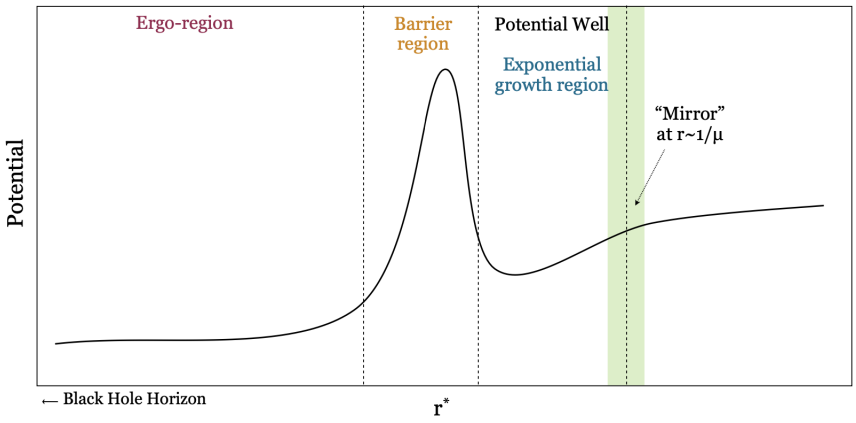

FIG. 3.3: The potential given in Eq. (3.3) for typical values. The potential well to the right of the barrier region makes bound states possible. Graphic taken from [37].

dividing by μ gives

$$1 - m\frac{\tilde{a}}{2\alpha(1-\sqrt{1-\tilde{a}^2})}\,, \tag{3.69}$$

which must be zero at $\tilde{a} = \tilde{a}_{\rm sat}$ when superradiance growth is exhausted. The solution for $\tilde{a}$ is

$$\tilde{a}_{\rm sat} = \frac{4m\alpha}{m^2+4\alpha^2}\,. \tag{3.70}$$

We see that for small α the $|211\rangle$ state reduces the BH spin down to $\tilde{a} \approx 4\alpha$, while the $|322\rangle$ spins it down further to $\tilde{a} \approx 2\alpha$. Note that when this happens, the superradiance rate of the $|211\rangle$ state turns negative, and this state begins to decay.

3.4.1 Mass of the Cloud

We can now also estimate, to which size the cloud actually will grow. We want to find $M_{\rm c}/M$, the ratio of cloud mass to BH mass. The final angular momentum of the fully grown cloud is given by the number of particles $M_{\rm c}/\mu$ times the angular momentum of a single particle m. The total angular momentum of the cloud will then be

$$L_c = \frac{M_{\rm c}}{\mu} m\,. \tag{3.71}$$

The angular momentum of a BH is $J = \tilde{a}GM^2$. Taking the result of the last section, if the BH is extremal in the beginning, i.e., $\tilde{a} = 1$ the $|211\rangle$ extracts approximately $J_{\rm ext,\,max} = (1-4\alpha)GM^2$ of angular momentum. We keep this factor general and impose that the cloud extracts $j < 1$ of the dimensionless spin of the BH, i.e., $J_{\rm ext} = jGM^2$. We then set this equal to the angular momentum of the cloud:

$$\frac{L_c}{J_{\rm ext}} \stackrel{!}{=} 1 = \frac{M_{\rm c}}{\mu} m \frac{1}{jGM^2}\,. \tag{3.72}$$

Solving this for M_c/M gives

$$\frac{M_c}{M} = \frac{j\alpha}{m}\,. \tag{3.73}$$

This bound is derived in vacuum. It can be relaxed in astrophysical environments due to accretion from surrounding matter [109]. For the fully realistic case of a BH-mass dependent α, we will take a closer look at the realistic mass of the saturated cloud in Ch. 8.

3.5 Phenomenology of Isolated Gravitational Atoms

While this thesis is concerned about the phenomenological prospects of a gravitational atom as part of a BBH, we also want to discuss the question if superradiance of ultralight particles cause observable effects for isolated BHs. There are two main possibilities: Observation of fast spinning BHs, and GW emission from the cloud itself. We are not going to discuss observable effects of clouds with self-interactions or couplings to other particles.

3.5.1 BH Spin Measurements and Scalar Mass Exclusion

Since the pure existence of an ultralight scalar in the spectrum of nature should start the superradiant instability for any highly spinning BH if the corresponding α allows the growth on short astrophysical timescales, the observation of highly spinning BHs could exclude the corresponding mass range of ultralight scalars. There is confirmed observation of spin of stellar BHs as well as of supermassive BHs. Therefore, bounds in the corresponding ultralight scalar mass range where clouds should be able to grow on astrophysical timescales have been put e.g., in Refs. [88, 89, 92, 110]. Spin measurements of individual BHs are based on X-ray measurements that relate to properties of the innermost stable circular orbit (ISCO) of the accretion disk. The ISCO is the radius at which matter in the disk stops orbiting and rapidly falls into the BH, and it is a monotonically decreasing function of $\tilde{a}$ that becomes steeper for $\tilde{a} \sim 1$. The size of the ISCO reflects in thermal emissions, used in the continuum fitting method [111], as well as in broadened iron emission lines, used in the reflection spectroscopy method [112]. We show the regions where ultralight scalars are supposedly excluded in Fig. 3.4. Only regions with large decay constant f_a (see Ch. 2) can be constrained, because at lower values, the self-interaction would be strong enough to destroy the cloud or inhibit its growth before the spindown can happen.

These results, if taken at face value, may imply that our studies of binaries with stellar-mass gravitational atoms can only be unsuccessful. Scalar masses between $\approx 10^{-12}\,\mathrm{eV} - 10^{-11}\,\mathrm{eV}$ corresponding to stellar mass BHs seem to be excluded. However, we mention here that these measurements come with big systematic uncertainties: How the inner region of the ISCO is modeled, how the atmosphere of the disc the photon crosses is modeled, and possible additional physical components that have not been included so far could all influence the deduced spin. In Ref. [113] it has been found that a high spin value of Cyg X-1 inferred by conventional models of $\tilde{a} > 0.9985$ can be reduced to $\tilde{a} = 0.92^{+0.07}_{-0.05}$ if the priors on radiative transfer in the disc atmosphere were relaxed. Allowing for a controversially discussed "warm" coronal component changed the best fit drastically

and lead to $\tilde{a} = 0.04^{+0.26}_{-0.04}$. While this may be an extreme example with a debated model, additional reason for skepticism towards the individual spin measurements comes from results from spin measurements via GW observation. A recent population study [114] from 70 BBH mergers detected as part of the Gravitational Wave Transient Catalog 3 (GWTC-3) [115] finds a spin distribution that peaks at $\tilde{a} \simeq 0.13^{+0.12}_{-0.11}$, while half of the individual BHs are found to have spins smaller than 0.25, with no evidence of any rapidly rotating BHs in the sample. There is no known reason why these independent methods of BH spin measurement would find such vastly different results. Therefore, we are going to assume that superradiance can happen for BHs in all of the mass range. Even if the spin measurements and with that the excluded boson mass ranges turn out to be solid, there is still the possibility to detect effects of superradiance for the much less studied and observed intermediate mass BHs [116].

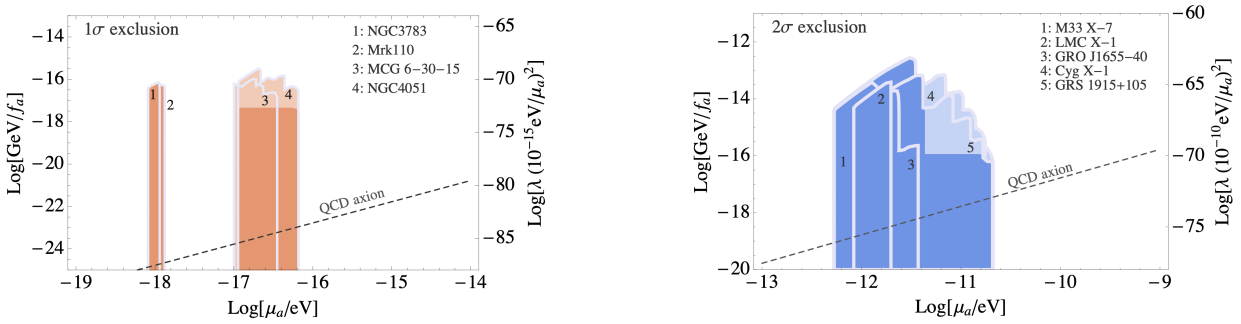

FIG. 3.4: Exclusion regions for ultralight scalars due to individually observed BH spins. Their large spin should not be possible if the superradiant clouds exist or once have existed in that mass range. The left plot shows exclusions from supermassive BHs, while the right plot shows stellar mass BHs. Graphic taken from Ref. [88].

3.5.2 Gravitational Wave-Emission from Annihilation

In any bosonic cloud, there is pair-annihilation of scalar particles into gravitons with rate Γ_a. Because of that, the cloud decays into GWs over time. The corresponding equation for the particle number is given by

$$\dot{N} = -\Gamma_a N^2 \,. \tag{3.74}$$

The solution to this is

$$N(t) = \frac{N_0}{1 + N_0 \Gamma_a t} \,. \tag{3.75}$$

The quantity $\tau_{\rm GW} \equiv (N_0 \Gamma_a)^{-1}$ is known as the decay time of the cloud, while we point out that this does not correspond to an exponential decay time. Typical values are [26, 88, 117]

$$\tau_{\rm GW,211} \approx 1.5 \times 10^8 \,{\rm yrs} \left(\frac{M}{10 M_\odot}\right) \left(\frac{0.07}{\alpha}\right)^{14} , \tag{3.76}$$

$$\tau_{\rm GW,322} \approx 1.5 \times 10^8 \,{\rm yrs} \left(\frac{M}{10 M_\odot}\right) \left(\frac{0.2}{\alpha}\right)^{18} . \tag{3.77}$$

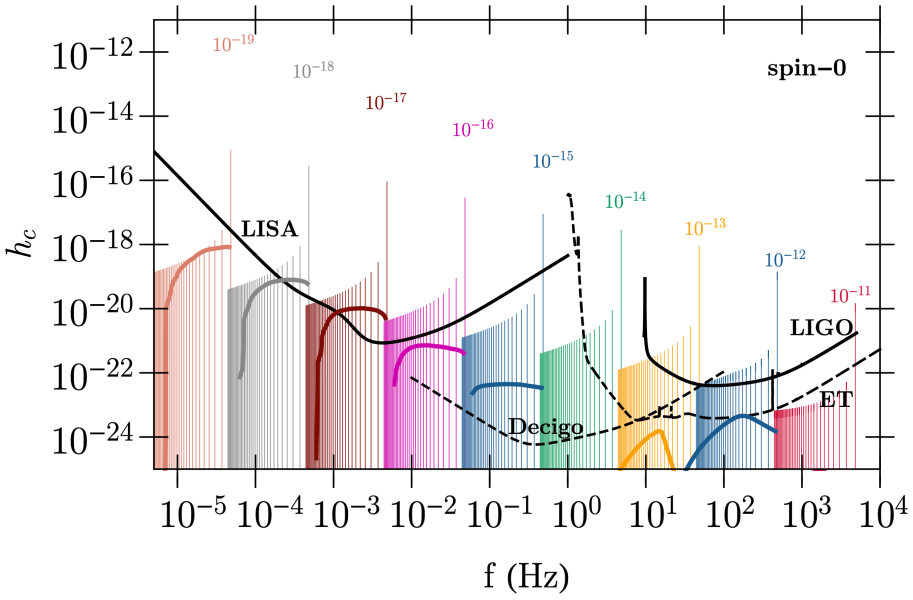

FIG. 3.5: GW strain produced by the clouds compared to the sensitivities of aLIGO and LISA (black thick curves) as well as DECIGO (dashed line), under the assumption of a coherent observation time of four years. Nearly vertical lines represent BHs with initial spin $\tilde{a} = 0.9$. Each line corresponds to a single source at redshift $z \in (0.001, 3.001)$ (from right to left), and the different colors correspond to different scalar masses. The thin lines show optimistic estimates of the stochastic background produced by the whole population of astrophysical BHs. Graphic taken from Refs. [87, 122].

The GW signal from the decaying cloud has frequency $f \simeq 2\mu/(2\pi) \simeq 10^3\,\mathrm{Hz}\left(\frac{\mu}{10^{-11}\,\mathrm{eV}}\right)$. Discussions on how to exclude certain boson masses via the non-observation of these monochromatic GW signals in LIGO and Virgo can be found in Refs. [118, 119]. It has been studied how more stringent constraints should be possible with aLIGO and LISA [87, 120, 121]. We show estimated GW strains compared to sensitivities of GW observatories in Fig. 3.5.

Chapter 4 Gravitational Atomic Physics

This chapter introduces a binary companion to the gravitational atom described in Ch. 3. To understand this system, we are first going to discuss how compact binaries evolve in GR. Instead of being described by stable Kepler orbits like in Newtonian physics, we will introduce radiation-reaction, leading to inspiral and decay of eccentricity. Cloud and companion cause tidal forces on one another, which gives rise to *gravitational atomic physics* [25, 26]. However, in contrast to actual atomic physics, where photons are usually assumed to radiate from or to infinity, the companion and the cloud are exchanging energy and angular momentum, meaning the atomic transitions of the cloud backreact onto the orbit, rendering the system non-linear and leading to the effects that will be investigated throughout the rest of this thesis. In this introduction we will focus on the resonant transitions in equatorial (meaning the spin of the BH and cloud are aligned with the angular momentum of the orbit) and circular orbits. We will also briefly discuss ionization. Based on the same framework as discussed here, in Ch. 5, we will study equatorial and eccentric orbits. In Ch. 7, we will drop all assumptions about the form of the orbit, and will aim to build a framework that captures the resulting dynamics consistently.

4.1 Basics of Compact Binaries

Einstein's equation in vacuum, Eq. (3.5), can be linearised around the flat space-time metric η, assuming that the perturbations are small

$$g_{\mu\nu} = \eta_{\mu\nu} + h_{\mu\nu}, \quad |h_{\mu\nu}| \ll 1. \tag{4.1}$$

In the Lorentz gauge, also called harmonic or De Donder gauge, the condition $\partial^\nu \bar{h}_{\mu\nu} = 0$ is satisfied, where we have defined $\bar{h}_{\mu\nu} \equiv h_{\mu\nu} - \frac{1}{2}\eta_{\mu\nu}\eta^{\alpha\beta}h_{\alpha\beta}$. In this gauge, the vacuum equation for the perturbation reduces to [123]

$$\Box\bar{h}_{\mu\nu} = 0\,. \tag{4.2}$$

The gauge choice has reduced the ten independent components of the metric to six, and this gauge is also valid when the right hand side is non-zero. In vacuum, one can apply the transverse-traceless

gauge, finding $h^{\rm TT}_{\mu\nu}$ and arrive at only two independent degrees of freedom. The equation then describes superposition of the two possible polarizations of gravitational waves in vacuum.

For clarity, we are going to restore c in this section. Coupling the GW equation, Eq. (4.2), to an energy density with finite spatial extent $T^{\mu\nu}$ that dynamically moves slowly compared to the speed of light $v \ll c$, one finds that the dominant contribution that is sourcing GWs comes from the transverse-traceless part of the quadrupole moment Q_{ij} of the energy density

$$[h^{\rm TT}_{ij}(t,\boldsymbol{x})]_{\rm quad} = \frac{1}{r}\frac{2G}{c^4}\ddot{Q}^{\rm TT}_{ij}(t-r/c), \tag{4.3}$$

where $Q^{ij} \equiv M^{ij} - \frac{1}{3}\delta^{ij}M_{kk}$ and $M^{ij} = 1/c^2\int d^3x T^{00}(t,\boldsymbol{x})x^i x^j$. This leads to a radiated power of

$$P_{\rm quad} = \frac{G}{5c^5}\left\langle \dddot{Q}_{ij}\dddot{Q}_{ij}\right\rangle. \tag{4.4}$$

A related calculation shows that angular momentum is also radiated for time-dependent quadrupoles. For details we refer to Ref. [123].

The power in Eq. (4.4) is the reason why two bodies in a binary emit GWs. This power scales with $(v/c)^5$, which is why this is referred to as an effect at 2.5 Post-Newtonian (PN) order. Conservative post-Newtonian corrections to Kepler orbits already appear at 1st and 2nd order, scaling with $(v/c)^2$ and $(v/c)^4$, respectively. They induce perihelion precession. Explaining the previously unaccounted part of Mercury's perihelion precession with the 1PN correction was one of the early successes of GR [124]. The radiation reaction of the orbit to Eq. (4.4) is the lowest order radiative effect, leading to the shrinking of the orbit. While the effect is minuscule and negligible for a system like the Earth orbiting the Sun, it is important when considering BBHs. For an eccentric BBH with semi-major axis a, where one of the BHs has mass M and the orbital companion has mass qM, we find for the radiated power[I]

$$P = \frac{32G^4M^5q^2(1+q)}{5c^5a^5}f(e), \tag{4.5}$$

where

$$f(e) \equiv \frac{1}{(1-e^2)^{7/2}}\left(1+\frac{73}{24}e^2+\frac{37}{96}e^4\right), \tag{4.6}$$

is a function of the eccentricity e. This function is unity for circular orbits and becomes much larger than unity only for eccentricities close to one. This means that highly eccentric orbits spiral in much faster. If one eliminates a in terms of frequency, a characteristic combination of M and q arises that defines the *chirp mass*

$$\mathcal{M}_{\rm ch} \equiv \frac{q^{3/5}}{(1+q)^{1/5}}M\,. \tag{4.7}$$

Since the orbital energy is given by

$$E_{\rm orb} = -\frac{qGM^2}{2a}, \tag{4.8}$$

[I] We note the identical notation for dimensionful spin of the rotating BH a from Ch. 3 and semi-major axis a. However, from now on, when we referring to the spin of the BH, we will always use the dimensionless spin $\tilde{a}$.

and semi-major axis and orbital frequency are related by $\Omega = \sqrt{\frac{GM(1+q)}{a^3}}$, we can find that the frequency evolution is given by

$$\frac{d\Omega}{dt} = f(e)\gamma_0 \left(\frac{\Omega}{\Omega_0}\right)^{11/3}, \tag{4.9}$$

with

$$\gamma_0 = \frac{96}{5c^5}\frac{q}{(1+q)^{1/3}}(GM\Omega_0)^{5/3}\Omega_0^2 \tag{4.10}$$

being related to the time scale of orbital evolution near any Ω_0 as reference frequency.

However, near such a reference frequency Ω_0, we can approximate the frequency evolution by a linear evolution and write

$$\Omega = \Omega_0 + \gamma_0 t. \tag{4.11}$$

This is the crucial ingredient for the orbital evolution to trigger the gravitational analogue of the Landau-Zener transition from atomic physics, which we will discuss in Sec. 4.3.1. In this thesis, we will often normalize both time and frequency with $\sqrt{\gamma_0}$, and introduce $w \equiv \Omega/\sqrt{\gamma_0}$ and $\tau \equiv t\sqrt{\gamma_0}$. With this, Eq. (4.9) becomes

$$\frac{dw}{d\tau} = f(e)\left(\frac{w}{w_0}\right)^{11/3}, \tag{4.12}$$

and for $e = 0 \rightarrow f(e) = 1$ has the solution

$$w(\tau) = \frac{3^{3/8} w_0^{11/8}}{(3w_0 - 8(\tau - \tau_0))^{3/8}}, \tag{4.13}$$

where $w(\tau_0) = w_0$. This solution shows that the frequency growth accelerates, until at the coalescence time

$$\tau_{\text{coal}} \equiv \tau_0 + \frac{3}{8}w_0 \tag{4.14}$$

the frequency diverges and the binary merges.[II] For any given orbital resonance, we will be interested in the behavior of the frequency relatively close to a given Ω_0. The analysis with dimensionless quantities shows that a *smaller* w corresponds to a Ω_0 that is closer to the merger. We will be interested in resonances far away from the merger, which means we have to do analyses demanding large numerical values, which holds non-trivial numerical challenges.

Eccentricity and magnitude of the angular momentum $\boldsymbol{L}$ of the orbit are related by

$$e^2 = 1 + \frac{2(1+q)E_o\boldsymbol{L}^2}{G^2M^5q^3}. \tag{4.15}$$

The GW emission of the orbit will also carry away angular momentum of the orbit. To derive the evolution of orbital eccentricity from this effect is non-trivial, and we refer to Ref. [123] for details. The most general result relating semi-major axis and eccentricity for a binary evolving in vacuum

[II] Ignoring here that the merger happens slightly before that due to the finite size of the horizons or compact objects.

is the relation [123, 125, 126]

$$a(e) = a_0 \frac{\tilde{g}(e)}{\tilde{g}(e_0)}, \tag{4.16}$$

where

$$\tilde{g}(e) = \frac{e^{12/19}}{1-e^2}\left(1+\frac{121}{304}e^2\right)^{870/2299}, \tag{4.17}$$

and where e_0 is the eccentricity of the orbit when the semi-major axis is a_0. This equation does not have an analytical solution for e unless we take certain limits. During the inspiral, a shrinks. When $a/a_0 < 1$, then $\tilde{g}(e)/\tilde{g}(e_0) < 1$ also holds. When eccentricity is small, $\tilde{g}(e) \approx e^{12/19}$. For general e, $\tilde{g}(e)$ is a monotonously growing function of e. This implies that orbits circularize while they shrink. This means we naturally expect orbits in the last phase of their inspiral to be almost circular. One of the main ideas of this thesis is that the interaction with the bosonic cloud offers a possibility to grow eccentricity and hence could make it possible to observe binaries with larger-than-expected eccentricity.

Deriving all of these effects relies on orbital averaging [123], and therefore can only be applied when the changes to the orbit are slow compared to the orbital frequency. The same will apply to the effects of the bosonic cloud that we will investigate. This means we still use the parameters commonly used to describe an unperturbed Newtonian Kepler orbit to describe the evolving orbit. These parameters are describing the orbit an object would have if all perturbations would vanish, called an *osculating orbit*.

Due to the observational possibilities of planned GW observatories, BBHs offer a plethora of possibilities to understand astrophysical environments as well as to test fundamental physics. Notably, the masses, spin alignment, and eccentricity are expected to be correlated with formation channels, where *isolated* formation leads to spins aligned with the orbital angular momentum, while *dynamically* formed binaries and ones that undergo a *common envelope* phase often have misaligned spins, e.g., Refs. [127–145].

4.2 Gravitational Wave Observatories

The first detection of gravitational waves occurred in September 2015 [5] by the LIGO interferometers. Since then, more than a hundred other events have been confirmed by LIGO working together with VIRGO [146] and KAGRA [147]. However, the frequency range of 10 Hz to 10^3 Hz and GW strain sensitivity only makes it possible to detect the late phase of mergers of compact objects of 1 to 100 solar masses. Planned future ground-based observatories like the Einstein Telescope [8] and Cosmic Explorer [10] are supposed to improve that sensitivity while staying in a similar frequency range. By contrast, the space-based interferometer LISA (Laser Interferometer Space Antenna) [7] is planned to extend the sensitivity toward the millihertz band, 10^{-4} Hz-10^{-1} Hz. At these frequencies, one expects the mergers of massive black hole binaries, EMRIs (Exteme Mass Ratio Inspirals), white dwarfs in our galaxy, as well as the inspiral phase of stellar mass BBHs. The latter is the main interest of this thesis, because the transitions between the cloud states we are interested in roughly fall into the LISA-band. Decihertz detectors like DECIGO [12] are supposed to brigde the

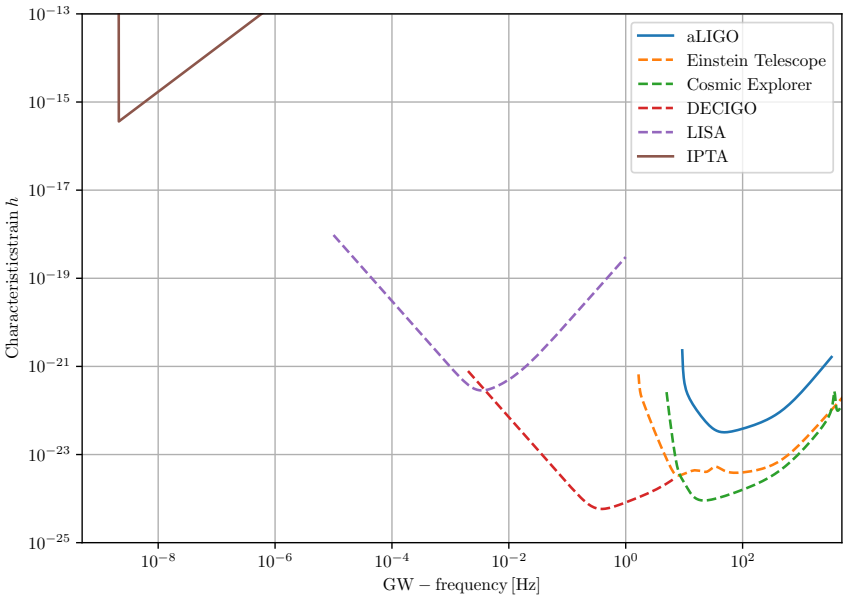

FIG. 4.1: Sensitivities and frequency range of some relevant working (solid) and planned (dashed) GW observatories. The data for the curves has been provided by Ref. [149].

gap between the ground-based observatories like ET and LIGO, and space-based observatories like LISA. We add for completeness that there is also ongoing research into the nanohertz-band by various pulsar timing arrays (PTAs), using the angular dependence of timing residuals of a collection of pulsars to infer a GW background. Growing evidence for such a background was announced in 2023 [148]. We display the sensitivity curves for these most important existing and planned GW observatories in Fig. 4.1.

4.3 Gravitational Atomic Physics in Circular, Equatorial Orbits

If one constituent of a BBH carries a bosonic cloud, the companion will, very generally, present a perturbation in the metric that induces mixing between the states. For a bosonic cloud around an isolated BH and in the absence of self-interactions, modes of different quantum numbers n, l, m do not interact. This is because the background spacetime is axisymmetric and time-independent, with an effectively monopolar potential. As a result, the wave equation separates into angular and radial parts, and different modes evolve independently. Adding the companion introduces a time-dependent, non-axisymmetric, multipolar gravitational perturbation to the background spacetime. This allows different angular momentum modes to couple and exchange energy. The most dramatic effect of this is resonant level mixing, when the orbital frequency matches the energy difference between any two states $|a\rangle$ and $|b\rangle$, $\Delta\epsilon \equiv \epsilon_b - \epsilon_a$ divided by the angular momentum difference $\Delta m \equiv m_b - m_a$.

In the first paper discussing superradiance in binaries [25], it was assumed that the metric perturbation induced by the companion could, for short timescales, be approximated as having constant frequency, such that at the point in the orbital evolution where the resonant condition

$$\Omega_{\rm res} \equiv \frac{\Delta\epsilon}{\Delta m}\,, \tag{4.18}$$

is fulfilled, the perturbation will lead to Rabi oscillations between the two states. Since one of the states would be the (saturated) superradiant state, while the other one is a decaying state, this resonance could partially deplete the cloud by dipping into the decaying state during the oscillations. If the orbit stays close to the resonance long enough, it could destroy the cloud completely. Any backreaction of the energy transfer to the orbit was not considered. However, the orbital frequency is not fixed, but it grows, and at no point during the inspiral it can be assumed to be "fixed"; instead, it always grows approximately linearly, $\Omega(t) \approx \Omega_0 + \gamma_0 t$. It was realized in Ref. [26] that such a linearly growing frequency does NOT induce Rabi oscillations, but a "one-way" transition from one state to the other in a so-called *Landau-Zener (LZ) transition* [150, 151]. This paper also considered for the first time that there is energy and angular momentum exchange between the cloud and the orbit during these transitions. It was concluded that the decay rate of the states was small enough such that not only the transition could proceed uninterrupted and that the decaying state could be fully occupied, but also that the decaying state could survive until it encounters another transition itself. Even for narrow resonances, this treatment is incomplete.

In this introductory chapter, we will discuss resonant LZ-transitions between bound states on equatorial and circular orbits, their backreaction to the orbit, as well as very briefly the effect of ionization, which is the excitation of bound states into unbound states and happens inside the cloud and is the equivalent to dynamical friction [27, 152, 153]. In the main parts of the thesis, we will discuss transitions to decaying states in eccentric, equatorial orbits [1, 154] in Ch. 5, as well as in general orbits in Ch. 7. General orbits include inclined orbits, which have been elaborated in Ref. [27, 152–154]. However, a main point of the third part of this thesis will be to show how these discussions have been incomplete due to an inconsistent treatment. In Ch. 8, we will also study non-resonant mixing due to strong decay rates [155].

4.3.1 Gravitational Mixing and Landau-Zener Transitions

We write a general bound state of the cloud as $|\psi(t)\rangle = \sum_i c_i(t)\,|i\rangle$, where $0 < c_i < 1$ is the complex amplitude of the i-th state and $|c_i|^2$ its relative occupation density. The inner product of these states is defined as

$$\langle nlj|n'l'm'\rangle \equiv \int d^3x \psi^*_{nlm}(t,\boldsymbol{r})\psi_{n'l'm'}(t,\boldsymbol{r}) = \delta_{nn'}\delta_{ll'}\delta_{mm'}\,. \tag{4.19}$$

Before any transition occurs, we are usually assuming that just one c_i, corresponding to a state experiencing superradiance, is non-zero. While at the same time as $|211\rangle$ experiences superradiance also states $|n11\rangle$, with $n > 2$ are growing, their growth rates are much smaller than $|211\rangle$, so it is fine to assume the latter to be dominating one. If we ignore the decay or growth of states, we will

have $\sum_i |c_i(t)|^2 = 1$. The Schrödinger equation Eq. (3.46) describing the evolution of the cloud can then be rewritten in terms of the occupation densities:

$$i\partial_t \sum_i c_i(t)\,|i(\boldsymbol{r})\rangle = \left(-\frac{1}{2\mu}\boldsymbol{\nabla}^2 - \frac{\alpha}{r}\right)\sum_i c_i(t)\,|i(\boldsymbol{r})\rangle\,, \tag{4.20}$$

$$\Rightarrow i\sum_i \dot{c}_i(t)\,|i(\boldsymbol{r})\rangle = \sum_i c_i(t)\epsilon_i\,|i(\boldsymbol{r})\rangle\,, \tag{4.21}$$

where ϵ_i is the energy of the ith-state. Multiplying from the left with $\langle i|$, using the orthogonality of the states $\langle i|j\rangle = \delta_{ij}$ and allowing for a possible mixing of the states via off-diagonal terms leads to

$$i\frac{dc_i}{dt} = \sum_j \mathcal{H}_{ij}(t)c_j, \tag{4.22}$$

with the Hamiltonian $\mathcal{H}_{ij} = \epsilon_i\delta_{ij} + V_{ij}(t)$, where V_{ij} is a term allowing mixing induced by a perturbation.[III] For us this arises from the perturbation by the binary companion.

For this, we will work in spherical coordinates aligned with the cloud, with coordinates (r, θ, ϕ). The binary companion is located at $\boldsymbol{R}_\star(t) \equiv \{R_\star(t), \Theta_\star(t), \varphi_\star(t)\}$ and has mass $M_\star$. The gravitational potential of the companion for the scalar field μ is

$$V_\star(t, \boldsymbol{r}) = -\frac{GM_\star\mu}{|\boldsymbol{R}_\star - \boldsymbol{r}|} \tag{4.23}$$

which can be decomposed into multipoles with the Laplace expansion [25]:

$$\begin{aligned} V_\star(t, \boldsymbol{r}) = -GM_\star\mu \sum_{l_\star\geqslant 2}\sum_{|m_\star|\leqslant l_\star} \frac{4\pi}{2l_\star+1} Y^*_{l_\star m_\star}(\Theta_\star, \varphi_\star)Y_{l_\star,m_\star}(\theta,\phi) \\ \times\left(\frac{r_\star^l}{R_\star^{l_\star+1}}\Theta(R_\star - r) + \frac{R_\star^{l_\star}}{r^{l_\star+1}}\Theta(r - R_\star)\right)\,, \end{aligned} \tag{4.24}$$

where we have used the expression of the spherical Legendre polynomials via spherical harmonics using the spherical harmonic addition theorem. $\Theta(x)$ is the Heaviside-function. For equatorial orbits we have $(\Theta_\star = \pi/2)$ for which the spherical harmonic depending on the companion's coordinates, $Y^*_{l_\star m_\star}(\Theta_\star, \varphi_\star)$, becomes a prefactor times an oscillatory term, $e^{im_\star\varphi_\star}$, which will be the crucial ingredient for the resonance.

To find the mixing between any two states $|i\rangle$ and $|j\rangle$, we have to calculate the matrix element $V_{ij}(t)$ in $\mathcal{H}_{ij}$ via $\langle j|\,V_\star\,|i\rangle = \int d^3x\psi^*_{n_jl_jm_j}V_\star\psi_{n_il_im_i}$.

For resonances triggered when the companion is far from the cloud, $R_\star \gg r_c$, we may neglect the part with $\Theta(r - R_\star)$, since in that region, the wavefunctions of the states will be exponentially suppressed. We define $\mathsf{r} \equiv r/r_c$ and $\mathsf{R}_\star \equiv R_\star/r_c$ and rewrite $GM_\star\mu = \frac{GM\mu M_\star}{M} \equiv q\alpha$, where we have

[III] It is *not* the central radial potential from Eq. (3.46).

defined $q \equiv M_\star/M$. With this, the tidal interaction is given by [25, 26]

$$\langle b|\, V_\star\, |a\rangle \equiv \sum_{l_\star=2}^{\infty} \sum_{|m_\star|\leqslant l_\star} \eta_{ab}^{(\star)} e^{-im_\star\varphi_\star}\,, \tag{4.25}$$

$$\eta_{ab}^{(\star)} = -\frac{q\alpha}{r_{\rm c}} \mathsf{R}_\star^{-(l_\star+1)} \frac{4\pi}{2l_\star+1} \left|Y^*_{(\star)}\left(\frac{\pi}{2},\varphi_\star\right)\right| I_r I_\Omega\,,$$

$$I_r \approx \int^{\infty} d\mathsf{r}\mathsf{r}^2 \hat{\mathcal{R}}_b \hat{\mathcal{R}}_a \mathsf{r}^{l_\star} \tag{4.26}$$

$$I_\Omega \equiv \int d\Omega Y_b^*(\theta,\phi) Y_{(\star)}(\theta,\phi) Y_a(\theta,\phi)\,, \tag{4.27}$$

$$\tag{4.28}$$

where $(\star) \equiv (l_\star, m_\star)$, and $\hat{\mathcal{R}}_c = r_{\rm c}^{3/2}\mathcal{R}_c$ is the (dimensionless) hydrogenic radial wavefunction. We note that this formula is true for all the terms in the expansion with $l_\star \geqslant 2$, while for $l_\star = 1$, a different formula applies that makes the mixing only non-zero when the companion is inside the cloud.[IV]

The integral I_r gives the strength of the mixing, which is determined by the overlap of the wavefunctions. Note that for simplicity, we took the limit of the integral to be ∞, since if the companion is far away, the radial wavefunctions are strongly suppressed for large r anyway.

The second integral, I_Ω does not depend on the position of the companion, has a well-known analytic solution, and for given states $|a\rangle$ and $|b\rangle$ determines, which terms of the infinite sum in Eq. (4.24) actually can contribute to the mixing. It is only non-zero if the following selection rules are satisfied:

$$\begin{aligned} &\text{(S1)} \quad m_\star = m_b - m_a, \\ &\text{(S2)} \quad l_a + l_\star + l_b = 2p, \quad \text{for } p \in \mathbb{Z}, \\ &\text{(S3)} \quad |l_a - l_b| \leqslant l_\star \leqslant l_a + l_b. \end{aligned} \tag{4.29}$$

Transitions from states where only m changes have the smallest difference in energy and happen first in the orbital evolution. They are called *hyperfine* transitions. *Fine* transitions are defined by $n_a = n_b$, but $l_a \neq l_b$. The transitions where n changes are called *Bohr* transitions, as in atomic physics. The selection rules show us which terms we need to take into account. For example for the fastest growing $|211\rangle$ state, there could be hyperfine transitions to $|21-1\rangle$ and $|210\rangle$. The selection rules make clear that $|211\rangle \to |21-1\rangle$ needs $l_\star = 2$, because it needs to be even, but cannot be larger than two. So the quadrupole term, $l_\star = 2$, is the only one contributing, with necessarily $m_\star = -2$. This makes the overlap non-zero, but mediated by only one term in the multipole expansion. In contrast $|211\rangle \to |210\rangle$ needs to be mediated by the quadrupole perturbation, $l_\star = 2$ as well, however, the m selection rule tells us that $m_\star = -1$. While $I_\Omega \neq 0$, the spherical harmonic $Y^*_{2,-1}(\pi/2,\varphi_\star) = 0$, which makes this hyperfine transition only possible for inclined orbits.

We are now going to consider a system with only two states, $|a\rangle$ and $|b\rangle$ with non-zero mixing η. The two-state approximation assumes all the other resonances are too far away in frequency space

[IV] For details on the dipole $l_\star = 1$ interaction see Refs. [154, 156–158].

to be relevant. The exceptions to that assumption will be discussed in Ch. 8. We are also going to assume that one state is fully populated due to superradiance, while the other is unpopulated. We are also going to ignore decay rates for now, which will be considered in Ch. 7. For this system, the Hamiltonian reduces to

$$\mathcal{H} = \begin{pmatrix} -\frac{\Delta\epsilon}{2} & \eta_{ab}(t)e^{i\Delta m\varphi_\star(t)} \\ \eta_{ab}(t)e^{-i\Delta m\varphi_\star(t)} & \frac{\Delta\epsilon}{2} \end{pmatrix}, \tag{4.30}$$

with $\Delta\epsilon = \epsilon_b - \epsilon_a$ and $\Delta m = m_b - m_a$. It is possible to write the diagonal terms just in terms of the energy difference, because we can always multiply a constant, in this case $-(\epsilon_b + \epsilon_a)/2$. The off-diagonal contains no sum, as we either find that only one term from the multipole expansion contributes, or we assume that only one mixing term is most dominant.

From this Hamiltonian it is not directly obvious why there are resonant transitions between the states. The exponential functions in the off-diagonal terms are oscillating heavily, which one would also expect for the corresponding small mixing between the states. However, we can transform the system into the *dressed frame*, the frame that co-rotates with the companion. This can be done via the time-dependent unitary transformation

$$\mathcal{U}(t) = \begin{pmatrix} e^{i\Delta m\varphi_\star/2} & 0 \\ 0 & e^{-i\Delta m\varphi_\star/2} \end{pmatrix}. \tag{4.31}$$

We have assumed that the orbit is equatorial and circular, which means that the general coordinate of the companion $\varphi_\star$ becomes identical to the mean anomaly of the orbit (for details see Sec. 5.2) which is related to the orbital frequency by $\dot{\varphi_\star}(t) = \Omega(t)$. With that, the Hamiltonian in the dressed frame becomes

$$\mathcal{H}_{\mathrm{D}}(t) = \mathcal{U}^\dagger\mathcal{H}\mathcal{U} - i\mathcal{U}^\dagger\frac{d\mathcal{U}}{dt} = \begin{pmatrix} (\Delta m\Omega(t) - \Delta\epsilon)/2 & \eta_{ab}(t) \\ \eta_{ab}(t) & -(\Delta m\Omega(t) - \Delta\epsilon)/2 \end{pmatrix}. \tag{4.32}$$

Since the transformation is unitary, any transformation of the occupation amplitudes c_i is physically equivalent, and the occupation densities in the dressed frame Hamiltonian coincide with those in the original frame. [26]

The resonance condition Eq. (4.18) now becomes explicit: It is the orbital frequency for which the diagonal terms vanishes and only the off-diagonal terms, which now also don't oscillate anymore.

Close to any reference frequency, the behavior of the frequency is approximately linear, $\Omega(t) \approx \Omega_0 + \gamma_0 t$ and we can now set $\Omega_0 = \Omega_{\mathrm{res}}$. For the rest of the thesis, we will always write Ω_0 to refer to a specific resonance frequency. We also assume that $\eta_{ab}(t)$ is constant ($\to \eta$) during the resonance, because the orbit is circular and the inspiral happens relatively slowly. The dressed Hamiltonian of the linearised problem then becomes

$$\mathcal{H}_{\mathrm{D,\,lin}}(t) = \frac{\gamma_0 t}{2}\begin{pmatrix} 1 & 0 \\ 0 & -1 \end{pmatrix} + \eta\begin{pmatrix} 0 & 1 \\ 1 & 0 \end{pmatrix}. \tag{4.33}$$

The energy eigenvalues of this Hamiltonian are $\epsilon_\pm(t) = \pm\sqrt{(\gamma_0 t/2)^2 + \eta^2}$, while the eigenstates are

$$|\epsilon_\pm(t)\rangle = \mathcal{N}_\pm^{-1}(\gamma_0 t/2 \pm \sqrt{(\gamma_0 t/2)^2 + \eta^2}, \eta)\,, \tag{4.34}$$

where $\mathcal{N}_\pm$ are appropriately chosen normalization constants. Careful investigation of the behavior in the infinite past and infinite future shows

$$|\epsilon_+(-\infty)\rangle = (0,1), \quad |\epsilon_-(-\infty)\rangle = -(1,0)\,, \tag{4.35}$$

while

$$|\epsilon_+(+\infty)\rangle = -\,|\epsilon_-(-\infty)\rangle\,, \quad |\epsilon_-(+\infty)\rangle = |\epsilon_+(-\infty)\rangle\,. \tag{4.36}$$

As a result, due to the mixing term, the two eigenstates permute their identities. This implies that as long as the transition happens slow enough, i.e., adiabatic, such that the system can track its instantaneous eigenstates, a system that starts with a fully populated state $|a\rangle$ completely transfers its population to state $|b\rangle$. This is the *Landau-Zener* (LZ) transition.

In the infinite future, after the transition, we have

$$|\langle\epsilon_+(\infty)|\psi(\infty)\rangle|^2 = e^{-2\pi z}, \tag{4.37}$$

where z is the Landau-Zener parameter defined as

$$z \equiv \frac{\eta^2}{\gamma}. \tag{4.38}$$

The exponential behavior shows that if z is larger than unity, we have a full transfer of the population. This happens in a smooth way. For smaller z, the transition is not total, while the incompletely transferred states oscillate. Two examples are shown in Fig. 4.2.

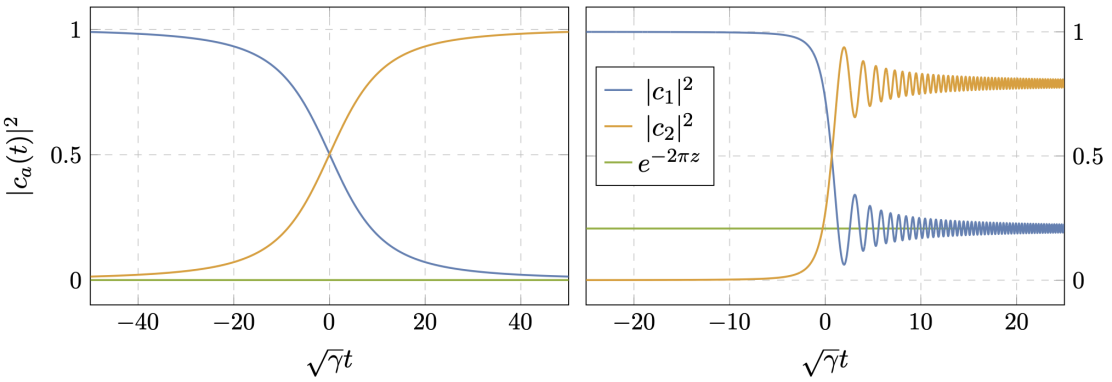

FIG. 4.2: Examples of the population transfer during Landau-Zener transitions. *(left):* Adiabatic transition with $z > 1$, *(right):* Non-adiabatic, $z < 1$. Graphic taken from [26].

4.3.2 Backreaction Onto the Orbit

So far, we have treated the orbital frequency as independent of the transition. While this is reasonable for LZ-transitions in atomic physics, where an external source of electromagnetic radiation can drive the transition in an atomic system, this is not true in our system. During the transition, the cloud gains or loses angular momentum and energy and this necessarily leads to a *backreaction* onto the orbit.

We can understand the backreaction by writing a full balance equation for the energy in the orbit, the cloud and the dissipation term due to GWs[V]

$$\dot{E}_{\rm o} + \dot{E}_{\rm c} = \mathcal{F}_{\rm GW} \equiv -\frac{32}{5}\frac{G^4 M^5 q^2 (q+1)}{a^5}\,, \tag{4.39}$$

where a is the semi-major axis. The orbital energy is given by $E_{\rm o} = -\frac{GM^2 q}{2a}$, while for the cloud the energy is a sum over the populated states, $E_{{\rm c}(i)} \equiv (M_{\rm c,0}/\mu)\epsilon_i |c_i|^2$.

With $\Omega = \sqrt{\frac{GM(1+q)}{a^3}}$, the above equations can then be rewritten as

$$\frac{d\Omega}{dt} = r\gamma_0 \left(\frac{\Omega}{\Omega_0}\right)^{11/3}\,, \tag{4.40}$$

$$r \equiv \frac{\dot{E}_{\rm o}}{\mathcal{F}_{\rm GW}} = 1 - b\frac{{\rm sgn}(\Delta m)\left(\frac{\Omega}{\Omega_0}\right)^{-11/6}}{\sqrt{\gamma_0 |\Delta m|}}\frac{d|c_a|^2}{dt}\,, \tag{4.41}$$

in terms of the orbital parameters, where

$$b \equiv \frac{3M_{\rm c,0}}{M}|\Delta m|^{3/2}\left(\frac{\Omega}{\Omega_0}\right)^{-3/2}\frac{(1+q)^{1/3}}{\alpha q}\frac{(GM\Omega_0)^{1/3}\,\Omega_0}{\sqrt{\gamma_0}}\,. \tag{4.42}$$

These are the equations for the full non-linear inspiral. Treating the inspiral as linear, and setting $\Omega(t) = \Omega_0$ close to the resonance, significantly simplifies these equations, as it has been done in Ref. [26, 154]. Because backreaction modifies r to be different than unity as soon as the transition starts at $d|c_a|^2/dt < 0$, the inspiral can happen faster or slower, depending on the kind of transition. This changes the effective $\gamma_{\rm eff} \neq \gamma_0$. That means that an "effective" LZ-parameter emerges: $\zeta(t) \equiv z/r(t)$, making it a fully nonlinear system. We see that b is always positive, $d|c_a|^2/dt$ is negative during the transition. So if we have a transition on a co-rotating orbit in which the cloud loses energy $\Delta\epsilon < 0$, and Δm is negative, during the transition the backreaction reduces r towards zero. When $r = 0$, the backreaction effectively counterbalances the GW emission of the orbit and hence the frequency stalls during the transition, $\dot{\Omega} = 0$. We call this behavior a *floating orbit*. Since the effective LZ-parameter becomes large, even if z is small, a formally non-adiabatic transition can become adiabatic due to the backreaction.

[V] We are ignoring decay rates, hence also the backreaction of the BH. Also, we are only interested in orbital energy, because we only investigate circular and equatorial orbits here.

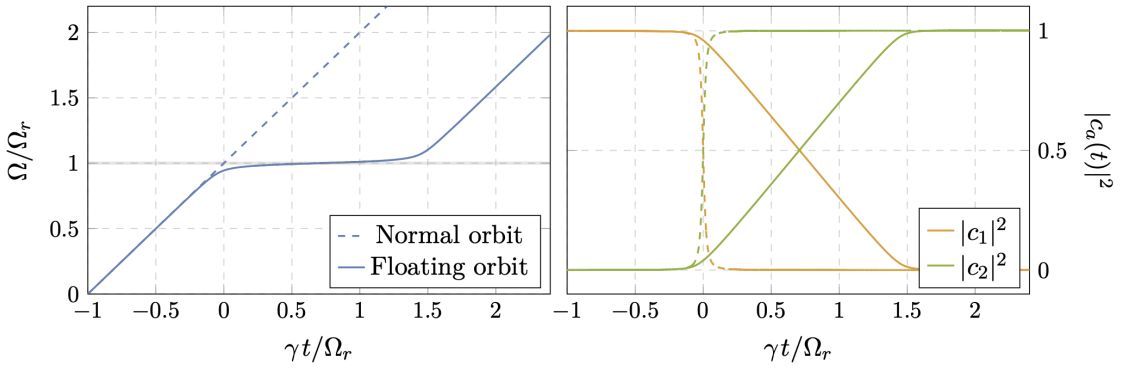

FIG. 4.3: Comparison of LZ-transitions without (dashed lines) and with backreaction (solid lines) showing orbital frequency *(left)* and occupation densities *(right)*. The backreaction leads to a stalling of the orbit, i.e., *floating*, during which the population transfer happens in a linear fashion. Graphic taken from [26].

The opposite thing happens when the cloud gains energy $\Delta\epsilon > 0$, which is only possible on co-rotating orbits if $\Delta m > 0$. During such a transition $r > 1$, and the inspiral happens faster than in vacuum. This will make the inspiral faster during the transition, which is why these are called *sinking orbits*. Such a transition also reduces the effective LZ-parameter, even if z is large. This means, due to backreaction a formally adiabatic transition could become non-adiabatic. An example of how backreaction changes the transition for a floating orbit is shown in Fig. 4.3. We will discuss this system as well as its generalization in detail in Ch. 5.

We point out that the scaling with frequency in Eq. (4.40) has a different power if the balancing is not done with orbital energy, but with angular momentum, $(\Omega/\Omega_0)^{1/3} \to (\Omega/\Omega_0)^{4/3}$. This explains the difference between Ref. [26] and Ref. [154]. However, the latter has used $\Omega(t) = \Omega_0$ near the resonance anyway. These differences would only be important far away from the resonance. For circular orbits, both approaches seem to lead to self-consistent results. We discuss in detail in Ch. 7, why these two results are inconsistent.

4.4 Ionization of Gravitational Atoms

Although we will not consider this process in this thesis, an important phenomenon of the perturbation induced by the binary companion is the induction of transitions from the bound state of the cloud to unbound states $|k; lm\rangle$, where k refers to a positive and continuous momentum. This process was first studied in Ref. [27]. We can only sketch the most important aspects here.

To understand the mechanism, we can write the general wavefunction as a linear combination of one bound state and the continuum as

$$|\psi(t)\rangle = c_{n_b l_b m_b}(t)\,|n_b l_b m_b\rangle + \int \frac{dk}{2\pi} c_{k;lm}\,|k; lm\rangle\,. \tag{4.43}$$

The occupation densities of the continuum states can then be computed as

$$c_{k;lm}(t) = -\int_0^t dt' \langle k; lm | V_\star(t', \boldsymbol{r}) | n_b l_b m_b \rangle e^{i(\epsilon(k)-\epsilon_b)t'} = i\eta \frac{1 - e^{i(\epsilon(k)-\epsilon_b-g\Omega)t}}{i(\epsilon(k) - \epsilon_b - g\Omega)}\,, \tag{4.44}$$

where η is defined as before. Here $\epsilon(k)/\epsilon_b$ refer to the non-relativistic energy of the continuum state and bound state, respectively. For the last equality it has been used that only the terms that oscillate with $g\Omega$ survive, where $g = m - m_b$. Averaging this expression over time gives rise to a delta function:

$$|c_{k;lm}|^2 = 2\pi t |\eta|^2 \delta(\epsilon(k) - \epsilon_b - g\Omega)\,. \tag{4.45}$$

When writing out the full result for the ionization rate, the delta function leads to a stepwise behavior. The rate is given by

$$\frac{\dot{M}_c}{M_c} = -\sum_{l,g} \frac{\mu |\eta^{(g)}|^2}{k_{(g)}} \Theta(k^2_{(g)}), \tag{4.46}$$

where $k_{(g)} \equiv \sqrt{2\mu(\epsilon_b + g\Omega)}$ and $\Theta(x)$ is the Heaviside function. In Ref. [27] it has been found that for a wide range of orbital separations, all near r_c, the power from ionization is larger than the power of emitted GWs, which means for this range ionization would be the domination contribution for the inspiral, making the latter proceed much faster than in vacuum. This in turn effectively turns the resonant transitions between bound states, in the Bohr regime, less adiabatic, rendering them almost negligible for the binary evolution [154].

One of the main features of ionization are the sharp features in the ionization power as a function of orbital frequency, which is a direct result of the Heaviside-function in Eq. (4.46). In the simplified discussion, these features materialize as discontinuous peaks that arise when $g\Omega = -\epsilon_b$ which is fulfilled for

$$\Omega^{(g)} = \frac{\alpha^3}{2gMn_b^2}, \qquad g \in \mathbb{N}_+\,. \tag{4.47}$$

These can be understood as threshold frequencies to excite an unbound state, analogous to the photoelectric effect. It has been shown in Ref. [153] that, neglecting the peaks, the overall shape of the ionization power is closely related to the dynamical friction that the binary companion would experience inside a cloud of point particles with the same density as the bosonic cloud. In that sense, ionization is the ultralight scalar equivalent of dynamical friction.

Part II

Phenomenological Treatment of Superradiance in Binaries with Eccentric and Equatorial Orbits

Chapter 5 Resonant Transitions to Decaying States in Eccentric Orbits

5.1 Overview

In the papers discussed in Ch. 4, the backreaction effects of level transitions between the cloud's states were studied under the simplifying assumption of planar, quasi-circular orbits. The reasoning for that was twofold [25]. First, several formation scenarios for BBHs lead to spins of the central BH that are aligned with the orbital angular momentum [132]. Second, since there is decay of eccentricity through GW emission in vacuum during the inspiral [125, 126], it is expected that in later stages of the BBH dynamics, the orbit has circularized.

In this part of the thesis, we keep the assumption that the orbit is aligned with the central black hole spin, but we discard the assumption that the orbit is circular. Adding eccentricity both introduces a series of *overtones* [153, 159] and can have dramatic influence in the orbital dynamics during the transition. These effects can leave a lasting imprint on the orbit, leading, for a specific system, to larger eccentricities than would be expected in the late stages of the inspiral.

The strength of the additional overtones is suppressed by eccentricity, to higher order the further you depart from the original resonance. Still, a small departure from circularity can trigger transitions that would not only deplete the cloud, but in the case of floating resonances also induce a growth of eccentricity toward a large fixed-point, i.e., critical value of about $e_{\rm cr} \in [0.3, 0.6]$. Measurements of larger-than-expected eccentricities could then provide strong evidence for the existence of an ultralight particle in nature.

In this chapter, we will introduce and investigate the theoretical framework of the transitions in an eccentric binary, while in Ch. 6, we are going to apply this formalism to a typical BBH population formed in isolation.

For this chapter, we keep the definitions of α, ϵ_{nlm} and the states themselves as they have been introduced in Ch. 3. Building on that, we will expand the formalism explained in Ch. 4 to capture eccentric equatorial orbits, as well as to include the effect of transitions to decaying states.

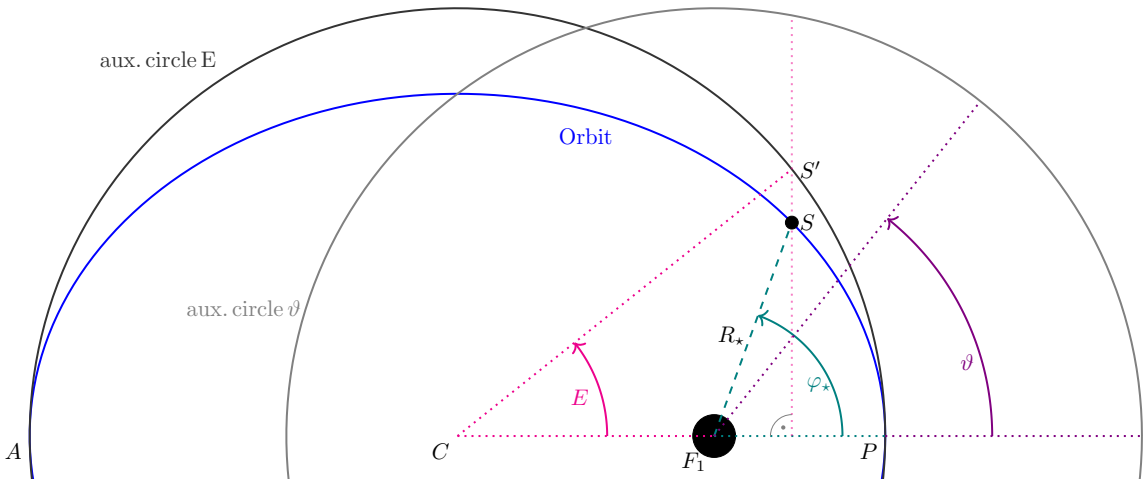

FIG. 5.1: Visualization of the three anomalies. The central object is at F_1 and the companion on the blue orbit at point S. The actual angle of the companion with respect to the central object and periastron P is the true anomaly $\varphi_\star$ in green. Note the auxiliary circle around the center C to geometrically define the eccentric anomaly E (magenta), and the auxiliary circle around F_1 to define mean anomaly ϑ (violet) from Kepler's law. Note that in this example ϑ is smaller than $\varphi_\star$, because near the periastron, the companion moves much faster than the same object would on a circular orbit with the same orbital frequency. See the description in the text for details.

5.2 Anomalies in Eccentric Orbits

For historic reasons, the angular variables in the Kepler problem used to describe the current position of the orbiting object with respect to some reference point of the orbit are called **anomalies**. We briefly review the definition of the three different anomalies *true anomaly*, *eccentric anomaly* and *mean anomaly* and their relations. We are considering the conventional description of the orbit in the Kepler problem: Instead of describing two objects from the inertial frame centered at their center-of-mass (com) which is orbited by both objects, we choose one object's reference frame (usually the frame attached to the heavier mass is chosen), orbited by an object with reduced mass $\mu \equiv MM_\star/(M + M_\star)$. In an elliptic orbit, there are two foci, F_1 and F_2, and on one of these two sits the central object, let it be on F_1. In the middle of the two foci is the center of the ellipse C. The length of the two line segments from C to the two farthest points of the ellipse is called the semi-major axis a. The two foci lie on these line segments. The distance from F_1 to the closest point of the ellipse is $a(1 - e)$, where $0 < e < 1$ is the eccentricity of the orbit. This point on the ellipse is called periapsis, here P, and is the point of closest approach. The length of the line segment from F_1 to the furthest point of the ellipse, going through F_2 is $a(1 + e)$ and this point is called apoapsis[I], here A, the point of maximum distance. Let the point on the ellipse where the

[I] These points are often called *apo- /periastron* for orbits around a star and *apo-/perihelion* for orbits around the Sun.

companion is located be called S.

- The true anomaly $\varphi_\star$ is the angle between $\overline{F_1P}$ and $\overline{F_1S}$.
- Imagine an auxiliary circle centered at C with radius a. This means it touches the orbit at P and A. The eccentric anomaly E is the angle between $\overline{CP}$ the $\overline{CS'}$, where S' is the point closest to S on the auxiliary circle that lies on the line that includes S and is perpendicular to $\overline{CP}$.
- Imagine a circular orbit centered at F_1 with radius a. Due to Kepler's law, this orbit will have the same orbital frequency Ω as any eccentric orbit with the same a. The mean anomaly is now $\vartheta \equiv \Omega(t - t_0)$, with t_0 being the time at which the companion is at P. The mean anomaly ϑ is not geometrically related to the true anomaly, it is fictitious angle increasing linearly in time for uniform motion on a circular orbit, and not geometrically related to the actual position of the object.

Note that for $\varphi_\star = \{\pi, 2\pi\}$, $\varphi_\star$, E and ϑ coincide. All three angles are degenerate for circular orbits. However, in circular orbits P is ill-defined. We illustrate these different anomalies in 5.1.

Some typical relations that we will use are *Kepler's equation*, relating E and ϑ:

$$\vartheta = E - e\sin E, \tag{5.1}$$

and the trigonometric relations between eccentric anomaly and true anomaly:

$$\cos\varphi_\star = \frac{\cos E - e}{1 - e\cos E}, \quad \cos E = \frac{\cos\varphi_\star + e}{1 + e\cos\varphi_\star}, \tag{5.2}$$

$$\tan\left(\frac{1}{2}\varphi_\star\right) = \left(\frac{1+e}{1-e}\right)^{1/2}\tan\left(\frac{1}{2}E\right). \tag{5.3}$$

We are also going to use several useful expansions in small eccentricity:

$$\varphi_\star = \vartheta + 2e\sin\vartheta + \frac{5}{4}e^2\sin(2\vartheta) + \mathcal{O}(e^3), \tag{5.4}$$

$$\varphi_\star = E + e\sin E + \frac{1}{4}e^2\sin(2E) + \mathcal{O}(e^3). \tag{5.5}$$

5.3 Resonant Transitions in Eccentric Orbits

Following Ch. 4, we again consider a boson cloud around a black hole of mass M in an orbit with a companion object of mass $M_\star$, where $q \equiv M_\star/M$ is the mass ratio. The coordinates are centered at the BH plus cloud system, where $R_\star$ denoting the radial distance to the perturber, and $\varphi_\star$ the azimuthal angle. Again, since we consider planar motion with spin parallel to the orbital angular momentum, this angle is identical with the true anomaly. The orbit is described by the semi-major axis a and the eccentricity e. We define the orbital frequency to be always positive such that the two orientations, co-rotating and counter-rotating, are identified by $\dot{\varphi}_\star = s|\dot{\varphi}_\star|$, with $s = \pm 1$. Again,

we are considering a two-level system with cloud states $|a\rangle$ and $|b\rangle$, and for a perturber outside the cloud ($R_\star \gg r_\mathrm{c}$), we are using that the off-diagonal matrix elements of the Hamiltonian, $\langle a|\, V_\star\, |b\rangle$, can be written in the multipole expansion as an harmonic series [25, 26]

$$\langle a|\, V_\star\, |b\rangle_{l_\star} = \sum_{|m_\star|\leqslant l_\star} \eta_{ab}^{(m_\star)} \mathrm{e}^{-im_\star\varphi_\star}\,, \tag{5.6}$$

The selection rules explained in Ch. 4 determine, which $l_\star$ terms are non-zero and force $m_\star = \Delta m$. Including a non-zero decay rate Γ_b of the second state, the Schrödinger equation is given by[II]

$$i\begin{pmatrix}\dot{c}_a\\ \dot{c}_b\end{pmatrix} = \begin{pmatrix} -\frac{\Delta\epsilon}{2} & \eta_0\left(\frac{R_\star}{R_0}\right)^{-(l_\star+1)}\mathrm{e}^{i\Delta m\varphi_\star}\\ \text{c.c.} & \frac{\Delta\epsilon}{2} - i\Gamma_b\end{pmatrix}\begin{pmatrix}c_a\\ c_b\end{pmatrix}\,, \tag{5.7}$$

We are going to analytically understand the effect of introducing eccentric orbits in the small-eccentricity expansion. It is expected that GW emission reduced the initial eccentricity before the resonant transition is encountered. This approximation will turn out to be rather accurate upon comparison with numerical solutions for generic equatorial orbits in most part of the parameter space.

In the small-eccentricity expansion, the true anomaly can be approximated by the mean anomaly as:

$$\varphi_\star = \vartheta + 2e\sin\vartheta + \mathcal{O}(e^2)\,, \tag{5.8}$$

$$R_\star = a(1 - e\cos\vartheta) + \mathcal{O}(e^2)\,. \tag{5.9}$$

Here, we used the relation $R_\star \simeq a(1-e\cos E)$ as well as the Kepler equation $E - e\sin E = \vartheta$. We remind of the relations $\dot{\vartheta} \equiv s\Omega$ and $\Omega = \sqrt{M(1+q)/a^3}$. This expansion gives rise to sinusoidal function inside the exponential factor of Eq. (5.6). We can use the Jacobi-Anger expansion into Bessel functions to rewrite that exponential factor up to linear order in eccentricity:

$$\mathrm{e}^{\pm i\Delta m(\vartheta+2e\sin(\vartheta))} = \sum_{k=-\infty}^{\infty} (\pm 1)^k J_k(2e\Delta m)\mathrm{e}^{i(k\pm\Delta m)\vartheta}\,. \tag{5.10}$$

We note the notational difference between eccentricity e and Euler's number e. For small arguments, the Bessel function can be approximated by

$$J_k(2e\Delta m) = \frac{(-\mathrm{sgn}(k)\Delta m e)^{|k|}}{|k|!}\,, \quad e \ll 1. \tag{5.11}$$

[II] See Ref. [160] for a redefinition of the occupation densities that effectively absorbs a possible non-zero Γ_a into only one decay rate appearing as modified Γ_b.

In this small eccentricity-expansion, the Hamiltonian Eq. (5.7) can be written as

$$\mathcal{H} = \mathcal{D} + \sum_{k=-\infty}^{\infty} \begin{pmatrix} & \eta_k \mathrm{e}^{i(k+\Delta m)\vartheta} \\ \eta_k \mathrm{e}^{-i(k+\Delta m)\vartheta} & \end{pmatrix}, \tag{5.12}$$

$$\mathcal{D} = \begin{pmatrix} -\frac{\Delta\epsilon}{2} & \\ & \frac{\Delta\epsilon}{2} - i\Gamma_b \end{pmatrix}, \; \eta_k \sim \eta_0 \mathfrak{f}^{\frac{2}{3}(l_\star+1)} \frac{e^{|k|}}{|k|!}, \;\; \mathfrak{f} \equiv \frac{\Omega}{\Omega_0},$$

where we traded distance for orbital frequency. The full analytic form of the η_k is non-trivial, because if we want to absorb the expansion of $a(1-e\sin E)^{-(l_\star+1)}$ in terms of ϑ into the exponential factor for every k-term, which scale as $e^{|k|}$, for every order in e, we have to take more terms into account. Using the properties of the Bessel function for parity, $J_k(-x) = J_{-k}(x) = (-1)^k J_k(x)$, and the recurrence formula $x\left(J_{k+1}(x) + J_{k-1}(x)\right) = 2kJ_k(x)$, the tidal perturbation to linear order in e, and therefore valid for $|k| \leqslant 1$, can be written as

$$\begin{aligned} \eta^{(\star)}_{ab,k} &= \eta^{(\star)}_{ab,0} \mathfrak{f}^{\frac{2}{3}(l_\star+1)} \tfrac{(\Delta m e)^{|k|}}{|k!|} \left(1 + \tfrac{(l_\star+1)k}{2\Delta m}\right) + \mathcal{O}(e^{|k|+1}), \\ \eta^{(\star)}_{ab,0} &= -\frac{q\alpha}{r_c}\left(\frac{r_c}{a_0}\right)^{l_\star+1} \frac{4\pi}{2l_\star+1} \left|Y^*_{(\star)}\left(\tfrac{\pi}{2}, \vartheta\right)\right| I_r I_\Omega, \end{aligned} \tag{5.13}$$

where $a_0 = [M(1+q)/\Omega_0^2]^{1/3}$.

It is evident that due to the expansion, the off-diagonal term in Eq. (5.12) now contains an infinite sum of eccentricity-suppressed terms containing the exponential term $\mathrm{e}^{i(k+\Delta m)\vartheta}$. From the analysis for circular orbits in Ch. 4, we know that the off-diagonal term leads to resonance, when the time derivative of the exponent in the exponential is equal to $\Delta\epsilon$. Since we expressed this in terms of ϑ, and $\dot{\vartheta} = \Omega$, we find a new, k-dependent resonance condition, which effectively introduces an infinite series of overtones

$$\Omega_k = \mathfrak{f}_k \, \Omega_0, \quad \mathfrak{f}_k = \frac{\Delta m}{\Delta m + k}, \quad k \in \mathbb{Z}, \tag{5.14}$$

where Ω_0 refers to the "main" transition which is also triggered on circular orbits

$$\Omega_0 = s\frac{\Delta\epsilon}{\Delta m} > 0. \tag{5.15}$$

When each of the k-resonances is sufficiently narrow, we can ignore the other ($k' \neq k$) terms in Eq. (5.12). First, terms with large $|k|$ will be strongly suppressed by eccentricity, since $\eta_k \sim e^{|k|}$. Second, these terms will oscillate and only have a negligible influence on the evolution of the states far from their respective resonance. A notable, and important, exemption from this assumption is the possible mixing with the spherical, strongly decaying states where $l = m = 0$. Their influence, captured as non-resonant, perturbative mixing, will be ignored for this part of the thesis and investigated in Ch. 7.

We can now linearize the orbital evolution near the respective transitions, $\Omega(t) = \Omega_k + f(e)\gamma_k t$,

where $f(e) = \frac{1+\frac{73e^2}{24}+\frac{37e^4}{96}}{(1-e^2)^{7/2}}$ and $\gamma_k \equiv \gamma_0 \mathfrak{f}_k^{11/3}$, with $\gamma_0 = \frac{96}{5} q M^{5/3} \frac{\Omega_0^{11/3}}{(1+q)^{1/3}}$ such that the Landau-Zener (LZ) solution now depends on the modified quantities

$$z_k \equiv \frac{\eta_k^2}{f(e)\gamma_k |\Delta m + k|} \quad \text{and} \quad v_k \equiv \frac{\Gamma_b}{\sqrt{f(e)\gamma_k |\Delta m + k|}} \,. \tag{5.16}$$

Ignoring the effects of backreaction, covered in the next section, the LZ solution is controlled by the parameters in Eq. (5.16), which controls the adiabaticity of the transition and the strength of the decay, respectively. As demonstrated in Ref. [150, 151], starting from the far past in the $|a\rangle$-state, in the limit $2\pi z_k \gg 1$, the eigenstate of the Hamiltonian yields a full population transfer to the (decaying) $|b\rangle$-state in the far future. We will demonstrate that although the solution changes for finite values of time, for different values of the parameter v_k, the asymptotic properties of the system (when we ignore backreaction) are robust with respect to variations in the decay width of the $|b\rangle$ state [161].

5.4 Orbital Backreaction

We already discussed the basics of orbital backreaction in Ch. 4. Like there, we focus on a two-state system. We are also assuming that the companion is outside of the cloud, because we focus on (hyper)fine resonances in two-level LZ transitions to a decaying mode.

For the equatorial case, the orbital dynamics can be governed by flux-balance equations at infinity [26, 28, 126, 153, 160, 162], and at the black hole's horizon [24, 109, 163]. We already mentioned in Ch. 4 that in the case of circular and equatorial orbits we only need one balance equation, while the results from balancing angular momentum and balancing energy lead to a different scaling with frequency. However, at the resonance, especially if it leads to a floating transition, this scaling does not change the phenomenology of the transition, because the frequency is mostly constant. For that reason the frequency appearing in the backreaction has often been set constant, i.e., $\Omega(t) \to \Omega_0$. For eccentric orbits, there is no redundancy and we need both angular momentum and orbital energy for the balancing approach. In Ch. 7 we will discuss in detail the caveats of this approach, and explain why we change to a different formalism in case of general, i.e., inclined, orbits. The balance equations for energy, angular momentum of orbit, cloud and BH are:

$$\dot{E}_{\rm o} + \dot{E}_{\rm c} + \dot{M} = \mathcal{F}_{\rm GW} \equiv -\frac{32 f(e)}{5} \frac{M^5 q^2 (q+1)}{a^5} \,, \tag{5.17}$$

$$\dot{L}_{\rm o} + s(\dot{L}_{\rm c} + \dot{S}) = \mathcal{T}_{\rm GW} \equiv \frac{\mathcal{F}_{\rm GW}}{\Omega} \frac{g(e)}{f(e)} \,, \tag{5.18}$$

$$\dot{M} = 2\Gamma_b E_{{\rm c}(b)} \quad , \quad \dot{S} = 2\Gamma_b L_{{\rm c}(b)} \,, \tag{5.19}$$

with $g(e) = \frac{1+\frac{7e^2}{8}}{(1-e^2)^2}$, and $\dot{M}$, $\dot{S}$ the change of mass and spin of the BH due to the decay of the $|b\rangle$ state into the black hole. We neglect effects due to changes in the background (M, S) black hole's parameters. We discuss phenomena that arise when we abandon this assumption in Ch. 8. The

right-hand side of the equations is given by the radiation reaction that carries energy and angular momentum to infinity by GWs.

The orbital energy and angular momentum are given by

$$E_{\rm o} = -\frac{M^2 q}{2a} \quad \text{and} \quad L_{\rm o}^2 = \frac{(M^5 q^3)(1-e^2)}{2(q+1)|E_{\rm o}|}\,, \tag{5.20}$$

while for the cloud they are a sum over the populated states, with $E_{{\rm c}(i)} \equiv (M_{{\rm c},0}/\mu)\epsilon_i |c_i|^2$, and similarly for $L_{{\rm c}(i)}$ with $\epsilon_i \to m_i$.

In the two-level system with a decaying mode, we can relate the total energy and the angular momentum of the $|a, b, {\rm BH}\rangle$ state (Eq. (5.17)-Eq. (5.19)) as

$$(\dot{L}_{\rm c} + \dot{S}) = (\dot{E}_{\rm c} + \dot{M})\frac{\Delta m}{\Delta \epsilon} \times \frac{\rho_\epsilon(t)}{\rho_m(t)} \tag{5.21}$$

$$\rho_x \equiv \frac{x_a}{\Delta x}\frac{d}{dt}|c_a|^2 - \Gamma_a |c_a|^2 - \sum \hat{\Gamma}_a |c_a|^2 + (a \to b)\,, \tag{5.22}$$

where $x \equiv \{\epsilon, m\}$, and the $\hat{\Gamma}$ represents other possible sources of dissipation, such as GW emission from the cloud [37, 88, 117, 120, 164, 165] or ionization [27, 152, 153]. The Schrödinger equation Eq. (5.7) yields

$$\rho_x = \frac{d}{dt}|c_a|^2 + 2|c_a|^2\Gamma_a + 2\frac{x_b}{\Delta x}\sum\left(\hat{\Gamma}_a |c_a|^2 + \hat{\Gamma}_b |c_b|^2\right)\,,$$

and a similar equation applies where $a \leftrightarrow b$. After superradiance has saturated the growth of the cloud in the $|a\rangle$ state, we have $\Gamma_a \simeq 0$. Moreover, for the floating timescales of the resonances we consider here, we can ignore other sources of dissipation during the LZ-transition, i.e., setting $\hat{\Gamma} \simeq 0$. Hence, $\rho_x = (d/dt)|c_a|^2$, which implies that $\rho_\epsilon/\rho_m = 1$. This yields the following expressions derived from Eq. (5.17)-Eq. (5.19) in terms of orbital frequency and eccentricity as:

$$\frac{d\Omega}{dt} = r\gamma_0 \mathfrak{f}^{11/3} f(e)\,, \tag{5.23}$$

$$\frac{de^2}{dt} = \frac{2}{3}\mathfrak{f}^{8/3}\frac{\gamma_0}{\Omega_0} f(e)\sqrt{1-e^2}\left[r\left(\mathfrak{f} - \sqrt{1-e^2}\right) - \mathfrak{f} + \frac{g(e)}{f(e)}\right]\,, \tag{5.24}$$

with

$$r \equiv \frac{\dot{E}_{\rm o}}{\mathcal{F}_{\rm GW}} = 1 - b\frac{{\rm sgn}(s\Delta m)\mathfrak{f}^{-11/6}}{\sqrt{f(e)\gamma_0|\Delta m + k|}}\frac{d|c_a|^2}{dt}\,. \tag{5.25}$$

Here we have defined the backreaction parameter b, which parametrizes the backreaction effects on the orbit due to the cloud:

$$b \equiv \frac{3M_{\rm c,0}}{M}\frac{|\Delta m|\mathfrak{f}^{-3/2}}{|\Delta m + k|^{-1/2}}\frac{(1+q)^{1/3}}{\alpha q}\frac{(M\Omega_0)^{1/3}\Omega_0}{\sqrt{\gamma_0}}\,. \tag{5.26}$$

While Eq. (5.23) and Eq. (5.24) may appear non-trivial at first sight, the introduction of r follows

a clear idea: As becomes clear from the form of Eq. (5.25), far from the transition, r will be unity, because $\frac{d|c_a|^2}{dt}$ will be zero. This renders the two balance equations to just describe the inspiral and circularization due to GW emission. From the form of Eq. (5.23), we understand that floating, i.e., $\frac{d\Omega}{dt} = 0$, corresponds to $r = 0$, which we will confirm analytically and numerically throughout the rest of this chapter. In the case of a sinking transition, we have $r > 1$, but in the following this case will not be relevant for us.

In the next subsections, we will analytically study the behavior of the non-linear LZ transition in the two limits of weak decay $v_k \ll z_k$ and strong decay $v_k \gg z_k$. For that we start from the solution to the linear LZ transition to a decaying state. We can then study the change of eccentricity during floating. In the end of the chapter, we will confirm the analytical estimates with numerical solutions, to then, in Ch. 6, apply the analytical estimates to a representative stellar mass BBH population.

5.5 Nonlinear Landau-Zener Transition

5.5.1 Linear Solution

The solution of the (linear) LZ transition, with adiabaticity parameter z_k and including a decaying width for the second state v_k, both normalised as above, Eq. (5.16), considering a linearized evolution of frequency, i.e., $\dot{\Omega}_k \simeq f(e)\gamma_k \simeq$ const and the resonance frequency being reached at $\tau = 0$, is given by [160, 161, 166]

$$\begin{aligned} |c_a|^2 &= \exp\left(-v_k\tau - \frac{\pi}{2}z_k\right)\left|D_{iz_k}\left(\mathrm{e}^{i\frac{3\pi}{4}}(\tau - iv_k)\right)\right|^2 \\ |c_b|^2 &= \exp\left(-v_k\tau - \frac{\pi}{2}z_k\right) z_k \left|D_{iz_k-1}\left(\mathrm{e}^{i\frac{3\pi}{4}}(\tau - iv_k)\right)\right|^2 , \end{aligned} \tag{5.27}$$

where D are parabolic cylinder functions [151], and we introduced a dimensionless time variable via

$$\tau \equiv t\sqrt{|\Delta m + k|f(e)\gamma_k}\,. \tag{5.28}$$

Note that the physical impact of γ_k, which is associated with the timescale of GW radiation, on the transitional dynamics is reflected via the ratio with the other two relevant parameters: $(\eta/\sqrt{\gamma_k})^2$ quantifies the adiabaticity of the transition, while $\Gamma_b/\sqrt{\gamma_k}$ measures the impact of the decay width relative to the dynamical time. It is remarkable, ignoring backreaction effects, that even though the solution is different from the solution to the non-decaying case, the transition probability at positive infinity, given by $|c_a(\infty)|^2 = \mathrm{e}^{-2\pi z_k}$, turns out to be independent of v_k. This fails to be the case for generic, nonlinear frequency evolution $\dot{\Omega}_k \sim t^n$ [166], which for our case is important during late inspiral.

However, the presence of a decay width tends to smooth out the LZ transition. A fraction of the initial state is transferred earlier than the case with $v_k = 0$. Additionally, the decay width dampens late-time oscillations. As a consequence, for large decay widths, the derviative $\frac{d}{d\tau}|c_a|^2$ peaks earlier than the non-decaying, $v_k = 0$, case. In the limit of strong decay, $v_k \gg z_k$, the LZ

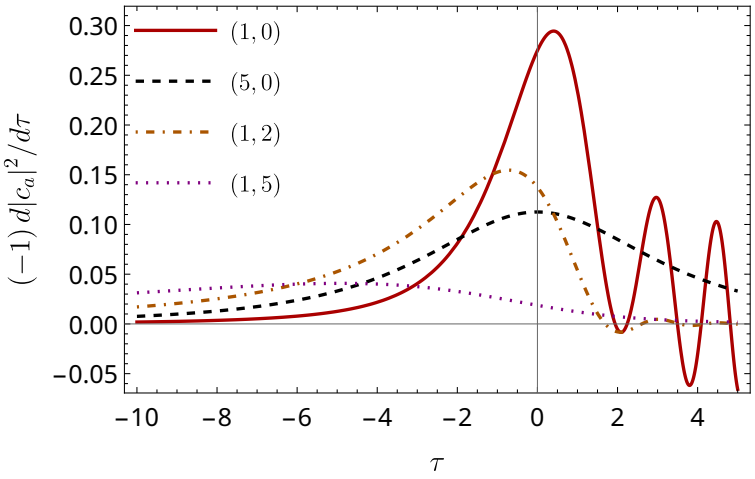

FIG. 5.2: We plot the (negative) derivative of the parent state occupancy, evaluated for a linear LZ-transition. The brackets in the legend correspond to (z_k, v_k). Note the decrease, as well as the shift to the left, of the amplitude, as well as the widening of the function and damping of the late-time oscillations, as the ratio v_k/z_k increases. Figure originally published in Ref. [1].

solution acquires a simple form [160, 166]

$$|c_a|^2 = \exp\left[-2z_k\left(\arctan\left(\frac{\tau}{v_k}\right)+\frac{\pi}{2}\right)\right], \tag{5.29}$$

$$|c_b|^2 = |c_a|^2\frac{z_k}{\tau^2+v_k^2}. \tag{5.30}$$

In this regime, $\frac{d}{d\tau}|c_a|^2$ peaks at $\tau_{\max}\simeq -z_k v_k$, and the width of the transition $\Delta\Omega$ roughly scales as

$$\frac{\Delta\Omega}{\sqrt{|\Delta m+k|f(e)\gamma}}\simeq 2v_k\sqrt{1+2z_k^2}. \tag{5.31}$$

5.5.2 Nonlinear Backreaction Effects

Because of the backreaction on the orbital frequency, the latter controlling the LZ transition itself, the problem becomes nonlinear. This means that the transition depends nonlinearly on the level-occupancy via the derivative of the initial state occupancy. This becomes obvious through the factor of r in Eq. (5.25). In Fig. 5.2, we plot this derivative for the linear LZ problem for different combinations of z_k and v_k.

Inspection of Eq. (5.24) shows that, in those regions of the parameter space where it has compact support, the effect of backreaction is to renormalize the parameters $(z_k, v_k)\to(\zeta_k, w_k)$ near the maximum value as

$$\zeta_k = \frac{\eta_k^2}{|\Delta m+k|\dot{\Omega}_k} = \frac{\eta_k^2}{|\Delta m+k|\gamma_k f(e) r} = \frac{z_k}{r_k(\zeta_k)}, \tag{5.32}$$

$$w_k \equiv \frac{v_k}{\sqrt{r_k}} \tag{5.33}$$

while the energy transfer itself depends on the level-occupancy of the cloud. That the effective adiabaticity parameter ζ_k becomes, in the nonlinear problem, a function of itself, shows, why a net-positive energy transfer from the cloud slows the inspiral down to floating, but not further. $r \to 0$ corresponds to $\zeta \to \infty$, which means the transition becomes as adiabatic as possible. Consequently, the system is "self-regulatory" in the sense that backreaction makes the transition infinitely adiabatic at best, but cannot lead to outspiral ($r < 0$).

While there is no full analytical solution to the nonlinear problem, we can find approximate solutions self-consistently in terms of the relevant parameters. Even in the regime where backreaction is strong, this mapping provides a useful indicator to evaluate whether, e.g., floating can occur, by indicating the breakdown of the linearization of the full problem. From the self-consistency condition above, Eq. (5.32), the "true" time scale for the nonlinear problem follows as $\mathrm{T} \equiv \sqrt{r_k}\tau$. We can then express the derivatives of the LZ function in terms of these quantities:

$$\frac{d|c_i|^2}{d\tau} = \sqrt{\frac{z_k}{\zeta_k}}\frac{d|c_i|^2}{d\mathrm{T}}\,. \tag{5.34}$$

We will map the non-linear problem into a quasi linear problem, by using the peak value of $\frac{d|c_a|^2}{d\tau}$, expressed in our "true" parameters, and plug this into the definition of the r, Eq. (5.25). In certain limits we can then find an explicit expression for $\zeta_k = \frac{z_k}{r_k(\zeta_k)}$ and solve that for ζ_k in terms of the parameters we know.

Using the solution for the LZ-transition to a decaying state Eq. (5.27) with the renomalized quantities at the peak of $\frac{d|c_a|^2}{d\tau}$, $-\zeta_k w_k$ this gives:

$$\begin{aligned} -\frac{d|c_a|^2}{d\tau}\Big|_{\tau=-\zeta_k w_k} &= \sqrt{\frac{z_k}{\zeta_k}}\psi_k(\zeta_k, w_k)\,, \\ \psi_k \equiv \frac{1}{2}\mathrm{e}^{-\frac{1}{2}(\pi\zeta_k)}\Bigg[2w_k \left|\mathcal{C}H_{i\zeta}\left(\frac{\mathcal{C}w_k\Delta w_k}{2}\right)\right|^2 - \\ \left(\mathcal{C}H_{1-i\zeta}\left(\frac{\mathcal{C}^*\Delta w_k^*}{2}\right)H_{i\zeta}\left(\frac{\mathcal{C}\Delta w_k}{2}\right) + \text{c.c.}\right)\Bigg]\,, \end{aligned} \tag{5.35}$$

where $\mathcal{C} = 1 + i$, $\Delta w_k = w_k(1 - i\zeta_k)$ and H is the Hermite function. We now take the small-eccentricity approximation, setting $f(e) \simeq 1$. This is justified by the fact that the eccentricity is typically small across the parameter space before the LZ transition for the cases we are interested in.

5.5.2.1 Negligible-Decay Regime

We now work in the small decay limit, where $v_k \ll z_k$ and hence $w_k \ll \zeta_k$. In this regime, the ψ_k function simplifies significantly and gives for both limits of renormalised adiabaticity:

$$\lim_{\zeta\to 0}\psi_k \sim \sqrt{\pi}\zeta\,, \quad \& \quad \lim_{\zeta\to\infty}\psi_k \sim \frac{1}{4\sqrt{\zeta}} \quad (w_k \ll \zeta_k)\,, \tag{5.36}$$

in which

$$\zeta_k \sim z_k \left(1 - \mathrm{sgn}(s\Delta m)\frac{b_k}{4\sqrt{z_k}}\right) , \tag{5.37}$$

and the value of r_k is given by the inverse of the bracket. For completeness, we explicitly state it below, in Eq. (5.43).

This result shows that the energy transfer for the adiabatic floating ($s\Delta m < 0$), is extremised by large backreaction, b_k and moderate values of z_k. In contrast, a sinking orbit, ($s\Delta m > 0$), can be consistent with large adiabaticity only for moderate backreaction parameters, $b_k < 4\sqrt{z_k}$.

Furthermore, we note that the large backreaction limit ($b_k \gg 1$) of the weakly-adiabatic regime is naturally only possible for sinking orbits, because for floating, the backreaction will always tend to make the transition more adiabatic. In the former case, the renormalized adiabaticity is given by:

$$\zeta_k \sim \mathrm{sgn}(s\Delta m)\left(\frac{z_k}{b_k^2\pi}\right)^{1/3} , \; r_k \sim \mathrm{sgn}(s\Delta m)(\pi b_k^2 z_k^2)^{1/3} . \tag{5.38}$$

In such scenarios, the strong backreaction in most cases then leads to non-adiabatic sinking transitions which potentially have significant impact on the orbit.

5.5.2.2 Strong-Decay Regime

The impact of the decay width generally depends on the dynamical timescale of the LZ transition, and should be compared with the adiabaticity. For our case, considering the additional overtones arising in eccentric orbits, even if $z_0 > v_0$ at the main resonance $\mathfrak{f}_0 = 1$, this hierarchy may be reversed for $\mathfrak{f}_k \neq 1$, because z_k scales as $e^{2|k|}$ and hence can be highly suppressed for non-zero k.

Similarly to the results for negligible decay, we can also obtain approximate relations in the limit of strong decay, described by Eq. (5.29), which yields

$$\psi_k \sim \frac{2\zeta_k \mathrm{e}^{-\zeta_k[\pi - 2\arctan(\zeta_k)]}}{w_k(\zeta_k^2+1)} , \tag{5.39}$$

$$r_k \sim 1 \pm 2b_k z_k \frac{\mathrm{e}^{-\zeta_k[\pi - 2\arctan(\zeta_k)]}}{v_k(\zeta_k^2+1)} . \tag{5.40}$$

This regime shares some qualitative behavior with the $w_k \ll \zeta_k$ regime, but here the gain/loss of adiabaticity and impact on the orbit is suppressed by the ratio b_k/v_k. For floating orbits, a large adiabaticity is consistent where we have

$$\zeta_k \simeq \frac{\sqrt{2}}{\mathrm{e}}\sqrt{\frac{b_k z_k}{v_k}} , \quad r_k = \frac{z_k}{\zeta_k} \to 0 , \quad (b_k \gg 1) . \tag{5.41}$$

In contrast to that, for sinking orbits, the strong backreaction requires a small population transfer, and we find

$$\zeta_k \simeq \frac{v_k}{2b_k}\,, \quad r_k \simeq \frac{2b_k z_k}{v_k} \gg 1\,. \quad (b_k \gg 1) \tag{5.42}$$

We point out that, maybe counter-intuitively, having a strong decay width does not only NOT necessarily imply that the cloud will be totally depleted, but instead that it suppresses r_k, and with that the ability of the system to float. This results in a smaller amount of the cloud being transferred to the decaying mode. See also Eq. (5.55) below.

We have analyzed for the several regimes, how, due to the effect of backreaction, the effective LZ parameters $\zeta_k(t)$ and $w_k(t)$ behave. With these estimates, we can infer the amount of the energy and momentum transfer near the resonance by self-consistently solving the condition $\zeta_k = z_k/r_k(\zeta_k)$.

For a moderate-to-large population transfer, i.e., ($\zeta_k \gtrsim 1$), we summarise the limiting results in the two regimes of strong and weak decay:

$$r_k \simeq \left(1 - \mathrm{sgn}(s\Delta m)\frac{b_k}{4\sqrt{z_k}}\right)^{-1}\,, \qquad (w_k \ll \zeta_k) \tag{5.43}$$

$$r_k \simeq 2\left(1 + \sqrt{1 - \mathrm{sgn}(s\Delta m)\frac{b_k}{z_k v_k}}\right)^{-1}\,, (w_k \gg \zeta_k)\,. \tag{5.44}$$

In summary, except for the trivial case, when $\zeta_k \ll 1$, due to the non-linearity of the problem, the transfer of energy and angular momentum from the cloud to the orbit does not simply reduce to a quest for adiabaticity of the LZ transition, and this not even for $w_k \ll \zeta_k$. For example, for extreme cases, with $z_k \gg 1$, we know that the (unperturbed) transition spreads over a long time scale, given by $\Delta t_{\rm LZ} \simeq 4\sqrt{z_k/\gamma_k}$ [167]. But this in turn actually reduces the orbital impact, as it follows from Eq. (5.43). It turns out that, in the scenario of large backreaction, the *sweet spot* for floating orbits occurs when $b_k \gg \sqrt{z_k}$. Due to the properties of the LZ solution, a strong decay width, $w_k \gg \zeta_k$, will not alter this picture. However, the impact on the orbital evolution, as well as the population transfer, becomes suppressed by $1/v_k$, as shown in Eq. (5.44).

For sinking transitions, the largest values of r_k are obtained for nonadiabatic transitions.

5.6 Eccentric Fixed Points

It is now clear, for which parameters we can expect adiabatic transitions and strong backreaction to the orbit for the nonlinear system. The next step is to investigate, how eccentricity changes during the resonance.

During the GW-dominated epochs, far from the resonances, we have $r \simeq 1$, and the leading order term in Eq. (5.24) vanishes, while the first contribution is at $\mathcal{O}(e^2)$. Similarly, for the $k = 0$ (main) resonance, the first term is $\propto\left(\frac{r}{2} - \frac{11}{3}\right)e^2$. This results in a damping of the eccentricity, unless the orbit gets a large kick ($r \gtrsim 7.3$).

When the influence of the cloud increases, the RHS of Eq. (5.24) asymptotes to $(\mathfrak{f}_k - 1)(r-1)$, modulo a positive prefactor. In this case, it enters at leading order. Additionally, the differences in the GW fluxes in Eq. (5.17) compared to Eq. (5.18) generate a distinction between the early ($k < 0$) and late ($k > 0$) resonances. For floating resonances we have $r \simeq 0$ and the eccentricity grows for the early resonances ($\mathfrak{f}_k < 1$), while it decays for the late ones ($\mathfrak{f}_k > 1$). We can understand this by noticing that during floating, i.e., when $\dot{E}_o \simeq 0$, we have $\dot{L}_o \propto \left(\frac{\Omega - \Omega_0}{\Omega\Omega_0} + \mathcal{O}(e^2)\right)$. We can then use $d(L_o^2) \propto - d(e^2)$, which shows that the eccentricity grows for $\Omega_k < \Omega_0$, and decays whenever $\Omega_k \geqslant \Omega_0$. This trend is reversed for the case of sinking resonances.

The above conclusions followed from assuming small eccentricity. It is instructive to look at the opposite limit of large eccentricuty, i.e., $e \to 1$. In this case, the RHS of Eq. (5.24) becomes $\propto \frac{r-1}{(1-e)^3}$. Since the sign of $\frac{de}{dt}$ is positive for $\Omega_k < \Omega_0$ for a floating orbit, but turns negative when the eccentricity approaches $e \simeq 1$, this implies the existence of a *fixed point*, a critical "attractor" $e_{\rm cr}$. Inspecting Eq. (5.24) and remembering that $r \to 0$ for floating, it becomes obvious that this fixed point is given by the condition $g(e_{\rm cr})/f(e_{cr}) = \mathfrak{f}_k$. For instance,

$$e_{\rm cr} = \{0.46, 0.35, 0.29\}, \quad \text{for} \quad |\Delta m| = \{1, 2, 3\}\,, \tag{5.45}$$

with $k = -1$.

5.6.1 Floating

If the energy transfer is sufficient to reach $r_k \lesssim 0.2$, the growth of the orbital frequency becomes sufficiently suppressed to allow floating. In that case, we can use that Eq. (5.23) goes to zero and eliminate the explicit dependence on the backreaction parameter from Eq. (5.24) and solve for e, which remains true as long as the floating condition is fulfilled. The growth of initial eccentricity, assumed to be small, is given, in units of the dynamical time introduced in Eq. (5.31), by

$$e(t) \simeq \sqrt{e_{\rm in}^2 + I_e \tau (1 - \mathfrak{f}_k)}\,, \qquad (\mathfrak{f}_k \neq 1) \tag{5.46}$$

$$e(t) \simeq e_{\rm in} \exp\left\{-\frac{11}{6} I_e \tau\right\}, \qquad (\mathfrak{f}_k = 1) \tag{5.47}$$

$$I_e \equiv \frac{2}{3}\frac{\sqrt{\gamma_0}}{\Omega_0}\frac{\mathfrak{f}_k^{5/6}}{|\Delta m + k|^{1/2}}\,.$$

The fixed points of eccentricity depend both on $|\Delta m|$ and $|k|$. For the first few values of $|k|$ they can be described by the polynomial fit $e_{\rm cr} = g_0 + g_1 k + g_2 k^2$, where $g_0 = \{0.3, 0.2, 0.16\}$, $g_1 = \{0.18, 0.16, 0.14\}$, $g_2 = \{2, 1.6, 1.3\} \times 10^{-2}$, all for $|\Delta m| = \{1, 2, 3\}$ in respective order.

To find the evolution of the eccentricity towards the fixed point, we change the time variable in the evolution equations Eq. (5.24), from t to $e^2(t)$, yielding

$$\int_{e_{\rm in}^2}^{e_{\rm fin}^2} \frac{d(e^2)}{\sqrt{1 - e^2}\left[\frac{g(e)}{f(e)} - \mathfrak{f}_k\right]} = I_e b_k \left(1 - |c_a(\infty)|^2\right)\,, \tag{5.48}$$

The result can then be approximated by

$$e_{\rm fin} \simeq e_{\rm cr}\sqrt{1-{\rm e}^{-{\rm C_k}}}\,, \tag{5.49}$$

where

$${\rm C}_k = c_{\Delta m,k}\left[I_e b_k\left(1-|c_a(\infty)|^2\right)+\frac{e_{\rm in}^2}{1-\mathfrak{f}_k}\right], \tag{5.50}$$

and $c_{\Delta m,-1}=\{2.37,2,1.37\}$ for $\Delta m=\{-1,-2,-3\}$.

It it also possible to estimate the duration of floating from the value of $e_{\rm fin}^2$ in Eq. (5.48) via

$$\begin{aligned}\Delta\tau_{\rm Fl} &= \frac{1}{I_e}\int_{e_{\rm in}^2}^{e_{\rm fin}^2} d(e^2)\frac{1}{\sqrt{f(e)}\sqrt{1-e^2}\left[\frac{g(e)}{f(e)}-\mathfrak{f}_k\right]}\,,\\ &\simeq \frac{{\rm C}_k}{\tilde{c}_{\Delta m,k}I_e}\,,\quad \frac{c_{\Delta m,k}}{\tilde{c}_{\Delta m,k}}=\frac{1}{\sqrt{f(e_{\rm cr})}}\,.\end{aligned} \tag{5.51}$$

A strong floating provides a distinct phase of the nonlinear LZ transition, during which most of the population transfer occurs. From Eq. (5.25) above, we find

$$\frac{d|c_a|^2}{d\tau}=\frac{r(\tau)-1}{b_k}\,, \tag{5.52}$$

which gives rise to the typical linear (in time) decay of the population during floating. An estimate for the population transfer is given by

$$|c_a(\infty)|^2 \simeq |c_a(\tau<\tau_{\rm Fl})|^2-(1-r_k)\frac{\Delta\tau_{\rm Fl}}{b_k}\,. \tag{5.53}$$

In the strong decay regime, $r(t)\to 0$ is a necessary condition at each point in time during the resonance, but not sufficient to guarantee a steady floating-type period. Additionally, enough of the cloud must be left to sustain a small $r(t)$. Following [160], it is possible to estimate the sufficient condition by considering the minimum amount of cloud to "jumpstart" a floating period. Applying the linear LZ solution Eq. (5.29) to Eq. (5.25), we find

$$|c_a|^2_{\rm min} \simeq \frac{v_k\sqrt{f(e_{\rm in})}}{2b_k z_k(e_{\rm in})}(1-r_k)\,. \tag{5.54}$$

Here we understand the left hand side as the minimal amount of cloud needed to start floating for any particular resonance. In turn, finding that the right-hand side is larger than unity, floating will not be able to start. We can use the same condition to estimate the amount of cloud that is left when floating stops. This is achieved by doing a *backward* matching into the linear LZ solution from the end of the floating time,

$$|c_a(\infty)|^2 \simeq \frac{v_k\sqrt{f(e_{\rm fin})}}{2b_k z_k(e_{\rm fin})}(1-r_k)\,. \tag{5.55}$$

This then becomes the relative amount of the cloud that survives *after* floating stops. A strong decay and small z_k could, in principle, interrupt the floating and leave a moderate amount of the cloud's initial state to survive after the resonance. This is consistent with the "resonance breaking" phenomena discussed in [154]. However, for a resonance at the overtones we have $z_k \sim e^{|2k|}$, which increases during floating. This means that when the eccentricity approaches the fixed point, for example at the $k = -1$ overtone, the value of z_k will increase by a factor $(e_{\rm cr}/e_{\rm in})^2 \simeq 10^2 - 10^3$, and therefore significantly extend the floating period. Compared to the naive estimate in Eq. (5.54), this will reduce the amount of cloud left after the resonance.

In general, the equations Eq. (5.48), Eq. (5.51) and Eq. (5.55) must be solved self-consistently to determine the end state of floating. As an estimate, we can apply Eq. (5.46) to Eq. (5.55), and assume $e_{\rm in} \ll 1$, and then have

$$\frac{\Delta\tau_{\rm Fl}}{b_k/\sqrt{f(e_{\rm cr})}} \simeq \left(\frac{x-1}{2x} + \sqrt{\frac{(x+1)^2}{4x^2} - \frac{\lambda}{x}}\right) , \qquad (5.56)$$
$$\lambda = \frac{v_k}{2b_k z_k(e_{\rm in})} , \quad x = \frac{I_e b_k (1-f_k)}{e_{\rm in}^2} .$$

Note that for the $k = -1$ overtone, the dependence on $e_{\rm in}$ drops out from the ratio λ/x. In this instance $\lambda \ll x$, and we find the longest periods of floating, $\Delta\tau_{\rm Fl} \simeq b_k/\sqrt{f(e_{\rm cr})}$, and largest depletion of the $|c_a(\infty)|^2 \lesssim r_k$. Depending on the resonances and the parameter space, this hierarchy may be also valid for higher overtones. In summary, for the case of floating orbits (with $s\Delta m < 0$), if the backreaction is sufficiently effective to enforce $r_k \simeq 0$ while the eccentricity approaches the critical point, we found a way to estimate the floating time $\Delta t_{\rm FL} \simeq b_k/\sqrt{\gamma_k}$, left-over population $|c_a(\infty)|^2 \lesssim r_k$, and also the growth of the eccentricity, until the resonant transition is over, by Eq. (5.49).

5.7 Numerical Validation

While we have used a small-eccentricity approximation to describe the initial stages of the cloud's evolution in Eq. (5.12), we have checked through numerical studies that the behavior we described above remains valid for generic equatorial orbits.

Our semi-analytic approach described in the sections above, relied in part on the assumptions that the BBHs have small initial eccentricity when they enter the transition region. By numerically solving the Schrödinger equation for arbitrary equatorial orbits, coupled with the energy-momentum balance equations (Eq. (5.7), Eq. (5.17)-Eq. (5.19)), we have validated our analytical results for a number of representative examples. These examples include a broad range of initial eccentricity, $10^{-2} \lesssim e_{\rm in} \lesssim 0.5$. For this purpose, we used the generic description of the orbital evolution, $R_\star = a(1 - e\cos E)$, as a function of the eccentric anomaly E. In *Mathematica*, we used the NDSolve routine [168], and monitored the violation of unitarity in the $\Gamma_b = 0$ regime, and the residual for $\Gamma_b \geqslant 0$, and also the occupation numbers of the states Eq. (5.27). For examples with

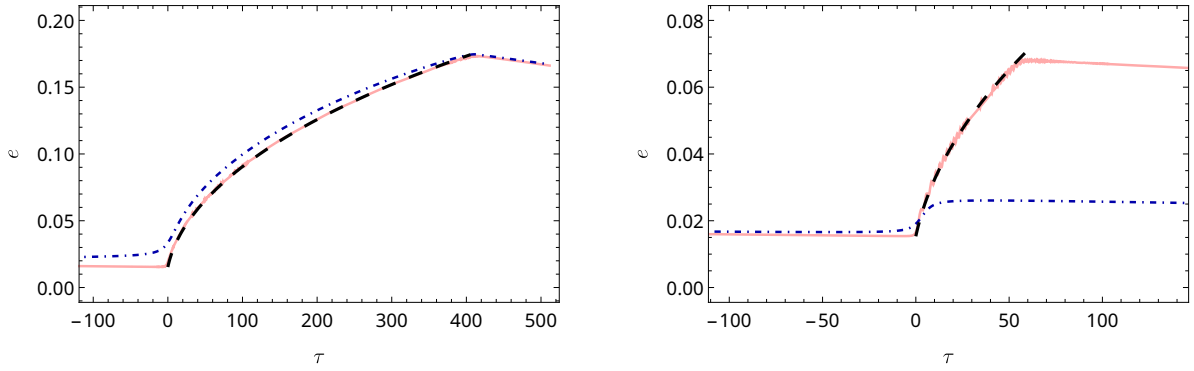

FIG. 5.3: The numerical evolution of the examples described in the text. The two figures correspond to the same z_k but different values for b_k, with the left plot having a stronger backreaction parameter (a few times larger) than on the right. The curves show the eccentricity evolution for vanishing (pink) and large decay width $v_k \gg z_k$ (blue, dot-dashed). Both choices for the backreaction yield floating orbits ($r_k \simeq 0$), except for the case of a large decay with small backreaction (blue curve on the right panel has $r_k \simeq 0.8$). The semi-analytic solution (black, dashed) (Eq. (5.24)) is in remarkable agreement within its regime of validity ($r_k \simeq 0$). Figure originally published in Ref. [1].

$(e, \Gamma_b) = 0$, we have also checked the consistency of our numerical results by comparing with the results in [83].

In general, we find that the numerical results are in broad agreement with the analytical arguments. As we have expected, the largest discrepancies occur for the estimates of $r(t)$ and $|c_a(\infty)|^2$. In the floating regime, the analytic results have a tendency to overestimate their respective values by a factor of few to an order of magnitude. This means our conclusions based on the analytic approximations can be considered conservative. In Fig. 5.3 we show (left) the numerical eccentricity evolution of a two-level system with $\Delta m = 2$ for values $\{z_0 = 4, v_0 = 2, b_0 = 200, e_0 = 10^{-2}\}$, for the main resonance. For these parameters, we find $\{z_{-1} = 7 \cdot 10^{-3}, v_{-1} = 3.4, b_{-1} = 450, I_e = 2 \cdot 10^{-4}\}$ at the $k = -1$ overtone, which is in the strong-decay regime: $v_{-1}/z_{-1} = 512$. The numerical evaluation is started before the system encounters the first overtone, following also the case $v_{-1} = 0$. Far away from the resonance, the orbital evolution follows the standard GW evolution in vacuum closely. The approximations found in Sec. 5.5 then correctly predict the strong floating that occurs (in both setups) at the frequency given by Eq. (5.14). We point out that, with small deviations, both cases follow the prediction for the growth of eccentricity assuming $r_k \simeq 0$ in Eq. (5.48). It is also broadly consistent with our estimates that the left-over occupancy of the initial state is given by $|c_a(\infty)|^2 \simeq 10^{-4}$ and $|c_a(\infty)|^2 \simeq 10^{-3}$, with and without the decay, respectively. If we reduce the backreaction to $b_0 = 25$ (Fig. 5.3, on the right), the decaying case does not develop floating, as $r_k \simeq 0.8$. However, as expected, there will still be a small growth of eccentricity, while the transfer of population is slightly increased compared to the linear LZ transition. In contrast, the case with small decay still undergoes a strong floating, follows the predicted growth of the eccentricity, and also experiences a transfer of the parent state up to $|c_a(\infty)|^2 \simeq 5 \times 10^{-3}$.

Chapter 6 A Population Study

6.1 Overview

In this chapter, we will apply the results of Ch. 5 to a representative fictitious population of BBHs formed in isolation. This will, summarized very briefly, include "evolving" each single BBH from birth frequency through the inspiral, checking which of the possible transitions can happen with significant population transfer, using the estimates to infer leftover population and eccentricity growth and then continuing this procedure until the BBH reaches the middle of the LISA band, with or without cloud.

As it was argued in the literature [129–131], LISA can in principle distinguish between BBH formation channels via the distribution of masses and eccentricities observed. We show that the contrast between evolution in vacuum, with decaying eccentricity, and the large eccentricities that is produced during early overtone transitions of the cloud can lead to dramatic changes in the expected evolution of the system. In this chapter, as a proof of concept, we take the stellar-mass BBH population that was studied in Ref. [129], which has chirp masses of $\mathcal{M}_{\rm ch} \lesssim 10 M_\odot$, and which is expected to form exclusively in isolation. This means that the BH spins are aligned with the orbital angular momentum, such that the assumption of equatorial (uninclined), co-rotating motion may be implemented here without loss of generality.

Since α dictates the time scale at which the cloud will grow, it can only take certain values, thus linking BH mass and boson mass. Consequently, we consider clouds of ultralight bosons with masses between 10^{-13} and 10^{-11} eV. Superradiance may excite the $|322\rangle$ state which then, depending on the parent black hole's mass and birth orbital frequency, will experience a series of (hyper)fine transitions. For the BBH population and values of μ we consider, the largest impact on the orbital evolution happens for values of $\alpha \gtrsim 0.1$. This means that the effect from the earlier-formed, but shorter-lived, $|211\rangle$-state will be subdominant, because it will form fast and will already have decayed via GW emission, when the respective resonances are met.

Before showing the resulting distribution of eccentricities in this population, we are going to discuss in greater detail, which resonances can actually be encountered by the BBHs.

FIG. 6.1: We show orbital resonance frequencies of possible fine transitions for the $|322\rangle$-component of the cloud. The blue and red arrows represent vacuum and floating BBH evolution, respectively, while the grey arrows point to various decaying modes that ultimately deplete the cloud. The thinner the line the smaller the cloud gets. Figure originally published in Ref. [1].

6.2 Atomic Resonances

The cloud is most effectively built up in states with maximal azimuthal number $m_{\rm max} = n - 1$. The states with strictly positive $m > 0$ *can* grow if the spin of the BH is large enough. That means $|100\rangle$ never grows. States with m closer to zero have faster growth rates for the same n, and for fixed m, lower n modes grow faster. This means, for an extremal Kerr BH, the $|211\rangle$ state grows fastest, while also states like $|311\rangle$, $|322\rangle$ and in general all $|n\ n-1\ n-1\rangle$ grow, but much slower, so we ignore them as long as $|211\rangle$ dominates. When the cloud has saturated the BHs spin such that $|211\rangle$ stops growing, $|322\rangle$ becomes the most dominant growing state. At the same time, the $|211\rangle$ depletes not only via GW emission. When $|322\rangle$ depletes the BH spin further, the growth rate of $|211\rangle$ turns negative, and it feeds back into the BH. For most part of the parameter space, however, the GW emission dominates.

Regarding phenomenological aspects, we are only interested in fine and hyperfine transitions. The strongest growing states can only experience (hyper)fine resonances transitioning to states with lower m. Such transitions are only possible on co-rotating orbits, where they obey $s\Delta m < 0$, leading to a floating-type motion.

From the selection rules for the tidal interactions, we find that the $|211\rangle$ state has only a single hyperfine transition that is possible on equatorial orbits, the one to $|21-1\rangle$, while the only possible fine transition, to $|200\rangle$, can only occur inside the cloud, because it is mediated only by the dipole.

Furthermore, we find that for small values of α, the duration of floating of the hyperfine transition would take longer than a Hubble time, obviously preventing the BBHs to reach the LISA band. We also consider that unless we find a precise fine tuning of the birth frequency of the BBH and cloud system, for large values of α we expect that the $|211\rangle$ component of the cloud will have decayed through its own GW emission before it can reach the resonant transition (see also Refs. [160, 169]).

The $|322\rangle$-state, for moderate values of α has reasonable growth time and is long lived regarding GW emission, so it is a viable candidate to be found on the BBHs of interest. $|211\rangle$ may experience various types of resonances. In contrast to the early and late resonances, like $|k| \neq 0$, all $k = 0$ hyperfine transitions to $|32m\rangle$ occur at the same frequency, because Δm drops out of the ratio. However, the dominant main hyperfine transition is the one to $|320\rangle$, because it is mediated by $l_\star = 2$. In contrast, the $|322\rangle \to |32-2\rangle$ resonance can only be mediated by the hexadecapole, i.e., $l_\star = 4$, making it extremely weak and non-adiabatic. The transitions to the $|32 \pm 1\rangle$ states are not

possible for equatorial orbits, because they are mediated by $l_\star = 2$, but then $m_\star = \Delta m \neq 2$, so the corresponding spherical harmonic will render this interaction zero for vanishing inclination.

The fine resonances from the $|322\rangle$ state are to $|31-1\rangle$ and $|311\rangle$ states, mediated by the octopole ($l_\star = 3$) and to the $|300\rangle$ state via the quadrupole ($l_\star = 2$), in that order as the frequency increases. The $|300\rangle$ state will be the culprit of a phenomenon that we have not considered in Ref. [1]: Due to its very large decay width, it influences the state long before the resonance is met. In the next part, especially in Ch. 8, we will investigate for which part of the parameter space this omission still does not spoil the phenomenological results.

Fig. 6.1 shows a succession of possible transitions. Even at these low frequencies, there can be overlap with (sinking) high-$l_\star$ Bohr resonances, i.e., resonances to states with different n that are very early due to their large Δm. Because they do not significantly affect the dynamical evolution, we ignore these here.

6.3 Eccentric Fossils in LISA

To illustrate the distinct physical effects of meeting (early) resonances, and also following [128, 129], we consider a birth orbital frequency for the BBH system along with the cloud at $\Omega_{\rm ini}/\pi \simeq 10^{-4}\,\text{Hz}$. Even in cases where the birth orbital frequency of the binary system may be lower, stellar evolution [79] could lead to younger (secondary) BHs carrying the cloud. To discuss possible phenomenological prospects, we are using the peak GW frequency [170]

$$f_{\rm GW} \simeq \frac{\Omega}{\pi}\frac{(1+e)^{1.1954}}{(1-e^2)^{3/2}}\,, \tag{6.1}$$

because this is what GW observatories will detect. We are "evolving" the BBHs until we reach a peak frequency $f_{\rm GW} = 10^{-2}$ (and 1 Hz for comparison).

The procedure to track the evolution of these BBHs is the following: μ is fixed as constant of nature. Since the original population in [129] is given only in terms of chirp mass, and eccentricity for each BBH, while the range of q is $[0.1, 1]$, we are assigning these q randomly. Assuming that the cloud forms on the heavier black hole, this fixes α for every BBH. We then check that for the range of α we get, the cloud has already formed the $|322\rangle$ state and that this is long-lived enough to encounter the resonances. We then order, in frequency, all possible hyperfine and fine resonances with the corresponding overtones, up to $|k| = 5$. Then we calculate for these resonances if the resonance is reached with a significant adiabaticity.[I] For that, we use that the estimates for ζ_k and r_k developed in Ch. 5. If the impact on the cloud and the orbit seems to be significant, we calculate the eccentricity and leftover cloud after the transition. This is done until either $f_{\rm GW} = 10^{-2}\,\text{Hz}$ is reached, or until the cloud has been depleted down to 10^{-4} of its original value. Of course, between the transitions, the orbit is evolved according to Peter's equations [125, 126], reducing the

[I] We will see that positive k will almost play no role, because it is basically impossible for the cloud to survive the main resonance, to then be lost at a late overtone. The BBHs that experience that are the ones born *after* the main resonance.

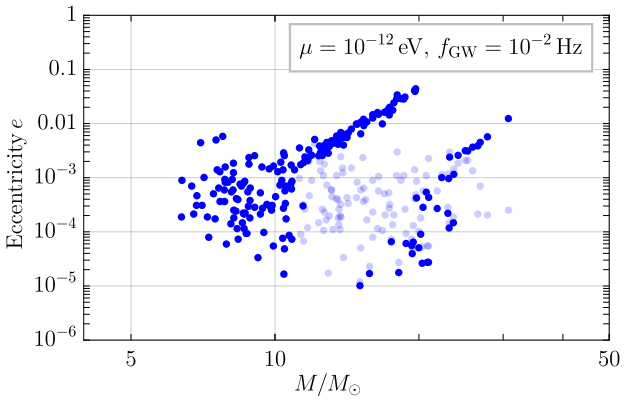

FIG. 6.2: BBH eccentricities at $f_{\mathrm{GW}} = 10^{-2}\,\mathrm{Hz}$, evolved with a uniformly distributed $q \in [0.1, 1]$, carrying a boson cloud on the heavier black hole. The pale blue dots show the values without a cloud [129]. BBHs with $e \lesssim 10^{-6}$ are not shown. Figure originally published in Ref. [1].

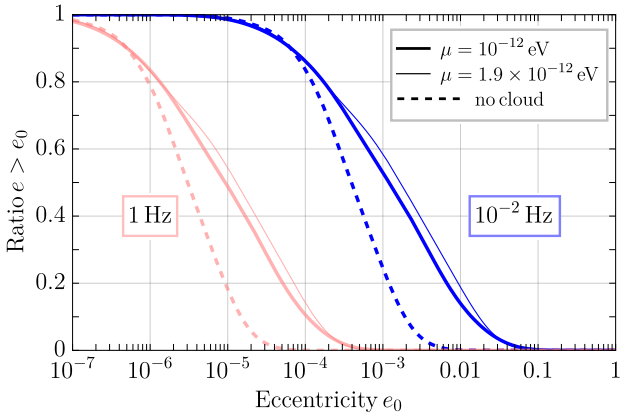

FIG. 6.3: The cumulative effect, i.e., the ratio of binaries with eccentricities above a given value e_0, with (solid) and without (dotted) a cloud, both at $10^{-2}\,\mathrm{Hz}$ (blue) and 1 Hz (pink), respectively. The thin line shows the result for a different boson mass. Figure originally published in Ref. [1].

eccentricity between the transitions. We also ensured that the whole inspiral as well as the floating transitions would complete within a Hubble time. The resulting distribution is shown in Fig. 6.2.

While some of the BBHs experience an early overtone of the hyperfine transition, the majority are affected by the fine overtones instead, because they are born after their respective hyperfine transitions. At these respective early resonances, the BBHs experience floating over a period of time while the orbit increases its eccentricity. The cloud typically either depletes at these overtones or decays later at the $k = 0$ resonance. Depending on the respective parameters, the ultimate decay may decrease the eccentricity or only have a small impact on the orbit. As a result, plotting all BBHs at the same frequency, a *wedge-like* distribution arises, where the heavier BHs (within each wedge) are subject to the largest increase in eccentricities, because they experienced the respective resonances the latest. We show the cumulative effect in Fig. 6.3. A significant fraction of the population is affected by the resonances, and yielding values of the eccentricities even at

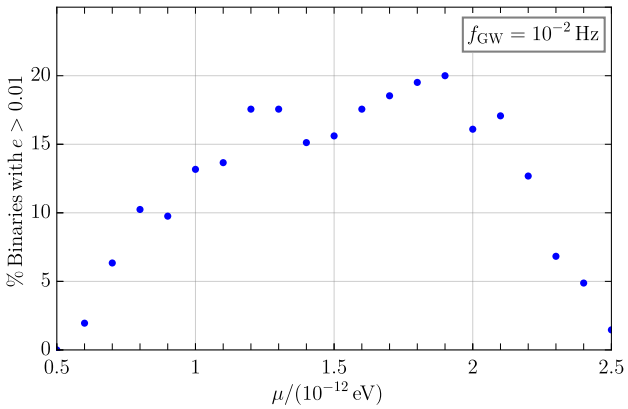

FIG. 6.4: Percentage of binaries from the population modeled after Ref. [129] that arrive with eccentricities above 0.01 at $f_{\rm GW} = 10^{-2}\,{\rm Hz}$ for different values of μ. Figure originally published in Ref. [1].

1Hz that may be within reach of mid-band and decihertz detectors. Increasing the value of μ shifts the location of the wedge in the distribution toward lower BH masses due to the relation with α. Vice versa, for decreasing the value of μ, the wedge shifts to larger mass BHs. Therefore, we can test which range of μ still influences the eccentricities of this particular population of BBHs. The dependence on the value of μ for the population reaching eccentricities with $e \gtrsim 10^{-2}$ at $f_{\rm GW} = 10^{-2}\,{\rm Hz}$, is shown in Fig. 6.4.

6.3.1 Overtone and Eccentricity Distribution

To assess the robustness of the prediction regarding early, eccentricity-enhancing overtones, we evaluate the distribution of resonances at early overtones, as well as the eccentricities in the population from Ref. [129]: For the BBHs that we evolved, resulting in Figures 6.2 and 6.3, only a few percent experience a floating transition $|322\rangle \to |31-1\rangle$ with a very early overtone fulfilling $k < -1$, while 25 % experience floating at the $k = -1$ resonance, making this the dominant one. Approximately 15 % of the population float at the main, $k = 0$, transition. Only a few BBHs experience resonances to either $|311\rangle$ or $|300\rangle$ states. The BHs with the largest masses, hence also the largest values of α for fixed μ, can float at the $|322\rangle \to |320\rangle$ hyperfine transition, where of the order of 5 % each either see an early resonance and increase eccentricity there, or they experience the main or $k = 1$ resonance and decrease eccentricity instead. We do not find any significant impact for overtones with $|k| > 4$. This also justifies why we did not even include $|k| > 5$, because they are extremely suppressed. In the left panel of Fig. 6.5, we show the distribution of the different k's that are experienced by the BBHs from the population with significant adiabaticity population. We show, in the right panel, the distribution of initial eccentricities the BBHs have before the floating starts. We note that, as an internal consistency check, that for most of the resonances the initial eccentricity fulfills $e_{\rm in} \lesssim 0.1$, which gives further support to assume the validity of the small-eccentricity approximation we developed. In Fig. 6.6, we plot the evolution of eccentricity as a function of peak frequency for three representative cases drawn from the population in Figures 6.2 and 6.3.

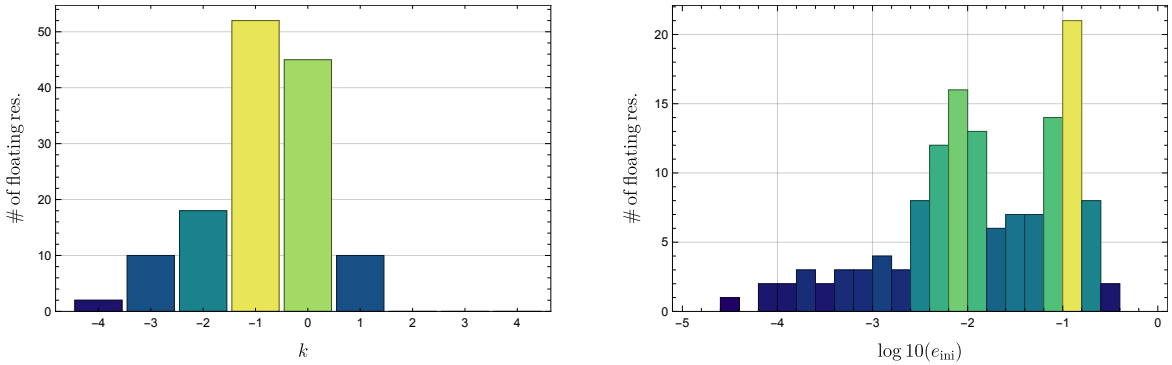

FIG. 6.5: The number of floating resonances for specific k (*left*) and binned by initial eccentricity (*right*) for the floating orbits the population shown in Figures 6.2 and 6.3 experiences. Figure originally published in Ref. [1].

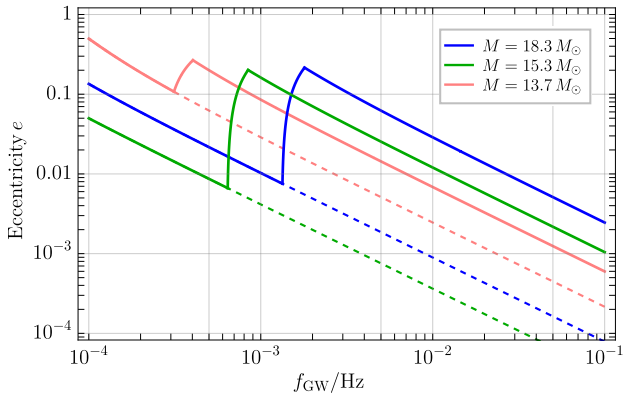

FIG. 6.6: Eccentricity evolution (in terms of the GW peak-frequency) for representative examples from Figures 6.2 and 6.3. Solid lines show the evolution with the cloud, while dashed lines represents the standard vacuum evolution. Note that during floating, the peak-frequency still grows due to the growth of eccentricity. Figure originally published in Ref. [1].

In the final plot of this section, Fig. 6.7, we show two exemplary plots about the parameters spaces of floating. For the specific transition $|322\rangle \to |31-1\rangle$ at the early overtone $k = -1$, we show a plot of the final eccentricity that can be reached depending on α and q, and for the same parameters the actual floating time, which of course scales with the actual BH mass M.

6.3.2 Different Birth Frequency

Similar to Figures 6.2 and 6.3, Fig. 6.8 shows the eccentricity distribution of the same population after experiencing the resonances at a final frequency of $f_{\rm GW} = 10^{-2}\,\text{Hz}$, but here we assumed a lower birth frequency for the BBH and cloud system, namely at $\Omega_{\rm ini}/\pi = 5 \times 10^{-5}\,\text{Hz}$. The main difference to Figures 6.2 and 6.3 is that more BHs can experience the hyperfine resonance. Of the ones that experienced the fine resonance before, this effects the highest mass BHs. Therefore, it cuts off some high eccentricity remnants, because these BBHs experienced the fine resonance at relatively high frequency. This means that the number of larger-than-expected eccentricity points

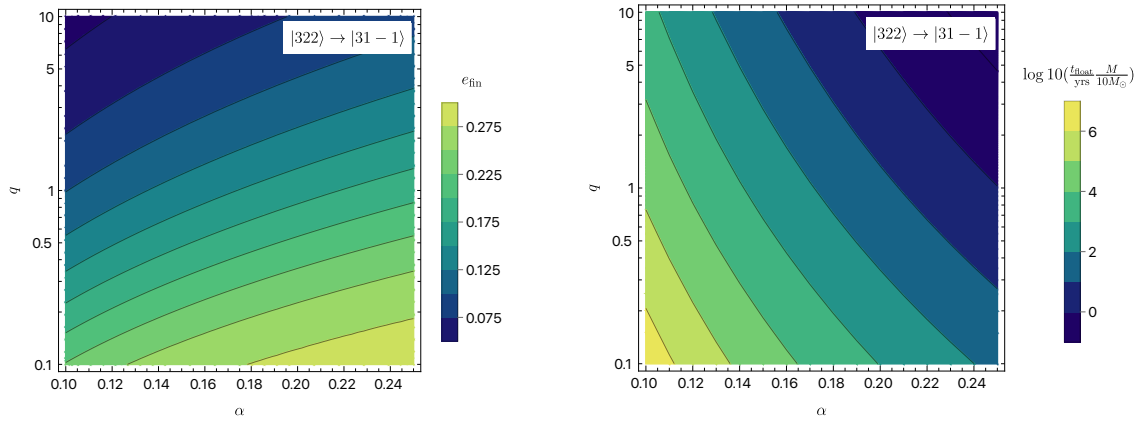

FIG. 6.7: Final eccentricity (*left*) and floating time (*right*), for the $|322\rangle \to |31-1\rangle$ transition with $k = -1$, assuming initial conditions that lead to a (long-lasting) floating orbit ($r_{-1} \simeq 0$) and $e_{\rm in} \ll 1$. Figure originally published in Ref. [1].

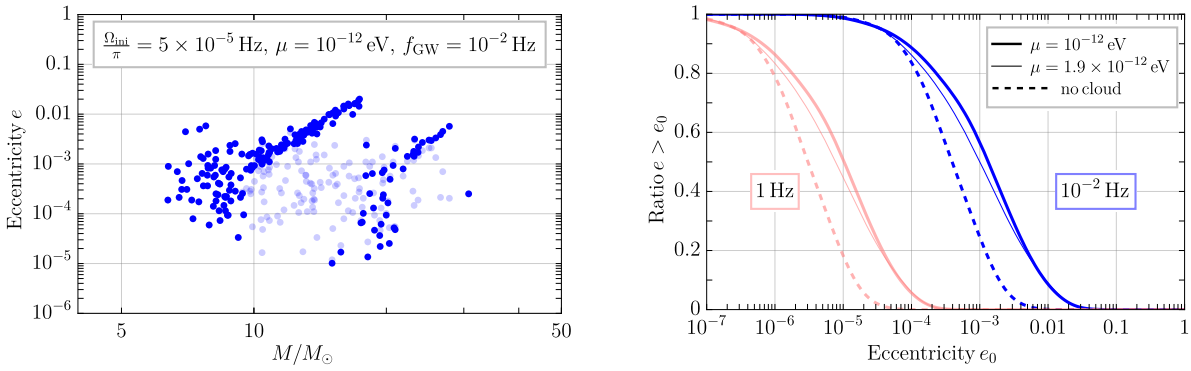

FIG. 6.8: Same as Figures 6.2 and 6.3, but with $\Omega_{\rm ini}/\pi = 5\times10^{-5}\,{\rm Hz}$ as the birth orbital frequency for the BBH and cloud system. Figure originally published in Ref. [1].

in the final plot is somewhat reduced, but still Fig. 6.8 illustrates the robustness of our predictions against changes in the initial conditions. We did this comparison, because a large fraction of BBHs that merge within a Hubble time will be born with orbital frequencies between $[0.5, 1]\times10^{-4}$Hz [128]. We also note that BBHs that are formed through a common-envelope mechanism can bring the binary initially closer, e.g., see Ref. [79], and at the same time this may produce a younger secondary black hole that would ultimately carry the cloud, which would push the birth frequency of the BBH and cloud system towards higher values, hence avoiding altogether early and main hyperfine transitions that can increase the eccentricity very early, or decrease it, and both leading to the loss of the cloud. In summary, our findings in this part of the thesis demonstrate that a skewed distribution and larger-than-expected eccentricities in a population could be a strong signal of the presence of boson clouds in the BBH dynamics. We will introduce a new formalism to treat inclined orbits in the next chapter, and discuss a more holistic picture of the history of the superradiant cloud, including non-resonant mixing with strongly decaying states in Ch. 8.

Part III

Toward a Consistent Treatment of Superradiance in General Black Hole Binaries

Chapter 7 Hamiltonian Formalism for General Orbits

7.1 Overview

The majority of the pre-existing literature on superradiance in BBHs has dealt with narrow resonances solely on equatorial and circular orbits, while Refs. [1, 154, 171] were the first to include eccentricity. At the same time, inclined orbits have been investigated in Refs. [153, 154, 171]. While the treatment of eccentricity seems quite straight-forward, the problem of the intertwined evolution of the superradiant cloud, the central BH and the companion gets significantly more involved when the spin of the cloud and the binary companion are misaligned. Independent of the restrictions to the form of the orbit, the approach that was used to find the evolution of the cloud and binary system was to sum the energies of the orbit, cloud and BH, and also the respective angular momenta, and assume that their sum is conserved, respectively, modulo dissipative effects like radiation reaction (RR) or GW emission of the cloud. Without considering RR, phenomena like floating would be impossible. Effectively, this is a balancing procedure of energy and angular momentum flux at infinity, because with the exception of GW emission, no energy and angular momentum can leave the system, which is why we referred to them as balance equations. We will discuss in this chapter why this approach, as it was used, is flawed, and precisely why it gave rise to erroneous results. For equatorial orbits, the resulting dynamics are rather similar, and, especially for narrow resonances and during floating indistinguishable. However, even for equatorial orbits, the difference far from the resonance is significant. It has recently been shown that the strong decay rates of spherical states with $l = 0$ can deplete the cloud even far away from the resonance, or inhibit the superradiance process completely, which is why it was referred to as termination of superradiance by Refs. [155, 172]. While this effect is significant for a large part of the parameter space, it would still be overestimated with the balance equations approach. We elaborate on this in Ch. 8. Since the balance approach has also been used to derive the dynamical equations for inclined orbits, the resulting equations are erroneous. However, given that the floating time is finite, these errors affect the phenomenological consequences only in certain regions of the parameter space.

We provide a self-contained account of the types and the dynamics of mixing, that both unifies and complements the previous discussion [1, 26, 154, 155, 160, 173, 174], but also corrects it in many aspects. Balance equations did not lead to inconsistent results because the idea of balancing the individual energies and angular momenta with the radiation reaction is wrong *per se*, but because the assumptions of how the energy and angular momentum of the cloud is defined and in what way the orbit and the cloud spin are allowed to change were erroneous. We will show that the former assumption ignored the energy and angular momentum related to the mixing between different cloud states, but instead assumed these are just the sum of their individual components, which is why we will call this approach the *isolated atom approach* (IAA). Additionally, the treatment of fully general orbits was also incomplete in the literature due to the neglect of two orbital parameters which necessarily are additional degrees of freedom.

The method we will use is based on a different formalism than balancing fluxes: Lagrange's planetary equations, derived directly from Hamilton's equation give a full set of dynamical equations for all six orbital parameters depending on partial derivatives of the Hamiltonian. In this formalism, everything we need in the end is the cloud's Hamiltonian, from which the dynamics for both cloud and orbit can be derived. The multipoles of the cloud constitute a Hamiltonian interaction for the companion, adding to the Kepler Hamiltonian and giving rise to a non-Keplerian flow of orbital elements. In Ref. [154] the only degree of freedom added to a and e was the inclination. In the Hamiltonian method it becomes clear that inclination and angle of the ascending node are intertwined, and not allowing one of them to change renders the treatment of the other inconsistent. We can apply this framework best if we work in a setup where we take two different viewpoints: The perturber in the early inspiral sees the gravitational atom (GA) from far away, and is not concerned about the detailed physics of the superradiant cloud. In the worldline effective field theory (WEFT) of the perturber, the gravitational atom is just a mass providing the potential for the bound orbit, and an infinite sum of multipole moments to which it reacts by non-Keplerian evolution of the orbital elements. The other viewpoint is the gravitational atom which consists of the cloud that reacts to a perturbing potential from the companion. The basic principle of action-reaction dictates that the multipole moments the companion provides for the cloud and vice versa are mirror images of one another. However, given that the reaction to these potentials becomes non-trivial in the most general cases, we are going to treat it carefully and step-by-step:

- In Sec. 7.2 we introduce the worldline action for the companion, and use Hamiltonian mechanics to find the evolution of its orbital elements under the influence of a perturbing Hamiltonian. We then use the worldline action to find the relation between such a perturbing Hamiltonian and the multipole moments in the worldline action.

- In Sec. 7.3 we calculate the multipoles from the microphysics of the gravitational atom and find the corresponding Hamiltonian. We then find the evolution equations for a, e and ι.

- In Sec. 7.4 we will compare the Hamiltonian formalism to the balance equation's approach in the IAA in detail.

We leave the dynamics resulting from the full set of equations for Ch. 8.

7.2 Framework: WEFT and Lagrange's Planetary Equations

7.2.1 Worldline Action

We start by discussing some basic features of a systematic framework that we introduce to describe the orbital dynamics of gravitational atoms in BBHs. For the BH plus cloud system that has an energy density that peaks around a few orders of magnitude away from the horizon, at $r_{\rm c} \simeq r_g/\alpha^2$ (with $\alpha < 1$) [24], we can implement a Worldline Effective Field Theory approach for the binary system during the inspiral regime, as it has been discussed in Ref. [25]. In the early stages of the inspiral, the separation between the gravitational atom and the companion fulfills $R_\star \gg r_c$, and that means we can treat the gravitational atom as a point-like object that is endowed with a series of multipole moments [175–181]. This means at leading (quadrupolar) order, it can be described by the worldline action,

$$S_{\rm WEFT} = -\int d\tau \left[\mathcal{M}(\tau) + \frac{1}{2}\omega_\mu^{ab} S_{ab}(\tau) v^\mu(\tau) + Q_L(\tau)\nabla_{L-2} E^{i_{\ell-1} i_\ell} + \cdots\right], \tag{7.1}$$

where $\mathcal{M}(\tau)$ is the total mass of the gravitational atom, v^μ the four-velocity, $S_{ab}(\tau)$ is the spin tensor, with ω_μ^{ab} being the spin connection, and ∇ is the covariant derivative. The gravitational field enters through $E_{lm} = E_{\mu\nu} e_l^\mu e_m^\nu$, which is the projection of the electric component of the Weyl tensor onto a local frame satisfying $g_{\mu\nu} e_\mu^l e_\nu^m = \eta_{lm}$. The coefficients $Q_L(\tau)$, carrying the multi-index $L = \{i_1 \cdots i_\ell\}$, describe the (time-dependent) mass-type multipole moment of the object (in the Fermi frame) and the dots include magnetic-type couplings, which will not be relevant here. See Refs. [175–181] for more details.

In principle, this description is only valid in the regime where the companion is *outside* of the cloud, at orbital separation much larger than the Bohr radius. However, as we will see, although the multipolar decomposition breaks down when the companion enters the cloud, we are still able to truncate the infinite sum to a handful of terms, including also a dipolar coupling, due to the selection rules.

7.2.2 Orbit and Spin Dynamics

We will consider the full dynamical problem in the non-relativistic regime, but also incorporating Post-Newtonian (PN) corrections such as radiation-reaction and spin effects. The former is obvious, because otherwise we would not have inspiral or floating resonances, among other things. The task then is to solve for the orbital dynamics of a point-like object with time-dependent mass, $\mathcal{M}(t)$, spin vector, $\boldsymbol{S}_{\rm GA}(t)$, and mass multipole moments, $Q_L(t)$, interacting with a perturber of mass $M_\star$. For simplicity we assume that the latter has negligible spin and internal structure. We move to the center-of-mass frame as inertial frame and choose a unit vector $\boldsymbol{n}$ as a fixed axis. As it is common in celestial mechanics, see e.g. [182] we work with six orbital parameters. There are three that describe the form of the orbit and the position of the companion *in* the orbital plane,

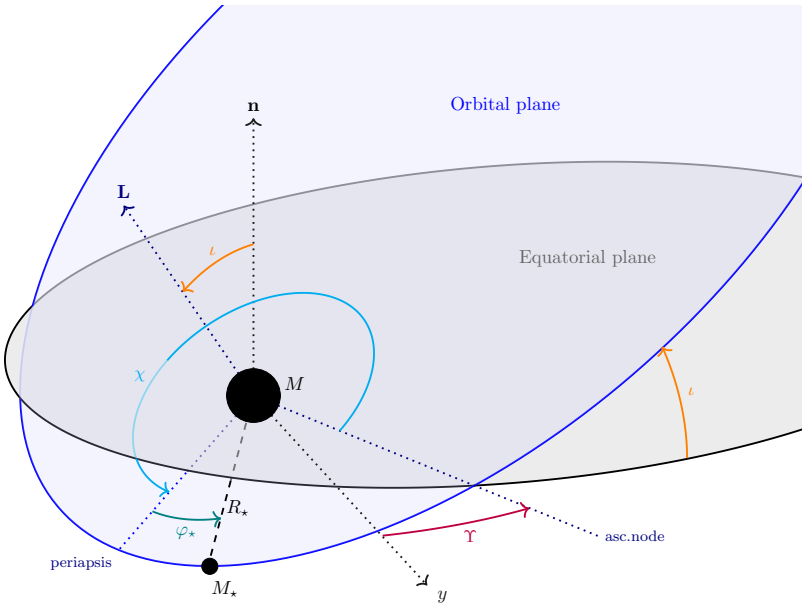

FIG. 7.1: Euler-angle rotation $\mathfrak{R}(\boldsymbol{n}, \hat{\boldsymbol{L}})$ from the reference frame, defined by the fixed axis $\boldsymbol{n}$, to the (non-inertial) *orbital* frame, whose z'-axis is aligned with the orbital angular momentum $\boldsymbol{L}$, while the y'-axis points toward the periapsis, with the positional elements of $\mathbb{E}$ indicated.

which are semi-major axis a, eccentricity e and one of the anomalies described in Sec. 5.2, which is measured from the periapsis. Then we need three more parameters to describe the position *of* the orbital plane with respect to the reference/equatorial plane. These are the longitude of the ascending node[I] (measured from some fixed axis, here the y-axis of the fixed coordinate system), called Υ, the inclination between the two planes, ι, and the argument (angle) of the periapsis as measured from the ascending node, χ. For a clearer picture see Fig. 7.1. The angular momentum vector of the orbit, $\boldsymbol{L}$ by definition is aligned with the z-axis of the orbital plane. The three orbital elements Υ, ι and χ refer to the three Euler angles of a passive coordinate transformation $\mathfrak{R}(\hat{n}, \hat{L})$ of the equatorial plane to the orbital frame.

A note to reference frame and coordinate conventions is in order. When performing transformations from the reference frame $\boldsymbol{n}$ to any other frame with the three (general) Euler angles $(\Upsilon_q, \iota_q, \chi_q)$, we use a passive zyz Euler rotation (in respective order):

$$\mathfrak{R}_q(\Upsilon_q, \iota_q, \chi_q) \equiv \begin{pmatrix} \cos\chi_q & \sin\chi_q & 0 \\ -\sin\chi_q & \cos\chi_q & 0 \\ 0 & 0 & 1 \end{pmatrix} \begin{pmatrix} \cos\iota_q & 0 & -\sin\iota_q \\ 0 & 1 & 0 \\ \sin\iota_q & 0 & \cos\iota_q \end{pmatrix} \begin{pmatrix} \cos\Upsilon_q & \sin\Upsilon_q & 0 \\ -\sin\Upsilon_q & \cos\Upsilon_q & 0 \\ 0 & 0 & 1 \end{pmatrix}, \quad (7.2)$$

This choice is common in quantum mechanics, because the small Wigner matrices d are purely

[I] The ascending node is the one of the two points of the orbit crossing the equatorial plane at which the companion crosses when the anomaly is growing.

real [183]. We note that in celestial mechanics the zxz convention is more common [182]. At the level of the orbital elements, the difference between the two choices reduces to $\chi|_{zyz} = \chi|_{zxz} + \pi/2$, $\Upsilon|_{zyz} = \Upsilon|_{zxz} - \pi/2$. However, in the zyz-convention, the periapsis in the orbital frame is aligned with the y-axis of that frame. From there, we measure the true anomaly. This would imply that a constant shift of $\pi/2$ should be included in Eq. (7.22). However, we suppress that, because it will have no phenomenological consequences.

To describe the position of the companion within the orbit, we choose the *mean anomaly*, ϑ, obeying $\dot{\vartheta} = \Omega$ for the Kepler problem, with $\Omega = \sqrt{\mathcal{M}(1+q)/a^3}$. Nonetheless, it will often be convenient to use the *eccentric* anomaly instead, especially for numerical reasons, see App. C. Also see Sec. 5.2 for details on the anomalies. We will refer to $\{a, e, \iota\}$ as *principal* and to $\{\vartheta, \chi, \Upsilon\}$ as *positional* elements. If we need to describe the spin degrees of freedom, we use the Euler angle rotation $\mathfrak{R}(\hat{n}, \hat{\boldsymbol{S}}_{\rm GA})$ with angles $(\Upsilon_S, \iota_S, \chi_S)$ to express the dynamics of $\boldsymbol{S}_{\rm GA}$ in the reference frame $\boldsymbol{n}$. In general, $\boldsymbol{S}_{\rm GA}$ will be the sum of the central BHs spin $\boldsymbol{S}_{\rm BH}$ and the spin of the cloud $\boldsymbol{S}_{\rm c}$. We expect them to stay aligned dynamically.

7.2.3 Lagrange's Planetary Equations

For a set of canonical variables $\boldsymbol{q}$ and their generalized momenta $\boldsymbol{p} \equiv \left(\frac{\partial \mathcal{L}}{\partial \dot{\boldsymbol{q}}}\right)$, we can write $\mathbb{D} \equiv (\boldsymbol{q}, \boldsymbol{p})$. For a given Hamiltonian H, Hamilton's equations are then given by

$$\frac{d\mathbb{D}}{dt} = \hat{\mathbb{J}} \frac{\partial H}{\partial \mathbb{D}}, \tag{7.3}$$

where $\hat{\mathbb{J}}$ is the symplectic matrix defined by

$$\hat{\mathbb{J}} \equiv \begin{bmatrix} 0 & \hat{\mathbb{I}}_n \\ -\hat{\mathbb{I}}_n & 0 \end{bmatrix}, \tag{7.4}$$

where $\hat{\mathbb{I}}$ is the unit matrix, and $n = 3$ is the number of pairs of (non)-canonical variables. A new set of variables $\mathbb{D}'$ is also canonical and fulfills Hamilton's equations if the Jacobian of the transformation $\mathbb{P} \equiv \partial \mathbb{D}'/\partial \mathbb{D}$ satisfies

$$\mathbb{P}^T \mathbb{J} \mathbb{P} = \mathbb{J}\,. \tag{7.5}$$

Spatial coordinates and their corresponding momenta are canonical variables, from which new ones can be found. If we use non-canonical variables, the respective derivatives between them have to be taken into account and will introduce additional dependencies on variables in the equation of motion.

For Keplerian orbits, the Hamiltonian is given by $H_{\rm K} = -qG\mathcal{M}^2/(2a)$ where $q = M_\star/\mathcal{M}$ is the mass ratio. We will show that the perturbation induced by the cloud as well as by PN effects can be written in the form of an additional term in the total Hamiltonian $H = H_{\rm K} + H_{\rm I}$. A typical set of canonical variables in celestial mechanics are the *Delaunay variables*, for which the

coordinate-momentum pairs[II] are given by [182]

$$\mathbb{D} = (\vartheta, \chi, \Upsilon, \Lambda, L, L_z)\,, \tag{7.7}$$
$$\Lambda \equiv [GM(1+q)a]^{1/2}\,, \tag{7.8}$$
$$L = [GM(1+q)a(1-e^2)]^{1/2}\,, \tag{7.9}$$
$$L_z = L\cos(\iota). \tag{7.10}$$

Λ is sometimes called the circular angular momentum, because it coincides with the angular momentum of a circularized orbit. Also these quantities are normalized to unit mass. However, we want to track the evolution of the state in terms of the variables introduced above that have a direct geometric interpretation. This constitutes a set of (non-canonical) orbital elements $\mathbb{E} \equiv \{\vartheta, \chi, \Upsilon\, a, e, \iota\}$. The flow of orbital elements $\mathbb{E}$ can be written in the form of Hamiltonian equations of planetary dynamics,

$$\frac{d\mathbb{E}}{dt} = \hat{\mathbb{M}}\frac{\partial}{\partial\mathbb{E}}(H_{\rm K} + H_{\rm I})\,. \tag{7.11}$$

The $\hat{\mathbb{M}}$ matrix takes into account the transformation between $\mathbb{E}$ and Delaunay's canonical basis:

$$\hat{\mathbb{M}} = \hat{\mathbb{G}}^{\rm T}\hat{\mathbb{J}}\hat{\mathbb{G}}\,, \quad \hat{\mathbb{G}} \equiv \frac{\partial\mathbb{E}}{\partial\mathbb{D}}\,, \tag{7.12}$$

where $\hat{\mathbb{G}}$ is the Jacobian for the $\mathbb{D} \to \mathbb{E}$ transformation. From that we find that the resulting orbital equations, called *Lagrange's (planetary) equations*, take the form

$$\frac{da}{dt} = -\frac{2\partial_\vartheta H_{\rm I}}{a\mu\Omega}\,, \tag{7.13}$$
$$\frac{de^2}{dt} = 2\sqrt{1-e^2}\frac{(\partial_\chi H_{\rm I} - \partial_\vartheta H_{\rm I})}{a^2\mu\Omega}\,, \tag{7.14}$$
$$\frac{d\iota}{dt} = \frac{\partial_\Upsilon H_{\rm I} - \partial_\chi H_{\rm I}\cos\iota}{a^2\sqrt{1-e^2}\mu\Omega\sin\iota}\,, \tag{7.15}$$
$$\frac{d\vartheta}{dt} = \Omega + \frac{2ae\partial_a H_{\rm I} + \left(1-e^2\right)\partial_e H_{\rm I}}{a^2 e\mu\Omega}\,, \tag{7.16}$$
$$\frac{d\chi}{dt} = -\frac{\left(1-e^2\right)\partial_e H_{\rm I} - e\partial_\iota H_{\rm I}\cot\iota}{a^2 e\sqrt{1-e^2}\mu\Omega}\,, \tag{7.17}$$
$$\frac{d\Upsilon}{dt} = -\frac{\partial_\iota H_{\rm I}}{a^2\sqrt{1-e^2}\mu\Omega\sin\iota}\,, \tag{7.18}$$

[II] Delaunay variables are also so-called *action-angle variables* [182]. There is an interesting aspect that can be studied with their help: We do not consider change of the orbit due to a mass loss of the whole gravitational atom, which happens during the transitions, but also steadily due to emission of GWs from the cloud itself. If we assume an adiabatic change of $M_{\rm c}(t)$, we can track the evolution of semi major-axis a due to the invariance of the action variable $\sqrt{(\mathcal{M}+M_\star)a}$:

$$\frac{da}{dt}\Big|_t = -a\frac{\dot{M}_{\rm c}}{M + M_\star + M_{\rm c}(t)}\,, \tag{7.6}$$

if this mass loss is strong enough and dominating over the radiation reaction. Ref. [169] studied how this could lead to outspiral for hyperfine transitions of $|211\rangle$.

with the reduced mass $\mu \equiv q\mathcal{M}/(1+q)$. The only term coming from $H_{\rm K}$ is $d\vartheta/dt = \Omega$, since $H_{\rm K}$ solely depends on a. In the next subsection, we will discuss how $H_{\rm I}$ is related to the multipole moments of the gravitational atom, and how the latter can be found for the superradiant cloud in Sec. 7.3. The plethora of effects stemming from the above equations are discussed in Sec. 8. If we want to consider spin dynamics of the gravitational atom, they would be also of the Hamiltonian form, taking place on the phase subspace $\mathbb{S}$,

$$\dot{\boldsymbol{S}}_{\rm GA} = \{\boldsymbol{S}_{\rm GA}, H_{\rm I}\}\,, \tag{7.19}$$

where $\{\}$ indicate Poisson brackets.

For any perturbation that can be written in terms of a Hamiltonian (see Ref. [184] for the Lagrangian formulation), the flow of the orbital elements is given by the above equations [182]. In the case of dissipative perturbations, one can express $\dot{\mathbb{E}}$ in terms of the perturbing force (Gauss equations) [182, 185]. As $\dot{\mathbb{E}}$ is linear in any non-Keplerian perturbation, the total change of $\dot{\mathbb{E}}$ will be the sum over all perturbations that act on the orbit. In the problem of a perturbed Keplerian orbit, we employ the osculating perspective - if the perturbation would be turned off at t, the orbit would be Keplerian (again) with the initial conditions given by the instantaneous values of the orbital elements $\mathbb{E}(t)$. However, it is important to note that while the perturbation is active, the orbits are not Keplerian and in general all the orbital elements will have a non-Keplerian flow, and this includes the mean anomaly $\dot{\vartheta} \neq \Omega$.

Finally, we note that the two angular elements χ and Υ are degenerate when $\iota \to 0$, and ill-defined when $e \to 0$. This can lead to numerical difficulties with Lagrange's equations when they get closer to this limit. In these cases one can use alternative sets of (non-)canonical elements that do not cause singularities [182] or work with the Keplerian-conserved quantities (see App. B).

We will be interested in tracking the dynamics of the system on *secular* timescales, meaning timescales that are much longer than the orbital period. This makes it possible to work within an *adiabatic approximation*, averaging over orbital timescales. In this way, we can also readily incorporate radiation-reaction effects, for example due to GW emission, see Eq. (7.24) and Eq. (7.25), but also BH absorption, by adding radiative terms to the right-hand-side of the above equations. However, for the terms in $H_{\rm I}$ that drive orbital resonances, we will not implement this averaging so that we can track the full resonant dynamics. Here we distinguish between three types of perturbations: conservative, mixing, and dissipative. The perturbations which are conservative do not change the orbital energy and angular momentum, and therefore can only influence the positional elements, see e.g., Ref. [185]. The mixing perturbations are those that exchange energy and angular momentum between the orbit and the gravitational atom, while dissipative processes emit energy-momentum to infinity. Although the mixing perturbations are intrinsically dissipative, the rearrangement of the degrees of freedom of the cloud during a resonant transition generally occurs on different timescales compared to the absorption of angular momentum and energy by the parent BH.

Tracking the orbital and spin degrees of freedom w.r.t. the fixed axis $\boldsymbol{n}$ is cumbersome in general. Owing to the fact that $\dot{\boldsymbol{L}}|_{\rm RR} \parallel \boldsymbol{L}$ to leading order in the radiation reaction (RR) [186],

there are three regimes where the description of the dynamics can be significantly simplified, on which we focus: (i) the equatorial setup where the spin $\boldsymbol{S}_{\rm GA}$ is (anti-)parallel to $\boldsymbol{L}$; (ii) The $q \simeq 1$ regime, where $|\boldsymbol{L}| \gg |\boldsymbol{S}_{\rm GA}|$; (iii) the extreme mass ratio (EMRI) limit, where $q \ll 1$ and $|\boldsymbol{S}_{\rm GA}| \gg |\boldsymbol{L}|$. Thus, we take $\boldsymbol{n} \approx \hat{\boldsymbol{L}}$ in (i) and (ii), and $\boldsymbol{n} \approx \hat{\boldsymbol{S}}_{\rm GA}$ in (iii). There are also instances when the total spin $\boldsymbol{J} = \boldsymbol{L} + \boldsymbol{S}_{\rm GA}$ can serve as a good reference vector (Sec. 7.3.2). We will elaborate on the applicability of these regimes in Sec. 8.3.

7.2.4 Interacting Hamiltonian

Introducing a companion at a relative distance $R_\star$, the mass-multipole couplings in the worldline action in Eq. (7.1) produce a Hamiltonian interaction

$$H_{\rm I} \supset -M_\star \sum_{l\geqslant 2} \frac{(-1)^l}{l!} Q^L e_L^A \partial_A \left(\frac{1}{R_\star}\right) , \tag{7.20}$$

with $R_\star \equiv \boldsymbol{R}_\star/\hat{R}_\star$ and where e_L^A maps from the orbital frame to the spin frame $\hat{S}$ parallel to $\boldsymbol{S}_{\rm GA}$ in which we perform the matching (see. 7.3). Contracting $e_L^A\partial_A$ and using the standard relations between the symmetric trace-free tensors and spherical harmonics we find

$$H_I \supset V_Q \equiv -M_\star \sum_{l\geqslant 2}\sum_{m=-l}^{l} \frac{4\pi}{2l+1}\frac{Y_{lm}(\hat{\boldsymbol{R}})}{R^{l+1}} Q_{lm} , \quad Q^{\langle L\rangle} = \frac{4\pi l!}{(2l+1)!!}\sum_{m=-l}^{m}\left(\mathcal{Y}_{lm}^{\langle L\rangle}\right)^* Q_{lm} , \tag{7.21}$$

where $\mathcal{Y}_{lm}^{\langle L\rangle}$ are symmetric trace-free (STF) tensor harmonics, and brackets around the multi-index denote the STF versions of the corresponding tensors. Q_{lm} are the spherical multipoles. Since Eq. (7.13)- Eq. (7.18) are written for the orbital elements that relate the orbital frame $\boldsymbol{L}$ to a fixed frame $\hat{\boldsymbol{n}}$, but the moments of the gravitational atom in its frame $\boldsymbol{S}_{\rm GA}$ are generally not fixed w.r.t to $\hat{\boldsymbol{n}}$, to relate the orbital dynamics $\hat{\boldsymbol{R}}$ in the GA-adapted frame with the orbital elements, we will perform a (passive) coordinate transformation in terms of Euler angles $\mathfrak{R}(\hat{\boldsymbol{S}},\hat{\boldsymbol{L}}) \equiv (\kappa,\beta,\xi)$ between the spin $\boldsymbol{S}$ and the orbital $\boldsymbol{L}$ frame. With these angles, the spherical harmonic relating the position of the companion to the quadrupole moments can be written as

$$\begin{aligned} Y_{lm}(\hat{\boldsymbol{R}}) &= \sum_{g=-l}^{l} [D^{(l)}_{mg}(\hat{\boldsymbol{S}},\hat{\boldsymbol{L}})]^* Y_{lg}\left(\frac{\pi}{2},\varphi\right) , \\ D^{(l)}_{mg} &\equiv \mathrm{e}^{ig\xi+im\kappa}[d^{(l)}_{mg}(\beta)]^* , \end{aligned} \tag{7.22}$$

where $D\,(d)$ are the Wigner (small) d-matrices [183], that encode the support of the multipoles: The $g=m$ term will have support around $\beta=0$, while $g=-m$ will have support around $\beta=\pi$. In order to apply the equations of motion Eq. (7.13)- Eq. (7.18), one needs to express (κ,β,ξ) in terms of dynamical variables $\mathfrak{R}(\hat{\boldsymbol{S}},\hat{\boldsymbol{L}}) = [\mathfrak{R}(\boldsymbol{n},\hat{\boldsymbol{S}})]^{-1}\mathfrak{R}(\boldsymbol{n},\hat{\boldsymbol{L}})$.[III]

[III] From $\mathfrak{R}_{SL} = \mathfrak{R}_S^{-1}\mathfrak{R}_L$ one can express SL angles via nS and nL. For illustration we report the most important one:

$$\beta = \arccos\left(\sin(\iota_L)\sin(\iota_S)\cos(\chi_L-\chi_S) + \cos(\iota_L)\cos(\iota_S)\right) . \tag{7.23}$$

As we have already done in Ch. 5, we are expanding the true anomaly as $\varphi = \vartheta + 2e\sin\vartheta + \mathcal{O}(e^2)$, and with the Jacobi-Anger identity we can express Y_{lg} in terms of ϑ as

$$Y_{lg}\left(\frac{\pi}{2},\varphi\right) = \sum_{k=-\infty}^{\infty} Y_{lg}\left(\frac{\pi}{2},0\right)\left[J_k(-2ge)+\mathcal{O}(e^{|k|+1})\right]\mathrm{e}^{i(g-k)\vartheta}\,,$$

where J_k is the Bessel function and $J_k \sim e^{|k|}$ as $e \to 0$. Effects coming from the spin dynamics will be shortly discussed in App. A. Other interacting terms that we will consider are point-particle and spin PN corrections up to 2.5PN order, where PN $\simeq (\Omega a)^2$. These effects are the point-particle 1PN and 2PN corrections, the spin-orbit (SO) coupling that enters at 1.5PN and the radiation reaction (RR) that enters at 2.5PN (e.g. [180]). The assumption of the point-particle nature of the companion will eliminate the spin-spin coupling that would enter at 2PN. The orbital flow due to the RR can be found via the Burke-Thorne potential, where the adiabatic averaging again gives Peter's evolution of the semi-major axis and eccentricity [125, 126]

$$\left.\frac{da}{dt}\right|_{\rm RR} = -\frac{64\mathcal{M}^3 q(q+1)}{5a^3}f(e)\,, \tag{7.24}$$

$$\left.\frac{de^2}{dt}\right|_{\rm RR} = \frac{64\mathcal{M}^3 q(1+q)}{a^4}\sqrt{1-e^2}\left(g(e)-f(e)\sqrt{1-e^2}\right)\,, \tag{7.25}$$

$$f(e) = \frac{1+\frac{73e^2}{24}+\frac{37e^4}{96}}{(1-e^2)^{7/2}}\,,\quad g(e) = \frac{1+\frac{7e^2}{8}}{(1-e^2)^2}\,.$$

When solving for the orbital parameters, we can add these to Eq. (7.13) and Eq. (7.14).

7.3 Matching

In this section, we will review the dynamical equations of the cloud in the tidal field of the companion and then describe the matching procedure that allows us to read off the coefficients of $Q_{lm}(t)$ from the short-distance physics of the gravitational atom.

7.3.1 Clouds in Isolation and in Tidal Fields

To describe the field Ψ evolving on a Kerr background, we align the z-axis of the reference frame $\boldsymbol{n}$ with the initial vector $\hat{\boldsymbol{S}}_{\rm GA}$, whose direction is (initially) inherited from the parent BH $\boldsymbol{S}_{\rm BH}$ and parallel to the initial spin of the cloud $\boldsymbol{S}_{\rm c}$, where $\boldsymbol{S}_{\rm GA} = \boldsymbol{S}_{\rm c} + \boldsymbol{S}_{\rm BH}$. This is a natural reference frame, since an equatorial orbit by definition is one where $\boldsymbol{L}$ and $\boldsymbol{S}_{\rm BH}$ are aligned. But we note again that in the full problem, $\boldsymbol{S}_{\rm GA}$ does not need need to stay aligned with $\boldsymbol{n}$, while the Lagrange equations Eq. (7.13)-Eq. (7.18) describe the change of orbital parameters w.r.t to $\boldsymbol{n}$.[IV] Again we will describe the system in the non-relativistic regime where $\alpha \ll 1$ and we can perform the field redefinition $\Psi = (\psi \mathrm{e}^{-i\mu t} + \text{c.c.})/\sqrt{2\mu}$, average over the (high-frequency) μ-terms, and expand the

[IV] As Boyer-Lindquist coordinates are adapted to an asymptotic observer, our reference frame is not rotating along with the BH or the cloud, thus we are slightly departing from the analysis in Ref. [181].

Klein-Gordon equation. In the frame of the (rotating) BH we get

$$i\dot{\psi} + \mathcal{I} = \left(-\frac{1}{2\mu}\nabla^2 - \frac{\alpha}{r} + V_{\rm R} + V_\star + V_{\rm sg}\right)\psi\,. \tag{7.26}$$

The potentials in this equation are $V_{\rm R}$, the (α-suppressed) relativistic corrections to the bound potential; $V_{\rm sg}$, accounting for the self-gravity of the cloud; and $V_\star$, induced by the presence of a companion. The remaining term on the left-hand-side, $\mathcal{I}$, includes all the non-Hermitian contributions due to decaying modes and absorption. Ignoring $\mathcal{I}, V_{\rm R}, V_\star$ and $V_{\rm SG}$, we again have the Schrödinger equation and the cloud is again described by the hydrogenic bound states, $|nlm\rangle \equiv \psi_{nlm}$ [32] with (fine and hyperfine) energy splitting [25, 83] as explained in Ch. 3.

If the companion is outside of the cloud ($R_\star > r_{\rm c}$), we again have [25, 26]

$$V_\star(r) = -\mu M_\star \sum_{l\geqslant 2}\sum_{m=-l}^{l} \frac{4\pi}{2l+1}\frac{r^l}{R^{l+1}} Y_{lm}(\hat{\boldsymbol{r}})Y^*_{lm}(\hat{\boldsymbol{R}}_\star)\,. \tag{7.27}$$

but now allow for general coordinates of $\hat{\boldsymbol{R}}_\star$. We discussed in Ch. 3, how this potential gives rise to Landau-Zener transitions between the states.

This time, for fully general orbits, we have to be more careful with the multipole expansion of the potential: As $Y_{lm}(\hat{\boldsymbol{R}}_\star)$ is evaluated in the $\hat{\boldsymbol{S}}_{\rm GA}$ frame, we use Eq. (7.22) to rewrite the overlap due to the multipole expansion and in the $e \ll 1$ limit (see also [1, 26, 154]). Additionally to the expansion into the l, m multipoles, and the sum over k for eccentric overtones, there is another sum arising, because for an inclined reference frame, a spherical harmonic becomes a sum of all spherical harmonics with the same l, i.e., ranging over all azimuthal quantum numbers: $-l \leqslant g \leqslant l$ related by the Wigner matrices:

$$\begin{aligned}
\langle a|\, V_\star\, |b\rangle_{lm} &= \sum_{g,k} \eta^{(ab|lm)}_{g,k} \mathrm{e}^{-i\Sigma_{g,k}}\,,\ \Sigma_{g,k} = (g-k)\vartheta + g\xi + m\kappa \\
\eta^{(ab|lm)}_{g,k} &\approx \eta^{(ab|lm)}_0 d^{(l)}_{mg}(\beta)\mathfrak{f}^{\frac{2}{3}(l+1)}\frac{(-\mathrm{sgn}[k]ge)^{|k|}}{|k|!}\left(1 + \tfrac{(l_\star+1)k}{2(-g)} + \mathcal{O}(e^2)\right)\frac{Y_{lg}\left(\frac{\pi}{2},0\right)}{Y_{lm}\left(\frac{\pi}{2},0\right)}\,, \quad \mathfrak{f} \equiv \frac{\Omega}{\Omega_0}\,, \\
\eta^{(ab|lm)}_0 &\equiv -\frac{\alpha_n M_\star}{GM_n^2}\left(\frac{GM_n}{a_0}\right)^{l+1}[\alpha_n\alpha(t)]^{-l}\frac{4\pi}{2l+1}Y_{lm}\left(\frac{\pi}{2},0\right)(I_r I_\Omega)^{(ab|lm)}\,, \qquad (7.28) \\
I_r^{(ab|lm)} &\equiv \int^{\mathsf{R}} d\mathsf{r}\mathsf{r}^2\hat{\mathcal{R}}_b\hat{\mathcal{R}}_a\mathsf{r}^l\,, \quad \int^{\mathsf{R}} \approx \int^{\infty} \\
I_\Omega^{(ab|lm)} &\equiv \int d\Omega_{\hat{r}} Y^*_a(\hat{r})Y(\hat{r})Y_b(\hat{r}), \qquad (7.29)
\end{aligned}$$

$\mathsf{r} \equiv r/r_{\rm c}$, $\mathsf{R} \equiv R/r_{\rm c}$, $\hat{\mathcal{R}}_c = r_{\rm c}^{3/2}\mathcal{R}_c$ is the (dimensionless) hydrogenic radial wavefunction, $\Delta x = x_b - x_a$ and $x = \{\epsilon, n, l, m\}$. We allow the BH mass to be time-dependent, so $\alpha(t)$ reflects that, while M_n, α_n denote the respective values when the $|a\rangle$ state is saturated,[V] while a_0 refers to the semi-major axis at the resonance. The sum over g is related to the equatorial case by the fact that

[V] See Sec. 8.3 for details on that notation.

for $\iota = 0$, $d^{(l)}_{mg}(0)$ is only non-zero if $g = m$, i.e., reducing the sum to the term with $m = -\Delta m$. For inclined orbits, other terms can be non-zero, and we will see that in general they can all be active at the same time.

Because the spherical harmonics are orthogonal, the bound states will receive self-corrections only from $m = 0$ terms. However, these are precisely the terms that don't have an explicit time dependence. There is, however, still an implicit dependence on time via principal orbital elements and $\alpha(t)$. For this framework to be applicable, we assume that this is adiabatic. Let us now *assume* we are in a region of the parameter space where the bound states receive only a perturbative correction by the mixing, such that the full solution has a following ansatz

$$\psi = \sum_a c_a(t)(\mathcal{R}_a Y_a + \delta\psi)e^{-i(\epsilon_a+\delta\epsilon_a)t}\,, \tag{7.30}$$

where $\mathcal{R}_a$ is the hydrogenic radial function, and $|\delta\psi| \ll |\mathcal{R}_a Y_a|$, $|\delta\epsilon_a| \ll \epsilon_a$. We can now use the standard toolkit of time-independent perturbation theory for linear systems to find estimates of the correction to the energy levels and the wavefunctions as

$$\delta\epsilon_a = \langle a|\, V_\star\, |a\rangle_{l0}\,, \quad \delta\psi_a = \sum_{b\neq a} \frac{\langle b|\, V_\star\, |a\rangle_{l0}}{\epsilon_a - \epsilon_b}\psi_a\,, \tag{7.31}$$

where $\epsilon_a > |\eta_{aa}|$ is a sufficient condition for the perturbative control, while we also must address the question if the perturbative expansion converges. If a certain two-state system approximately describes the time-dependent dynamics (going to be discussed below), one can in addition use $|\Delta\epsilon| > \max\left[|\eta_{aa}|, |\eta_{bb}|\right]$ as an indicator of convergence [187]. Physically, if perturbativity breaks down, this is telling us that the binding potential of the full problem is not dominated by the superradiant instability of a single BH, but instead is more similar to something that has been called a gravitational molecule [188][VI].

If the perturbative condition for the bound states is satisfied (see below), we can assume that the expansion Eq. (7.30) is approximately valid and then solve the time-dependent problem of level mixing, generated by the $m \neq 0$ terms in the multipole expansion, *non-perturbatively*.[VII] A perturbative approach for resonant transitions will necessarily generate divergences and loss of predictability, e.g., as in Ref. [157, 158]. We note here that the combination of the perturbative treatment of the bound states and the non-perturbative treatment of the occupancy dynamics is parallel to the treatment of superradiance in the presence of $\lambda\phi^4$ scalar interaction [89, 92]. Again, mixing can occur only if the selection rules are satisfied [25]: $m = -\Delta m$, $l + l_a + l_b = 2\mathbb{Z}$, $|l_a - l_b| \leqslant l \leqslant l_a + l_b$. In the new formalism, the full resonance condition determining where LZ-like level mixing is resonantly enhanced is given by

$$\dot{\Sigma}_{g,k} = -\Delta\epsilon\,. \tag{7.32}$$

[VI] In the late phase of the inspiral, even if one expands around a different background solution like the gravitational molecule, the adiabaticity assumption may break, which could hint at the necessity of a fully numerical treatment in the time domain [189, 190].

[VII] As a resonance process, a LZ transition necessarily is non-perturbative.

Note that this now not necessarily coincides with $\Omega\Delta m = \Delta\epsilon$, because the change of the other orbital elements, i.e., precession of $\{\kappa, \xi\}$ now also appear in the resonance condition. Again, the resonances can be classified as being of the Bohr ($\mathcal{B}$), fine ($\mathcal{F}$) and hyperfine ($\mathcal{H}$) type, with the leading order α-scaling given by

$$\Delta\epsilon \sim \frac{\alpha^p}{M}\left[1 + \delta_{p,7}\left(\frac{\tilde{a}}{\alpha} - 1\right)\right], \quad p = \{3, 5, 7\}\ , \text{for } \{\mathcal{B}, \mathcal{F}, \mathcal{H}\} \tag{7.33}$$

There are three further aspects of the microphysics mentioned above that we will not track explicitly in this work – self-gravity, ionization and self-interactions.

7.3.2 One- and Two-Level Atom

Let us now consider a cloud saturated by superradiance in the state $|n_a l_a m_a\rangle$. Because this time we also want to be able to track changes in occupation due to decay of the states, as well as changing mass of the BH, in this chapter, we are more careful in setting up the system. In the non-relativistic limit, the density of the cloud is $\rho = \mu N_c \mathcal{R}_a^2 Y_a Y_a^*$, where N_c is the occupancy of the cloud, i.e., the particle number, while the spin is $S_c = m_a N_c$. We also define the dimensionless occupancy

$$n_c \equiv N_c/(GM_0^2) = \frac{M_c}{M_0\alpha_0}\,, \tag{7.34}$$

where M_0 is the initial mass of the BH before superradiance. The second equality, was found by rewriting $M_0 = \alpha_0/(G\mu)$, with the initial α_0. As superradiance generates only $m_a > 0$ states, in this setup we have $\hat{\boldsymbol{S}} \parallel \boldsymbol{S}_c$. We will use $n_c \simeq \alpha$ for the estimates in this chapter and the first half of Ch. 8, and do a more refined discussion in Sec. 8.3.

Although individual wavefunctions of the cloud are described by the spherical harmonics Y_a, the multipolar decomposition is obtained by a projection of the density ρ on the spherical harmonic basis. This means even states with $l_a > 2$ will generate a non-zero quadrupole for the cloud. In particular, Q_{lm} vanishes for $m \neq 0$ and is importantly time-independent

$$Q_{l0} \quad = \quad \mu N_c r_c^l \left[I_r I_\Omega\right]^{(aa|l0)}\,, \tag{7.35}$$

making the spin frame also the principal axis frame. The quadrupole of the gravitational atom is dominated by the cloud, as we find for the scaling

$$\frac{Q_c}{Q_{\rm BH}}\Big|_{20} \sim \frac{\tilde{a}}{\alpha^5} + \mathcal{O}(\alpha^{-4})\,, \tag{7.36}$$

so we will ignore the BH contribution to the quadrupole from here on.

We now introduce the second state $|n_b l_b m_b\rangle$ and allowing for level mixing between the bound states:

$$\rho = \mu N_c \left|c_a(t)\mathcal{R}_a Y_a + c_b(t)\mathcal{R}_b Y_b\right|^2\,, \tag{7.37}$$

where c_i are now dimensionless *relative* occupancies of the two states $\{|a\rangle, |b\rangle\}$, while the overall particle number is given by N_c. Due to unitarity $|c_a|^2 + |c_b|^2 = 1$ and the $U(1)$ symmetry, one needs only two parameters to describe this system, although the c_i are complex numbers. Therefore, we can define

$$c_a \equiv \sqrt{\frac{1+\sigma}{2}} \exp\left[i(-\Delta\epsilon\, t/2)\right] , \tag{7.38}$$

$$c_b \equiv \sqrt{\frac{1-\sigma}{2}} \exp\left[i(\delta + \Delta\epsilon\, t/2)\right] , \tag{7.39}$$

and then use the canonically conjugate variables (σ, δ) [191] to describe the dynamics of the cloud sector. Note that $\sigma = 1$ ($\sigma = -1$) corresponds to a cloud only populated by the $|a\rangle$ ($|b\rangle$) state. In this way we explicitly track the microscopic degrees of freedom of the cloud, and the full phase space is given by $\mathbb{P} = \mathbb{E} \cup \mathbb{S} \cup \{\sigma, \delta\}$. Working in the (g,k)-overtone expansion Eq. (7.28), one can derive the Hamiltonian of the two-state system in two steps: We integrate the Lagrangian density of the cloud (see Ref. [25]) over space, and use the field redefinition Eq. (7.30) and Eq. (7.38) to obtain $2L_\mathrm{c}/N_\mathrm{c} = \dot{\delta}(\sigma - 1) + \Delta\epsilon\sigma - 2\sqrt{1-\sigma^2}\sum_{l,m,g,k} \eta_{g,k} \cos(\delta - \Sigma_{g,k})$.[VIII] We then apply the Legendre transformation to L_c, with the generalized and canonical conjugate coordinates (δ, σ). This gives

$$H_\mathrm{c} = \frac{N_\mathrm{c}}{2}\left(-\Delta\epsilon\sigma + 2\sqrt{1-\sigma^2}\sum_{l}\sum_{m=1}^{l}\sum_{g,k}\eta_{g,k}^{(ab|lm)}\cos(\delta - \Sigma_{g,k})\right) , \tag{7.40}$$

from this, the equations of motion of σ and δ follow:

$$\left.\frac{d\sigma}{dt}\right|_{g,k}^{lm} = -2\eta_{g,k}\nu\,, \tag{7.41}$$

$$\left.\frac{d\delta}{dt}\right|_{g,k}^{lm} = -\Delta\epsilon - 2\eta_{g,k}\frac{\sigma}{1-\sigma^2}u\,, \tag{7.42}$$

where we have defined two variables that will become convenient later:

$$u \equiv \sqrt{1-\sigma^2}\cos\left(\delta - \Sigma_{g,k}\right), \tag{7.43}$$

$$\nu \equiv -\sqrt{1-\sigma^2}\sin\left(\delta - \Sigma_{g,k}\right). \tag{7.44}$$

A particular choice of the phase ansatz in Eq. (7.38) allows us to remove the explicit time dependence in the multipole moments and write

$$\begin{aligned} Q_{lm} = \frac{1}{2}\mu N_\mathrm{c} r_c^l \times \Big[&\sqrt{1-\sigma^2} I_r^{(ab|lm)}\left(e^{i\delta} I_\Omega^{(ab|l\bar{m})} + e^{-i\delta} I_\Omega^{(ba|l\bar{m})}\right)(1-\delta_{m0}) \\ &+ \left(I_r^{(aa|l0)} I_\Omega^{(aa|l0)}(1+\sigma) + I_r^{(bb|l0)} I_\Omega^{(bb|l0)}(1-\sigma)\right)\delta_{m0}\Big] , \end{aligned} \tag{7.45}$$

where $\bar{m} \equiv -m$. Note that this expression reduces to Eq. (7.35) when $\sigma \to 1$. Given l and paring Q_{lm} and $Q_{l\bar{m}}$ terms in the sum Eq. (7.21) one can find, using $I_\Omega^{(ba|lm)} = I_\Omega^{(ab|l\bar{m})}$ and assuming that

[VIII] Here, L_c is the Langrian, not the magnitude of angular momentum.

the selection rules are satisfied, and using Eq. (7.28), the contribution of the mixing terms to the multipolar potential

$$V_Q \supset N_{\rm c}\sqrt{1-\sigma^2}\sum_l\sum_{m=1}^{l}\sum_{g,k}\eta_{g,k}^{(ab|lm)}\cos\left(\delta-\Sigma_{g,k}\right). \tag{7.46}$$

The mixing terms in $H_{\rm c}$ (Eq. (7.40)) and V_Q (Eq. (7.46)) that connect the orbital and gravitational atom phase subspaces are exactly the same and are thus balancing the outflow of energy-momentum from one subspace with the inflow to the other. In this way the Hamiltonian governing the dynamics on $\mathbb{E}$ is $H_{\rm K}+H_{\rm c}$, identifying $H_{\rm I}$ with $H_{\rm c}$. This discussion can be straightforwardly generalized to multi-level systems. However, as explained in Ch. 8, most of the phenomenologically relevant dynamics can be represented by an effective two-level mixing.

To find the evolution of the principle orbital elements, we plug the Hamiltonian Eq. (7.40) as $H_{\rm I}$ into Eq. (7.13), Eq. (7.14) and Eq. (7.15) and obtain the flow of the principal elements due to mixing terms

$$\left.\frac{da}{dt}\right|_{g,k}^{l} = \frac{2}{q}\sqrt{\frac{a(1+q)}{\mathcal{M}^3}}N_{\rm c}(g-k)\eta_{g,k}\nu\,, \tag{7.47}$$

$$\left.\frac{de^2}{dt}\right|_{g,k}^{l} = \frac{2}{q}\sqrt{\frac{1+q}{a\mathcal{M}^3}}\sqrt{1-e^2}N_{\rm c}\left(\sqrt{1-e^2}(g-k)-g\right)\eta_{g,k}\nu\,, \tag{7.48}$$

$$\left.\frac{d\cos\iota}{dt}\right|_{g,k}^{l} = \frac{1}{q\sqrt{1-e^2}}\sqrt{\frac{1+q}{a\mathcal{M}^3}}N_{\rm c}\left(m-g\cos\iota\right)\eta_{g,k}\nu\,. \tag{7.49}$$

In addition, the positional elements χ, Υ and ϑ will have a flow induced by $H_{\rm I}$ that is proportional to $\eta_{g,k}u$, but also a flow induced by the $m=0$ that is non-zero also for gravitational atoms in a single state. For details, see App. A.1.

7.4 Dynamics via Energy-Momentum Balance

Having derived the full set of equations for all orbital elements, we are now going to compare it to the single approach that has been used in all pre-existing literature on superradiance in binaries, usually dubbed balance equations.

We give a brief summary of the arguments, which we will then develop in detail: The energy and angular momentum of the cloud in the IAA are taken to be $E=\sum_i\epsilon_i|c_i|^2$ and $L=\sum_i m_i|c_i|^2$. For clouds that are in a superposition of states, these results are erroneous, which we have shown by deriving the Hamiltonian of the non-relativistic scalar field in the Kerr metric: Eq. (7.40) contains an interaction term, which is non-zero when both states are in a superposition. For equatorial orbits, there are only two degrees of freedom of the orbit we need to solve for: a and e. This has been done by balancing the energies and the L_z of the angular momentum, assuming the orbit lies in the x,y-plane and L_z and L_y to be zero. These assumptions are true, but ignoring the interaction term of the Hamiltonian, even for equatorial orbits, balancing these fluxes leads to an erroneous equation for the eccentricity evolution. The treatment of inclined orbits in Ref. [154]

then assumed the orbit could be initially inclined with respect to the spin of the cloud with a non-zero L_x. However, it was then assumed that the spin of the central BH and the cloud are forced to be kept aligned with the z-axis. During transitions, the whole system then could only change L_z, while keeping L_x of the orbit fixed. While this is technically changing the inclination of the orbit, since fixing L_x while changing L_z changes the angle to the z-axis, no actual new dynamic degree of freedom has been introduced. $\dot{L}_x = 0$ and $\dot{L}_y = 0$ are ad-hoc assumptions. Setting up the full balance equations by using the Runge-Lenz-Vector shows that such a setup is inconsistent. And this stays true even in the case when one includes the interacting part of the Hamiltonian. The inconsistency stems from an incomplete treatment of what defines a general orbit: Since in non-relativistic mechanics the movement of an object in three dimensional space is defined by position $\boldsymbol{x}$ and momentum $\boldsymbol{p}$, we need six independent parameters to describe the position of a binary companion. Even for equatorially aligned orbits, when all the dynamics are necessarily restricted to a plane, we have included a and e, φ_*, but the position of the periapsis from which the true anomaly is measured, χ, was assumed to be fixed. In the full dynamics this angle with respect some fixed coordinate system is dynamic. For fully general orbits, we need two more variables, which are inclination ι and angle of the ascending node Υ. As we have seen, the dynamics of these two are intertwined.

The idea of the balance equations are to balance conserved quantities - the orbital energy H_K, angular momentum $\boldsymbol{L}$ and the eccentricity (Laplace-Runge-Lenz) vector

$$\boldsymbol{e} = \frac{\dot{\boldsymbol{r}} \times (\boldsymbol{r} \times \dot{\boldsymbol{r}})}{\mathcal{M}(1+q)} - \frac{\boldsymbol{r}}{r} \tag{7.50}$$

with the "fluxes" from the perturbations and emissions to infinity via GWs. From here, one can obtain the time dependence of five orbital parameters. The conservation of $\boldsymbol{e}$ follows from the hidden SO(4) symmetry [182, 192]. In principle, these conserved quantities have $1 + 3 + 3 = 7$ components. However, the constraints $\boldsymbol{L} \cdot \boldsymbol{e} = 0$ and $(L/(\mu\Lambda))^2 + e^2 = 1$ lead to 5 independent equations. In fact, it is enough to use the conservation of H_K and $\boldsymbol{L}$ together with the kinematic constraints in order to solve for $\dot{\mathbb{E}}\backslash\{\vartheta\}$ [193, 194]. Note that the same $SO(4)$ hidden symmetry is responsible for the degeneracy in the hydrogenic $\mathcal{B}$ spectrum [187]. Using how these vectors are related to the the orbital elements by geometry, we can relate the temporal change of the latter to

the change of these vector elements, which gives:

$$\begin{aligned}
\frac{da}{dt} &= \frac{2a^2}{\mathcal{M}^2 q}\dot{H}_{\rm K}\,, \\
\frac{de}{dt} &= \frac{1}{ae\mathcal{M}^2 q}\Big[a^2\dot{H}_{\rm K}\left(1-e^2\right) - \sqrt{a\left(1-e^2\right)M(q+1)}\,\times \\
&\quad \Big(\sin\iota(\dot{L}_x\sin\Upsilon - \dot{L}_y\cos\Upsilon) + \dot{L}_z\cos\iota\Big)\Big]\,, \\
\frac{d\iota}{dt} &= -\frac{1}{q}\sqrt{\frac{1+q}{a\mathcal{M}^3(1-e^2)}}\,\times \\
&\quad \Big((-\dot{L}_x\sin\Upsilon + \dot{L}_y\cos\Upsilon)\cos\iota + \dot{L}_z\Big) \\
\frac{d\Upsilon}{dt} &= \frac{1}{q}\sqrt{\frac{1+q}{a\mathcal{M}^3(1-e^2)}}\frac{\cos\Upsilon}{\sin\iota}\Big(\dot{L}_x + \dot{L}_y\tan\Upsilon\Big)
\end{aligned} \tag{7.51}$$

So far, this is a purely kinematic statement — there is no input on dynamics. The dynamics will only enter by prescribing the fluxes $\dot{H}_{\rm K}$ and $\dot{\boldsymbol{L}}$. For example, performing the orbital average and plugging in the GW emission fluxes, one obtains equations for the evolution of $\dot{a}, \dot{e}$ due to RR [125, 126]. In Refs. [1, 154], the following identification has been utilized for a two-level system, considering only the cloud contribution to the fluxes, which, as already mentioned above, is called the isolated atom approximation (IAA):

$$\dot{H}_{\rm K} = -\dot{E}_c\,,\; E_c = N_{\rm c}(\epsilon_a|c_a|^2 + \epsilon_b|c_b|^2)\,, \tag{7.52}$$

$$\dot{L}_z = -\dot{S}_c\,,\; S_c = N_{\rm c}(m_a|c_a|^2 + m_b|c_b|^2)\,, \tag{7.53}$$

$$\dot{L}_x = 0\,, \dot{L}_y = 0\,. \tag{7.54}$$

As already mentioned, the last two equations are inserted ad-hoc. They make sense in the equatorial limit, because there is no obvious way to extend the dynamics into an additional dimension[IX], but Ref. [154] assumed they must be true even for misaligned orbits, because the cloud is assumed to have spin only in the z-direction of the central BH spin, while in turn also the spin of the central BH is assumed to be fixed. We conclude that both of these assumptions are unjustified in general orbits, since even in the picture of balance equation it should be assumed that the gravitational atom reacts to changes in orbital precession and inclination. Because Ref. [154] was mostly interested in EMRIs, implicitly assuming that the spin axis of the gravitational atom is the fixed reference frame, the assumption of $\dot{S}_x = \dot{S}_y = 0$ may seem as an acceptable approximation, but still leads to a wrong set of equations. The change of the orbital elements that follows from the assumption above doesn't agree with the equations Eq. (7.13)-Eq. (7.18). In fact, the IAA is missing three important facts:

(i) The angular orbital elements $\{\vartheta, \chi, \Upsilon\}$ have a non-Keplerian flow due to both the conservative and the mixing part of V_Q. This evolution, as we will discuss in App. A, influences the position

[IX] With the exception of hyperfine transitions that naturally generate a non-zero x and y component of the cloud's spin.

and the duration of the resonances. This contribution, however, can be typically be ignored in the range of the parameters that we consider for $\mathcal{H}/\mathcal{F}$ resonances.

(ii) Let us focus, for simplicity, on the two-state system, ignoring the decay processes. Using Eq. (7.38) to rewrite Eq. (7.52) as $\dot{E}_c = -N_c \Delta\epsilon\dot{\sigma}/2$ and comparing with the full internal energy, i.e., the Hamiltonian Eq. (7.40) one finds that the interacting term is missing. In order to understand the impact of this term in the energy flux, consider for simplicity the resonance on the co-rotating circular orbit, from Eq. (7.40):

$$\begin{aligned}\frac{2}{N_c}\frac{dH_c}{dt} &= -\Delta\epsilon\dot{\sigma} - 2\eta\Big\{ (\Delta\epsilon - \Delta m\Omega)\,\nu \\ &\quad + \Big[\frac{\partial_t\eta}{\eta}u + \Delta m\left(\dot{\vartheta} - \Omega\right)\nu\Big]\Big\} \end{aligned} \tag{7.55}$$

The term in the second row in the bracket [...] can be shown to be zero from Eq. (7.16). The remaining part of the interacting term in the bracket {...} will be approximately zero during resonant floating and evolving $\dot{a}$ using IAA will give a correct result. However, as already hinted, it will lead to a different scaling far away from the resonance, which is important for the non-resonant mixing due to a large decay width. See Sec. 8.4 for a discussion of the latter.

(iii) The precession of the orbital momentum also enters directly in the Eq. (7.51) for the evolution of $\dot{\mathbb{E}}/\{a\}$. Ignoring these terms, for inclined orbits, leads to erroneous dynamics, even for the resonant dynamics in the EMRI limit considered in Ref. [154], as the energy-momentum budget is not appropriately allocated;

We discuss a few of these differences in detail for equatorial and then for general orbits.

7.4.1 Equatorial Orbits

Let us first consider the equatorial regime and the $e \ll 1$ expansion to examine further differences between the IAA and the correct approach, comparing the predicted evolution. Dividing the evolution equations for Ω and e from the Hamiltonian and from the IAA we find

$$\frac{d\Omega_{\rm IAA}}{d\Omega}\Big|^{lm}_{g,k} = \frac{\mathfrak{f}_{g,k}}{\mathfrak{f}(t)}\,, \tag{7.56}$$

$$\frac{d(e^2)_{\rm IAA}}{d(e^2)}\Big|^{lm}_{g,k} = \frac{\mathfrak{f}_{g,k}}{\mathfrak{f}(t)}\frac{\sqrt{1-e^2}-\mathfrak{f}}{\sqrt{1-e^2}-\mathfrak{f}_{g,k}}\,, \tag{7.57}$$

where the index IAA denotes the time evolution in the isolated atom approach, and the same quantity without index is the Hamiltonian result. We see from the above comparison that in the vicinity of a floating resonance, when $\mathfrak{f}(t) \approx \mathfrak{f}_{g,k}$, the evolution in IAA of both Ω and e^2 is in agreement with the general result. We also point out that Ref. [154] usually just linearized the whole problem and ignored time dependence of any frequency in the backreaction at the resonance. For narrow floating resonances, this is fine. However, away from the resonance, the IAA scales with

$1/\mathfrak{f}(t)$ instead of the correct result $1/\mathfrak{f}_{g,k}$, which means for low frequency, $\mathfrak{f} \ll \mathfrak{f}_{g,k}$ it significantly overestimates the strength of non-resonant mixing.

On the counter-rotating equatorial orbits, even the resonance is incorrectly predicted by the IAA as the term {...} in Eq. (7.55) doesn't cancel. As the sign of $\dot{\Omega}$ in IAA is tied to $\Delta\epsilon$, the resonance must work in the direction of floating for $\Delta\epsilon < 0$, which is not the case on counter-rotating orbits (see Sec. 8.2.2.1).

Finally, note that the difference for Ω persists also in the circular limit. In fact, as already discussed in Ch. 4, in the circular limit one can use the IAA balance approach by balancing either energy or the spin of the cloud, but these different options give inconsistent results away from the floating resonance. The latter option was originally used in Ref. [26] and it coincides with the correct general result as $\boldsymbol{S}_c$ doesn't have an interacting term, in contrast with Eq. (7.40).

7.4.2 Inclined Orbits

For the ratio of the two different results of the inclination evolution equations, we find

$$\left.\frac{d\iota_{\rm IAA}}{d\iota}\right|_{g,k}^{lm} = \frac{\Delta m \sin^2(\iota)}{m_\star - g\cos(\iota)}. \tag{7.58}$$

This equation really *only* agrees in the equatorial limit when $g = m_\star$ and $\iota = 0$ and then predicts that equatorial orbits remain equatorial. As explained above, not allowing L_x and L_y to change leads to a wrong prediction for the inclination behavior, because in general orbits, the evolution of ι and Υ are related and one cannot force non-precession of inclined orbits.

However, an even more important difference for general orbits is the behavior of eccentricity for inclined orbits: Derived with the conditions of the IAA approach, the eccentricity evolution contains an explicit factor of $\cos\iota$. For $\Delta m = -g$, this factor eradicates the fixed points in eccentricity for any non-zero inclination. This led the authors of Ref. [154] to conclude that there are no eccentricity fixed points for inclined orbits and that *if* adiabaticity could remain strong enough, an inclined orbit, in principle, could grow eccentricity towards unity, decreasing inclination and then, when equatorialized, lose eccentricity again towards the fixed point. While in reality, floating could never last long enough for that to happen anyway, our results show that this conclusion is wrong even in principle. Assuming a very extended period of floating, we show the correct behavior in the (e, ι)-phase space in Fig. 7.2. However, this is the behavior for the dominating term in the g-expansion. As we will discuss in Ch. 8, for general inclined orbits the actual dynamics become even more non-trivial, because several terms from the expansion in $-l < g < l$ can be active simultaneously. We point out, that the correct balance approach can lead to the correct equations of motion, but makes it necessary to also define the angular momentum of the cloud correctly, including the mixing term.

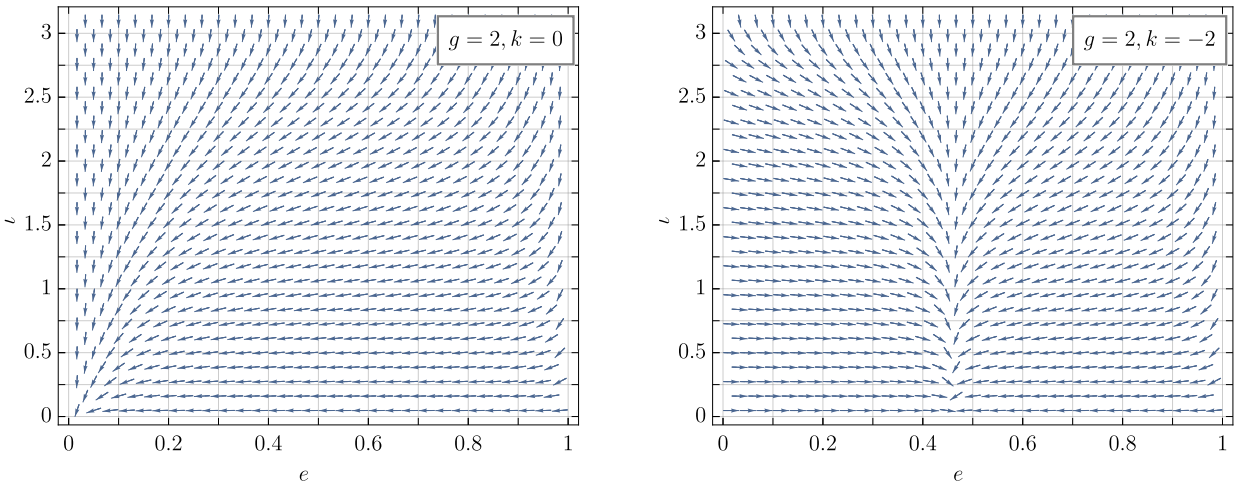

FIG. 7.2: Visualization of the flow of eccentricity e in Eq. (8.12) and inclination ι in Eq. (8.21) during floating, for $g = -\Delta m = 2$ and $k = 0$ ($k = -2$) on the left (right), to show that the eccentricity fixed points (0 for $k = 0$ and 0.46 for $g = 2, k = -2$) are valid for all inclinations. This is a correction of Fig. 1 in Ref. [171] and Fig. 6 in Ref. [154]. The binary could follow a path in this parameter space if one unrealistically assumes a fixed $\eta_{g,k}$. Note however, that no realistic system with large initial inclination can ever follow a trajectory of significant length in this parameter space, since the overlap is Wigner-suppressed and the floating time finite. Additionally, the whole formalism breaks down for eccentricities close to unity, because adiabatic averaging over orbits is not valid anymore [195]. Additionally, if other terms in the inclination expansion in g are important, the combined effects can differ from the evolution of the dominant term, see Ch. 8.

Chapter 8 Dynamics in General Orbits

8.1 Overview

In this chapter, we describe the most salient aspects of the cloud-binary dynamics arising from the full set of equations derived in Ch. 7. First, in Sec. 8.2 we describe the quasi-adiabatic co-evolution of the BH and the cloud. In Sec. 8.2.1-8.2.2.2 we describe the mixing dynamics in three different aspects: First, the dynamics in the cloud sector, including time-dependent treatment of the central BH mass during the mixing, followed by the full dynamics on orbits with (anti-)aligned and misaligned $\boldsymbol{L}$ and $\hat{\boldsymbol{S}}_{\rm GA}$, respectively. After briefly discussing how to find the cloud mass consistently in Sec. 8.3, we discuss how to treat non-perturbative mixing with strongly decaying states, an important effect that has so far not been treated consistently in the literature, in Sec. 8.4. In some of these sections we provide results of numerical simulations using simplified parameter values. Although these deviate from realistic scales that are computationally expensive, they suffice to visualize the phenomenological consequences. All of these numerical results will incorporate the full dynamics of eccentric orbits without using the Jacobi-Anger expansion. We compare results from one of the g-terms in the inclination expansion with the full sum over g where necessary. See App C for details on the numerics. Finally, in Sec. 8.5 we review the history of realistic binaries incorporating everything we discussed so far. This is going to challenge the results from Part 2 by incorporating effects that have not been understood at that point. This chapter aims to establish possible dynamics that have so far been missed and that only a full treatment of the co-evolution of BBHs and the superradiant cloud can cover, while we close with the conclusion that the complete phenomenological impact of superradiance in binaries is yet to be fully understood.

8.2 BH-Cloud Co-Evolution

8.2.1 Mixing Dynamics: Cloud Sector

We set the stage by considering a decaying two-level system. Ignoring $\dot{\chi}$ and $\dot{\Upsilon}$, as discussed in Sec. 7.3.1, the strongest effect of level mixing occurs at the (overtone) resonance

$$\Omega_{g,k} = \mathfrak{f}_{g,k}\Omega_0\,, \quad \mathfrak{f}_{g,k} \equiv \frac{-\Delta m}{g-k}\,. \tag{8.1}$$

The condition $\mathfrak{f}_{g,k} > 0$ is a necessary condition for the resonance, e.g., in the equatorial limit only $g = \mp\Delta m$ overtones have a support, which makes resonances possible for $k/\Delta m > -1$ ($g = -\Delta m$) and $k/\Delta m < 1$ ($g = \Delta m$). The resonance under considerations is *narrow* if it starts at $\mathfrak{f} \simeq \mathfrak{f}_{g,k}$ or *wide* if the non-trivial mixing occurs for $\mathfrak{f} \ll \mathfrak{f}_{g,k}$. We will discuss the latter case in 8.4.

At the resonances, the cloud dynamics needs to be solved simultaneously with the orbital dynamics. Assuming a background radiation reaction-driven dynamics of the orbital elements $\{a, e\}$ we perform a rescaling very similar to what we did in Ch. 5:

$$z_{g,k} \equiv \frac{\eta^2_{g,k}}{\hat{\gamma}_{g,k}}\,, \quad v^{(\pm)}_{g,k} \equiv \frac{\Gamma_\pm}{\sqrt{\hat{\gamma}_{g,k}}}\,, \quad w_{g,k} \equiv \frac{\Omega_{g,k}}{\sqrt{\hat{\gamma}_{g,k}}}\,, \quad \hat{\gamma}_{g,k} \equiv |g-k|\mathfrak{f}_k^{11/3}\gamma_0\,, \quad \tau \equiv \sqrt{\hat{\gamma}_{g,k}}t\,, \tag{8.2}$$

The relative and total magnitude of $z_{g,k}$ and $v_{g,k}$ will characterize the LZ-transitions in the same way as already discussed in Ch. 5.

In the previous section, we implicitly assumed that the superradiant growth of $|a\rangle$ had saturated, while the decay rate of $|b\rangle$ was much longer than all other timescales in the problem. We will now relax these assumptions and allow for both positive and negative decay width of the states $\{|a\rangle, |b\rangle\}$, as well as the co-evolution of the background BH. The decay of the states $\{|a\rangle, |b\rangle\}$ makes the cloud dissipative, but the whole gravitational atom can still be considered an unitary system. However, the fact that the cloud decays into GWs via axion annihilation, and the possibility of level transition makes the gravitational atom truly an open system [37, 88, 117, 120, 164, 165, 196]. These dissipative processes make the system non-symplectic. This means, still focusing on a two-state system, on top of the phase space (σ, δ), we also need to prescribe the instantaneous occupancy of the cloud $n_{\rm c}$. The equation of motion for δ is the same as in Eq. (7.42), while the one for σ is modified and we introduce

$$\left.\frac{d\sigma}{dt}\right|^{lm}_{g,k} = -2\eta_{g,k}\nu - \bar{\Gamma}^-_{ab}(1-\sigma^2)\,, \tag{8.3}$$

$$\left.\frac{dn_{\rm c}}{dt}\right|^{lm}_{g,k} = -(\bar{\Gamma}^+_{ab} + \bar{\Gamma}^-_{ab}\sigma)n_{\rm c}\,, \tag{8.4}$$

$$\bar{\Gamma}^\pm_{ab} \equiv \bar{\Gamma}_a \pm \bar{\Gamma}_b\,, \tag{8.5}$$

where $\bar{\Gamma}_i$ denotes the sum of the decay (or growth rate if $\Gamma < 0$) of state $|i\rangle$ and possibly its GW emission $\Gamma_{\rm GW}$.

In order to model the co-evolution of cloud and BH superradiance, we use the quasi-adiabatic approach, i.e., we assume that the evolution of the system of BH and cloud can be treated as a sequence of $|\text{Kerr}\rangle \otimes \sum_a |nlm\rangle$ states as[I] $M \gg \epsilon_a \gg \Delta\epsilon_{ab} \gg \Gamma_a$. The co-evolution is balanced at the horizon for mass $\dot{M} = -\dot{M}_\text{c}$ and angular momentum $\partial_t(\tilde{a}M^2) = -\dot{S}_\text{c}$, where M_c is the mass of the cloud [82, 163]. For a two-state system we have:

$$\frac{d\alpha}{dt} = \alpha_\text{sat}^2 n_\text{c}(\Gamma_{ab}^+ + \Gamma_{ab}^-\sigma)\,, \tag{8.6}$$

$$\frac{d\tilde{a}}{dt} = \left(\frac{\alpha_\text{sat}}{\alpha}\right)^2 n_\text{c}\left(m_a + \Delta m\frac{(1-\sigma)}{2}\frac{\Gamma_{ab}^+ - \Gamma_{ab}^-}{\Gamma_{ab}^+ + \Gamma_{ab}^-\sigma} - 2\alpha\tilde{a}\right)\left(\Gamma_{ab}^+ + \Gamma_{ab}^-\sigma\right)\,, \tag{8.7}$$

where the index "sat" refers to the values when the cloud is saturated in state $|a\rangle$. Regarding the GW emission, we consider only the dominant channel where two axions annihilate to a graviton and where the emission rate is given by [165]

$$\Gamma_\text{GW} \simeq \frac{M_\text{c}}{M^2} H_a \alpha^{4m_a+10}\,, \quad H_{|211\rangle} \simeq 0.025\,, \quad H_{|322\rangle} \simeq 2\cdot 10^{-7}\,. \tag{8.8}$$

Typically, in the vicinity of a resonant transition we can ignore the effect of the GW depletion of the cloud and take $\bar{\Gamma}$ to just be decay or growth rates of the states $\bar{\Gamma} \approx \Gamma_i$. In that case, n_c can only change because particles, and with that mass, are exchanged with the central BH. This means from the evolution of n_c, we can directly calculate the change of α. This makes Eq. (8.6) a redundant equation, allowing us to close the system by tracking the evolution of $\{n_\text{c}, \tilde{a}\}$ on top of $\{\delta, \sigma\}$, as

$$\alpha \simeq \alpha_\text{sat}\left[1 + \alpha_\text{sat}(n_\text{c,sat} - n_\text{c})\right]\,. \tag{8.9}$$

In Fig. 8.1 we show comparisons of early resonances with different strength of the decay rate and how they change floating and eccentricity growth.

8.2.2 Mixing Dynamics: Orbit

8.2.2.1 Mixing Dynamics: Equatorial Orbits

It is instructive to go back to equatorial orbits. They not only have different dynamics far away from the resonance in the full formalism, but can also be treated more consistently. This discussion also sets the stage for inclined orbits in the next section. Because they are phenomenologically more important, we are going to concentrate on transitions where the cloud loses energy $\Delta\epsilon < 0$.

[I] The only chance for the violation of the adiabatic theorem ($\Gamma_b \simeq \Delta\epsilon_{ab}$; see Ref. [187]), for $\alpha < 1$, to occur is for $\mathcal{F}$ transitions to spherical $l = 0$ states, as $\Gamma_b \sim \alpha^5$ and $\Delta\epsilon_{ab} \sim \alpha^4$. We have checked with an explicit calculation for $|322\rangle \to |300\rangle$ that for the range of α that we consider $\Delta\epsilon_{ab} > 2\Gamma_b$, and thus we don't expect a significant departure from the adiabaticity.

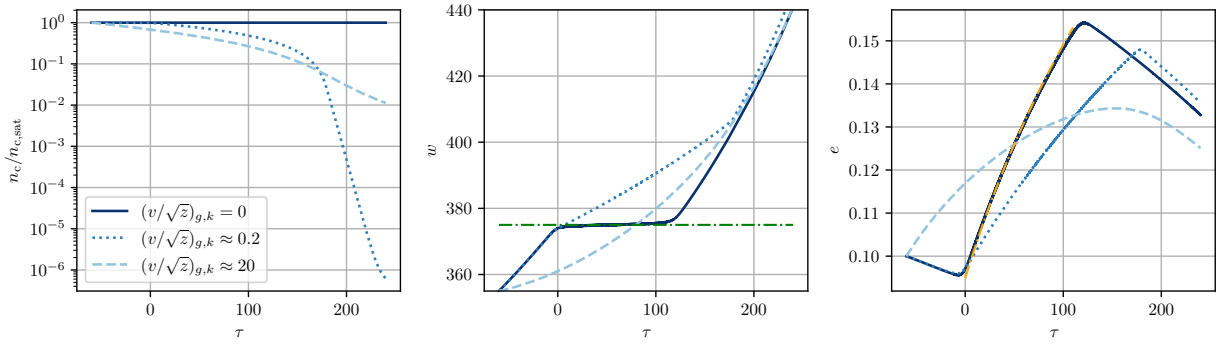

FIG. 8.1: We show $n_c/n_{c,sat}$ (left), orbital frequency w (center) and eccentricity e (right) for a $\Delta m = -3$, $g = 3$, $k = -1$ early resonance on a co-rotating orbit ($\iota = 0$). Dark blue shows the resonance for zero decay rate of the second state, which provides perfect floating at the resonance frequency, the latter indicated by the green dash-dotted line in the center plot. The orange dash-dotted line in the rightmost plot shows the growth of eccentricity as semi-analytically expected, which perfectly agrees with the numerical result for $\dot{\alpha} = 0$. The medium blue, dotted lines show the resonance in the weak-decay regime ($(v/\sqrt{z})_{g,k} \ll 1$), where the eccentricity still grows strongly, but the floating behavior is changed because due to the decay of particles back into the BH, α and consequently the resonance frequency changes. The light blue, dashed lines show the strong decay regime ($(v/\sqrt{z})_{g,k} \gg 1$), for which there is no clear resonance behavior, while eccentricity still grows.

Rewriting Eq. (7.47) in terms of frequency Ω and plugging in Eq. (7.40) for H_I we find

$$\frac{d\Omega}{dt} = \gamma_0 \mathfrak{f}^{11/3} \left[f(e) - (g-k) \left(\frac{\mathfrak{f}}{\mathfrak{f}_{g,k}} \right)^{-7/3} \left(\frac{n_c}{n_{c,sat}} \right) b_{g,k} \sqrt{z_{g,k}} \nu \right], \tag{8.10}$$

$$b_{g,k} \equiv \sqrt{\frac{15}{32}} \sqrt{|g-k|} \mathfrak{f}_{g,k}^{-7/3} \sqrt{\frac{1+q}{q^3}} \frac{n_{c,sat}}{\sqrt{M_0 \Omega_0}}, \tag{8.11}$$

where $b_{g,k} > 0$ is the orbital backreaction parameter. Here we have introduced $n_{c,sat}$, which is the dimensionless occupancy after the cloud has reached saturation. We note that we use a slightly different notation w.r.t. Ch. 5 for $\{b_{g,k}, z_{g,k}, v_{g,k}, w_{g,k}\}$. The biggest difference is that there is no explicit γ_0 in $b_{g,k}$. Also note that $\eta_{g,k}$ can be negative, but this will only influence the sign of u and ν. However, we will see that for general orbits, the relative sign of the different $\eta_{g,k}$ will matter. To simplify the notation, we assume $\eta_{g,k} > 0$ in the following. Written in this form, we can easily translate the equation to a dimensionless form $dw/d\tau$ with $w \equiv \Omega/\sqrt{\gamma_0}$ and $\tau \equiv t\sqrt{\gamma_0}$ by dividing both sides by γ_0. We assume that this γ_0 is constant and refers to a resonant frequency for either the initial α, or the value for the saturated cloud. In the latter case, $b_{g,k}$ would need to be rescaled accordingly.

We already know that a significant backreaction $b_{g,k} \gg 1$ makes the problem non-linear, leading to floating orbits and stalling the frequency if $\Delta\epsilon < 0$. For early resonances, we find fixed points in eccentricity evolution, as from Eq. (7.48) and Eq. (8.10) one finds for the eccentricity during

floating

$$\left.\frac{de^2}{dt}\right|_{\rm fl} = \frac{2}{3}\mathfrak{f}^{8/3}\frac{\gamma_0}{\Omega_0}f(e)\sqrt{1-e^2}\left(\frac{g(e)}{f(e)} - \frac{g}{-\Delta m}\mathfrak{f}_{g,k}\right) . \tag{8.12}$$

We know from Ch. 5 that on co-rotating orbits $g = -\Delta m$, early overtones with $\mathfrak{f}_{g,k} < 1$ have fixed points at $e_{\rm cr} \in [0.3, 0.6]$, while for late overtones $\mathfrak{f}_{g,k} \geqslant 1$, eccentricity decays faster than in vacuum as $e_{\rm cr} = 0$.

In the new formalism, especially using the Block sphere variables u and ν, the derivation of several possibilities of "resonance breaking" that have been discussed in the literature become much easier to derive. Assuming a successful floating, from Eq. (8.10) we get

$$\langle\nu_{\rm fl}\rangle \simeq \frac{f(e)}{|g|b_{g,k}\sqrt{z_{g,k}}}\left(\frac{n_{\rm c}}{n_{\rm c,sat}}\right)^{-1} . \tag{8.13}$$

As the population transfer ensues, σ will, neglecting the pre-resonant effects as well as a possible strong decay rate of the second state, move from the initial value of $\sigma = 1$ to $\sigma \to -1$. From that we find via Eq. (7.44) that $\langle\nu\rangle$ will follow a parabolic-like trajectory from $\langle\nu\rangle(-\infty) = 0$ to $\langle\nu\rangle(+\infty) = 0$. This means, the estimate Eq. (8.13) also represents a maximal value achievable for perfect floating that must necessarily satisfy the constraint $|\langle\nu_{\rm fl}\rangle| \leqslant 1$. We will see later from Eq. (8.28) that during floating, $\dot{\nu}$ must follow the sign of σ, and thus the bracket in the first term of Eq. (8.28) must be positive. These two constraints yield

$$n_{\rm c} > n_{\rm c}^{\rm (cr)} \equiv n_{\rm c,sat}\frac{f(e)}{|g|b_{g,k}\sqrt{z_{g,k}}} \times \max\left[1\,,\, \frac{|v_{g,k}^{(-)}|}{2\sqrt{z_{g,k}}}\right] . \tag{8.14}$$

The condition above is a time-dependent statement, since in general $n_{\rm c} = n_{\rm c}(t)$, $z_{g,k} = z_{g,k}(t)$, and it should be satisfied at any point in time during the floating as well before its onset. Thus, the above represents the condition for the floating to ensue or for the resonance to break before the complete transfer of population. We find that these results agree with the simplified limits that we discussed in Ch. 5 and Ref. [1], as well as with Ref. [154], where applicable.[II] In particular, for early resonances with eccentricity starting out below the fixed point, $e_{\rm in} < e_{\rm cr}$, if the condition is fulfilled for floating to start, growth of $z_{g,k} \sim e^{2|k|}$ will tend to decrease the threshold for the occupation of the cloud and thus make the resonance self-sustaining. On the other hand, the decrease of eccentricity that happens for late overtones would increase the critical threshold $n_{\rm c}^{\rm (cr)}$, and could lead to resonance breaking.

If the decay of the cloud is slow with respect to floating, one finds from Eq. (8.13) and Eq. (8.3)

$$\sigma_{\rm fl} \simeq 1 - \left(\frac{n_{\rm c}}{n_{\rm c}^{\rm sat}}\right)\frac{2t}{|g|b_{g,k}} , \tag{8.15}$$

and the maximal floating timescale is given by $\tau_{\rm fl} \equiv |\Delta m|b_{g,k}$. This analytically confirms the typical

[II] An exception being the scaling with $z_{g,k}$ in the vanilla floating condition in [154].

linear population transfer during floating. As already discussed in Ch. 5, an efficient floating requires the transition not be overly adiabatic. Because even for $z_{g,k} \gg v_{g,k}$, if $z_{g,k}$ is too large, this would lead to prolonging and smoothing of the mixing, suppressing $\dot{\sigma}$ and, via Eq. (8.3) and Eq. (8.10), weakening the counter-balance to radiation reaction. By comparing the linear LZ-timescale in the weak-decay regime with the efficient floating timescale one can find a complementary condition to Eq. (8.14) that determines if the floating can be efficient

$$b_{g,k} \gtrsim 4\sqrt{z_{g,k}}/|g| \,. \tag{8.16}$$

Unbound eccentricity growth on counter-rotating orbits. It has been claimed so far in the literature that binaries formed close to the counter-rotating configuration will necessarily survive the $\mathcal{H}/\mathcal{F}$ resonances and reach the $\mathcal{B}$ regime [154], as all transitions are of the floating type $\Delta\epsilon < 0$ with $\Delta m < 0$. Thus for $g > 0$ overtones (including $g = -\Delta m$), which have support around $\iota = 0$, the resonance can happen for low inclination orbits, including co-rotating ones, while the $g = \Delta m$ overtone, which has support around $\iota = \pi$ does not fulfill the resonant condition. However, it was missed that this is only true for $k = 0$. The resonance condition $(g-k)\Omega_0 = -\Delta\epsilon$ can be satisfied for $|k| > |g|$ even when $g < 0$. In other words, depending on a particular transition, sufficiently eccentric orbits can excite negative overtones. That means at least a subset of binaries on counter-rotating orbits will experience $\mathcal{H}/\mathcal{F}$ resonances. For co-rotating orbits, we already studied the behavior of fixed points in eccentricity from Eq. (8.12). However, on counter-rotating floating orbits we can only have $g = \Delta m$, and hence from Eq. (8.12) it follows all overtones would lead to the growth of eccentricity if floating is initiated by an overtone that flips the sign of $(g-k)$. This growth is in principle unbounded, although the floating assumption, as well as the whole orbital averaging giving rise to Peter's evolution equations, break down as $e \to 1$.

To be concrete, let us consider an $l = 3$ driven $\mathcal{F}$ transition similar to $|322\rangle \to |311\rangle$. This resonance is possible at $\iota = \pi$ for $k \leqslant -2$. The leading overtone $k = -2$ occurs at $\mathfrak{f}_{-2} = 1$, the same frequency as the main resonance on the co-rotating orbit, and, if the floating is successful, leads to the eccentricity increase (see Eq. (8.12)) and the cloud decay. We illustrate this behavior for simplified values in Fig. 8.2.

8.2.2.2 Mixing Dynamics: Inclined Orbits

In the previous section we have summarized results we partly discussed before, but in a more coherent and straightforward way. We are now turning to the case of general, i.e., misaligned orbits, which has not been addressed properly in the literature. In most general cases, the problem gets much more complicated to track as in the equatorial case. The Eqns. (7.13) to (7.18) describe the change of orbital parameters under influence of a perturbing Hamiltonian $H_{\rm I}$ with respect to a fixed frame. However, for equatorial orbits, it is okay to use the spin frame of the gravitational atom as the fixed frame, because only a, e, and possibly χ will change, but the dynamics are restricted to two dimensions. If now the orbit changes also inclination and precession, this change will necessarily back react onto the gravitational atom, and the orientation of its spin frame with

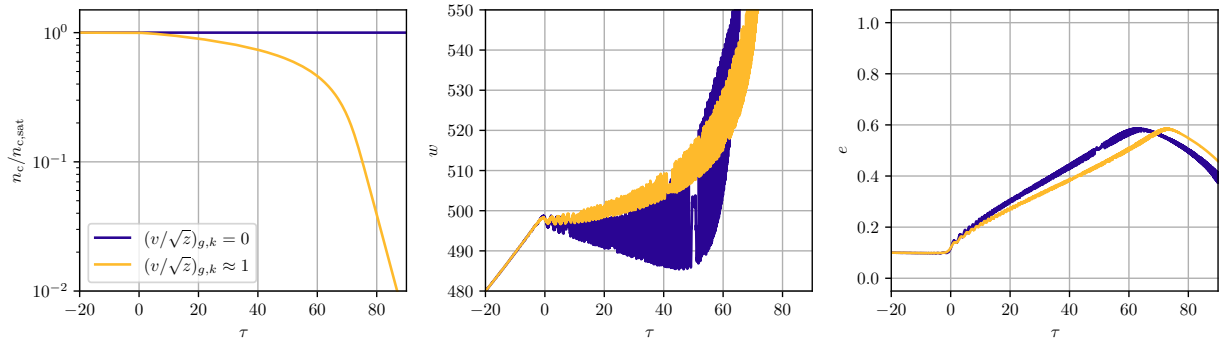

FIG. 8.2: $n_c/n_{c,sat}$ (left), orbital frequency w (center) and eccentricity e (right) for a $\Delta m = -1$, $g = -1$, $k = -2$ resonance on a counter-rotating orbit ($\iota = \pi$). While this is an overtone, the resonance is not "early", but happens at w_0. The growth of eccentricity is in principle unbounded, but the system begins to become unstable for $e \gtrsim 0.6$. Violet shows the resonance for zero decay rate of the second state, which, modulo the heavy oscillations, yields floating at the resonance frequency. The yellow curve shows a resonance to a decaying state with $(v/\sqrt{z})_{g,k} \approx 1$. It shows the same strong growth of eccentricity, while the cloud is lost.

respect to the fixed reference frame will change, in turn changing the overlap of the states due to the orbital companion. We remind the reader of the Euler angles between $\hat{\boldsymbol{n}}$ and $\boldsymbol{L}$ (Υ, ι, χ), between $\hat{\boldsymbol{n}}$ and $\boldsymbol{S}_c$ $(\Upsilon_S, \iota_S, \chi_S)$ and between $\hat{\boldsymbol{L}}$ and $\boldsymbol{L}$ (κ, β, ξ). To proceed further, let us consider two limits:

$|\boldsymbol{S}_{GA}| \gg |\boldsymbol{L}|$ **regime:** allowing us to assume that $\boldsymbol{n} \approx \hat{\boldsymbol{S}}$ $(\iota_S \to 0)$. One can thus relate the Euler angles

$$\chi \approx \xi + \chi_S + \Upsilon_S\,, \quad \iota \approx \beta\,, \quad \Upsilon \approx \kappa\,. \tag{8.17}$$

As $\boldsymbol{n}$ and $\hat{\boldsymbol{S}}$ are nearly parallel, the angles $\{\chi_S, \Upsilon_S\}$ become degenerate and we can thus take $\xi \approx \chi - \chi_S$. We already wrote down the general form of the flow of the principle elements in Eq. (7.47)-Eq. (7.49).

$|\boldsymbol{L}| \gg |\boldsymbol{S}_{GA}|$ **regime:** Here instead we take $\boldsymbol{n} \approx \hat{\boldsymbol{L}}$ $(\iota \to 0)$, restricting the orbital configuration space to the equatorial plane and thus tracking only $\mathbb{E}\backslash\{\Upsilon, \iota\}$ in the orbital sector, complemented by the dynamics of the Euler angles describing the spin. Similarly to the Eq. (8.17) one can find[III]

$$\begin{aligned} \chi &\approx \operatorname{atan2}\left(-\cos(\Upsilon_S)\sin(\iota_S), \sin(\Upsilon_S)\sin(\iota_S)\right)\,, \quad \iota \approx \iota_S\,, \\ \Upsilon &\approx \operatorname{atan2}\left(-\cos(\chi_L + \Upsilon_L - \chi_S)\sin(\iota_S), -\sin(\chi + \Upsilon - \chi_S)\sin(\iota_S)\right)\,, \end{aligned} \tag{8.18}$$

again finding the expected degeneracy of $\{\chi, \Upsilon\}$, thus taking $\Upsilon \to 0$ and suppressing the indices on $\{\iota, \Upsilon\}$. The flow of $\{a, e\}$ is the same as in Eq. (7.47)-Eq. (7.48). Assuming that $\hat{\boldsymbol{L}}$ is now fixed, while we understand Eq. (7.49) to describe the negative change of the inclination of the

[III] Where $\operatorname{atan2}(y, x) \equiv \arg(x + iy)$.

gravitational atom, the $\boldsymbol{L}\cdot\hat{\boldsymbol{S}}_{\rm GA}$ angle, and its evolution can be written as (from Eq. (A.1))

$$\left.\frac{d\cos\iota}{dt}\right|^{l}_{g,k} = \frac{N_{\rm c}}{S_{\rm c}}\left(m\cos\iota - g\right)\eta_{g,k}\nu\,, \tag{8.19}$$

$$S_{\rm c} = N_{\rm c}\left(m_a + m\frac{\sigma-1}{2}\right)\,. \tag{8.20}$$

We will now focus on particular novel phenomena that occur away from the equatorial orbit, and in this way also probe the self-consistency of the equatorial assumption that we discussed in the previous section.

Inclination evolution during floating. To understand the eccentricity evolution during floating in Eq. (8.12), we "integrated out" the cloud phase subspace by using the floating condition $\dot{\Omega}=0$ and substituted the terms containing $b_{g,k}$. We can obtain a similar equation for the inclination evolution from Eq. (7.49):

$$\left.\frac{d\iota}{dt}\right|_{\rm fl} = \frac{2}{3}\mathfrak{f}^{8/3}\frac{\gamma_0}{\Omega_0}f(e)\frac{1}{\sin\iota\sqrt{1-e^2}}\frac{g\cos\iota - m}{2(g-k)}\,. \tag{8.21}$$

When we compare that to Eq. (8.12), we see that the dynamics of $de^2/d\iota$ becomes independent of γ_0/Ω_0 and depends only on the specifics of the (g,k) overtone. We already have shown the gradient evolution following from Eq. (8.12) and Eq. (8.21) in Fig. 7.2 for contrast with the result derived by ignoring the impact of the orbital angular momentum precession in Ref. [154]. In particular, one finds that looking at the individual g-terms, there exists a fixed point in the flow of inclination only for $\iota\to 0$, for $g>0$. For counter-rotating orbits, $\iota=\pi$ for $g<0$ is an unstable fixed point. However, the interplay of several terms in the g-expansion can modify that behavior, as we will discuss below.

In the $e\ll 1$ limit one can solve for the evolution of inclination during floating, which is then given by

$$\cos(\iota) \simeq \frac{m}{g}\left[1+\mathrm{e}^{-\frac{g}{3(g-k)w_0}\frac{\mathfrak{f}_k^{3/8}f(e)\tau}{\sqrt{1-e^2}}}\left(\frac{g}{m}\cos\iota_0 - 1\right)\right]\,, \tag{8.22}$$

where ι_0 is the initial inclination. In the case of both $\{e,\iota\}$, assuming a successful vanilla floating, the parameter $C\simeq\gamma_0/\Omega_0$ controls for the actual change in $\{e,\iota\}$ as was already recognized in Ch. 5 and Ref. [154]. We have confirmed Eq. (8.22) by comparison with numerical simulations.

Overtone overlap. In the equatorial regime there is only one very specific case where an *overlap* of overtones, i.e., several overtones happening at the same time, can occur. This is in the $\mathcal{H}$ regime where all possible $k=0$ resonances for different l occur at the same frequency. However, for these there is a strong hierarchy by virtue of the multipole expansion. For different k, even these overtones happen at different frequencies. Unless by coincidence, there cannot be any other overlap of resonances.

For inclined orbits however, the interplay of inclined and eccentric overtones, determined by g and k, respectively, can more generically lead to an overtone overlap, without a clear or strong

hierarchy between them. Explicitly, consider two overtones (g, k) and (g', k') of the same main resonance Ω_0. They will lead to the resonance at the same frequency when $g - g' = k - k'$ (see Eq. (8.1)). For example, let us take a transition where $\Delta\epsilon < 0$, $\Delta m = -2$ (which is typical for $\mathcal{H}$ and $\mathcal{F}$ transitions). For general inclinations one find in this case a simultaneous occurrence of four overtones: $(g, k) = \{(2, 1), (1, 0), (-1, -2), (-2, -3)\}$, which would happen at $\mathfrak{f}_k = 2$. Going to the vicinity of co- and counter-rotating orbits, $\iota_{\rm in} \to \{0, \pi\}$, where $\iota_{\rm in}$ is the inclination away from the resonance, only the leftmost and the rightmost overtones will have support, in respective order. However, for general inclination, all four corresponding Wigner matrices will be non-zero. One can similarly expect that for $0 < \iota < \pi/2$, and $e \ll 1$, the main overtone $(1, 0)$ will dominate. However, apriori, it is not clear how the transition will play out when $\pi/2 < \iota < \pi$ as there is an interplay of the ι-suppressed $g > 0$ overtones and the e-suppressed $g < 0$ overtones. Here, for the first time, the relative sign of the $\eta_{g,k}$ become important. Because of that, the full effect of single overtones is *not* identical with the sum of their individual effects. If only one $\eta_{g,k}$ overtone is active, the sign of it does not matter, as the vanilla LZ-transition is only characterized by $z_{g,k}$. But when several overtones act at the same time, the dynamics is determined by the sum of their individual effects *including* their sign. This can lead to the effect that the $g < 0$ and $g > 0$ overtone act together to make π a fixed point of inclination evolution. Note further that these four overtones pull towards different eccentricity fixed points: $g > 0$ overtones pull toward $e \to 0$, while $g < 0$ overtones pull toward $e \to 1$. We show an exemplary behavior of a different example of such an overtone overlap, for a $\Delta m = -1$ resonance, in Fig. 8.3.

An even more subtle and previously unexplored phenomenon is when *one* g-term provides the resonance, but the dynamics are determined by another g-term. Close to $\iota \to \pi$ it can be possible that the counter-rotating overtone $g < 0$ is too weak by itself to trigger a resonance, e.g., because the eccentricity is too small. However, if the $g > 0$ inclination-suppressed overtone is still strong enough, it can trigger a resonance. This activates not only the dynamics governed by that overtone, but also the dynamical equations of $g < 0$ which is now "externally forced" to also resonate. We show a numerical example of this in Fig. 8.4. This interplay during overtone overlap would be completely missed by considering only individual g-terms in the inclination expansion.[IV]

8.3 Superradiant Evolution in Isolation

The "vanilla" model of superradiance evolution[V] that ignores any effects of accretion and a companion, for $\alpha < 1$, is a two-step adiabatic process, where first the superradiance grows the cloud until it saturates, and subsequently, the saturated cloud emits GWs [37, 88, 164]. Let us denote the BH mass before the start of the n-th cycle as M_{n-1} and the corresponding fine-structure constant as $\alpha_{n-1} = \mu M_{n-1}$. This means, the first cycle where $|211\rangle$ grows starts with M_0 and α_0. For stellar-mass BHs and $\alpha_{n-1} \lesssim 0.1$, most of the angular momentum of the gravitational atom

[IV] Consequently, it also renders discussions about flow of single g-terms in the (e, ι)-plane that we showed for demonstrative purpose in Fig. 7.2 questionable in at least part of the parameter space.

[V] We refer for a dark matter-based mechanism to generate clouds around compact objects to Ref. [197].

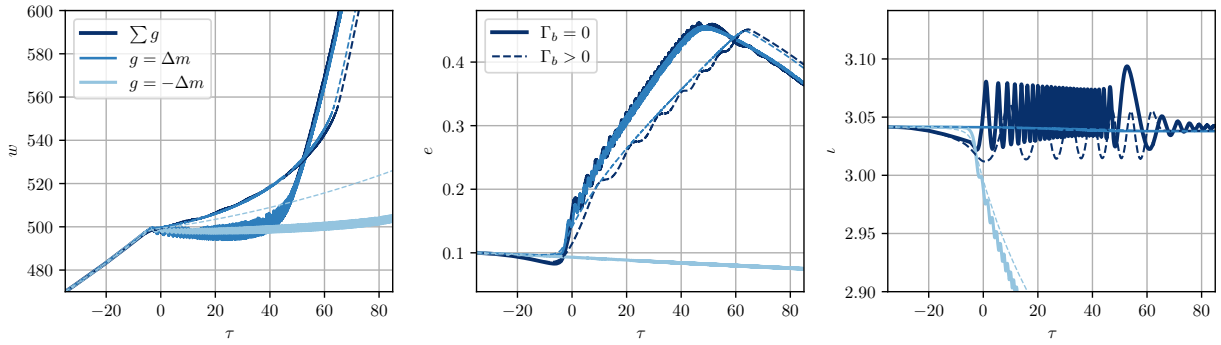

FIG. 8.3: Orbital frequency w (left), eccentricity e (center) and inclination ι (right) for a floating orbit resonance at an almost counter rotating orbit at $\iota_0 = \pi - 0.1$. We choose $\Delta m = -1$ and $l_\star = 3$. The dark blue lines show the full result, summing all g-terms in the inclination expansion, while the medium (light) blue line shows the individual evolution of the term $g = \Delta m$ ($g = -\Delta m$) which has the strongest support at $\iota = \pi$ ($\iota = 0$). The resonance for $g = \Delta m$ is technically a $k = -2$ overtone. Both active g-terms individually lower inclination (while $g = \Delta m$ does it too weakly to be visible in the plot). However, the relative sign of their corresponding η's leads to a stabilization of inclination (including some oscillations around the initial value), as can be seen in the unexpanded evolution in dark blue. The solid lines are for a transition where $\Gamma_b = 0$, while the dashed lines show results for Γ_b in the small-decay regime.

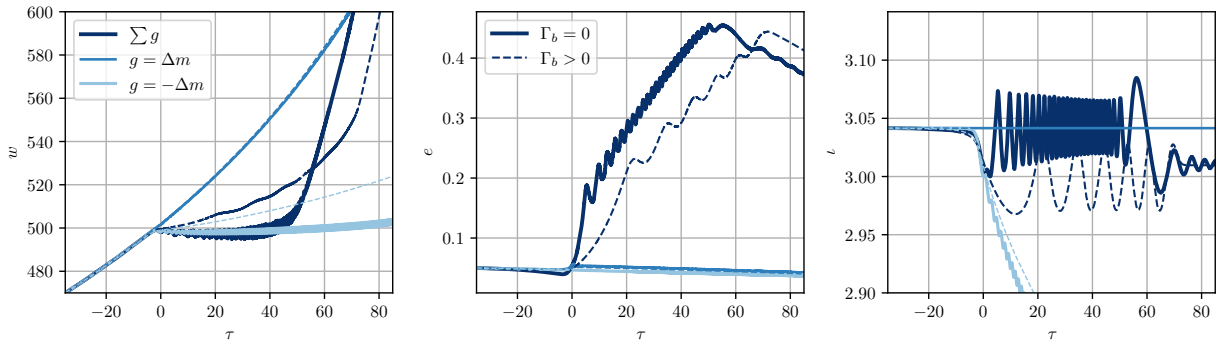

FIG. 8.4: Similar to Fig. 8.3, but with a smaller initial eccentricity. For these choices of parameters, the individual $g = \Delta m$, in medium blue, resonance is not triggered, because the overtone is too strongly suppressed by eccentricity. However, the full evolution in dark blue shows, that the eccentricity still grows. This is because the $g = -\Delta m$, in light blue, provides the resonance and initiates floating, while the $g = \Delta m$ terms provides the dynamics. This shows unmistakably that for general inclined orbits the full dynamics are not necessarily the "sum" of the dynamics resulting from individual terms of the inclination expansion.

is transferred to the $|211\rangle$ cloud, while for larger α_{n-1}, the cloud efficiently decays into GWs due to axion annihilation [88, 117, 120, 164, 165], and the two-step process of growth and decay of higher-m states $\{|322\rangle, |433\rangle, ...\}$ on astrophysical timescales ensues, again depleting the BH spin efficiently [37, 88]. As long as this evolution is adiabatic, i.e., $\Delta\epsilon > \max\{\Gamma, \Gamma_{\rm GW}\}$, where $\Delta\epsilon$ is a typical state split and $\Gamma_{\rm GW}$ is the rate of the cloud decay in GW, one can use the hydrogenic description with the background BH parameters slowly changing. An initially highly spinning BH, $\tilde{a}_{n-1} \lesssim 1$, deposits its angular momentum into the scalar cloud until the superradiant condition stops being fulfilled:[VI]

$$\tilde{a}_{{\rm sat},n} = \frac{4m_n\alpha_{{\rm sat},n}}{m_n^2 + 4\alpha_{{\rm sat},n}^2} < \tilde{a}_{n-1}\,, \tag{8.23}$$

where the index sat, n denotes the value when the n-th cycle has saturated, and m_n is the azimuthal quantum number of the growing state of the n-th cycle. To find the parameters of the gravitational atom at the superradiance saturation in each cycle, we can ignore the effect of the GW depletion. Since $M_{{\rm c},n} = \alpha_{n-1} n_{{\rm c,sat},n}$ we can use this to write α and $\tilde{a}$ at saturation as

$$\alpha_{{\rm sat},n} = \alpha_{n-1}(1 - \alpha_{n-1} n_{{\rm c,sat},n})\,, \tag{8.24}$$

$$\tilde{a}_{{\rm sat},n} = \frac{\tilde{a}_{n-1} - m_n n_{{\rm c,sat},n}}{(1 - \alpha_{n-1} n_{{\rm c,sat},n})^2}\,. \tag{8.25}$$

Together with Eq. (8.23) one can close the (algebraic) system, solving for $(n_{\rm c}, \alpha, \tilde{a})|_{\rm sat}$, given the parameter values at the onset of the n-th SR cycle, as it has also been done in Ref. [89]. To leading order in α_{n-1}, $n_{{\rm c,sat},n} \simeq (\tilde{a}_{n-1} - \tilde{a}_{{\rm sat},n})/m_n$. We show in Fig. 8.5 the resulting cloud masses for $|211\rangle$ and $|322\rangle$ states, together with results from more simple estimates. Note that the SR cloud $M_{\rm c} \simeq \mu N_{\rm c}$ can carry at most 11% of the original BH mass in the vanilla scenario Ref. [109].

It also follows that for small-to-moderate eccentricities $e \lesssim 1$ and $\alpha \ll 1$ one finds (for $m_a = 1, 2$),

$$\frac{L}{S} \simeq \frac{q\alpha^{-p/3-(m_n-1)}}{(1+q)^{1/3} 2^{2(m_n-1)}}\,, \tag{8.26}$$

i.e., for $q \gtrsim 10^{-1}$ ($\mathcal{B}$ regime) and $q \gtrsim 10^{-2}$ ($\mathcal{H}$), we have $L \gtrsim S$.

8.4 Non-Resonant Mixing: Integrating Out the Cloud

This section treats non-resonant decay to strongly decaying states. In the presence of the companion, the dominant state technically mixes with other states with non-zero overlap all the time, but this will not built up a significant occupation of the second state off the resonance due to the fast oscillations in the overlap. However, for decaying states, even these oscillations will induce a transition. While for orbits on which the conditions for a LZ-resonance are fulfilled, these *non-resonant* transitions can be understood as very wide LZ-transitions, such perturbative mixing is

[VI] This saturation condition arises when setting $\omega = \mu$ in the superradiance condition. Ignoring the $\mathcal{O}(\alpha^2)$ corrections in the bound state energy provides a good approximation of the SR saturation [198].

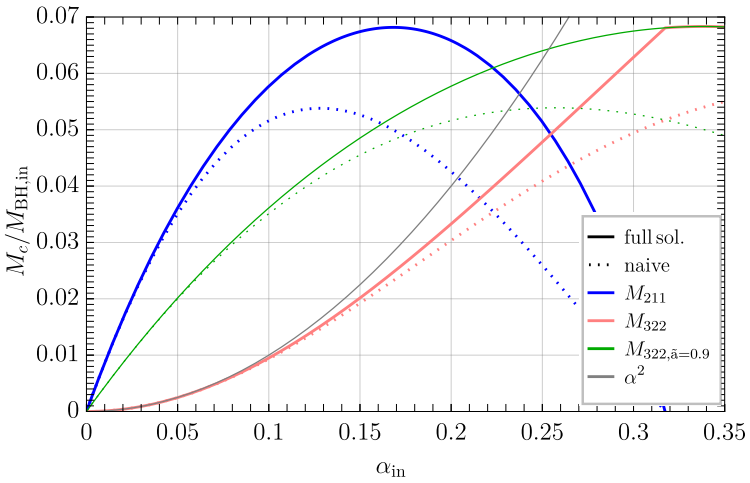

FIG. 8.5: Final cloud mass in relation to the initial BH mass for different values of the initial α before any superradiant instability happens, here denoted with the index "in". Solid lines show the calculation described in the text, while dashed lines show the solution if α is assumed to fixed. The blue lines shows $|211\rangle$, the red line shows $|322\rangle$ after $|211\rangle$ vanished, the green line shows $|322\rangle$ assuming $|211\rangle$ never extracted mass and spin. For reference, we also show α^2. All curves assume $\tilde{a}_0 = 0.9$.

possible even if the condition for the resonance cannot be satisfied, but $\Gamma_b > 0$, for example on a counter-rotating orbit for a transition that has a resonance on the co-rotating orbit. This is due to the fact that the mixing terms between the states oscillate, and even if the resonance condition is never fulfilled, these oscillations "dip" into the decaying state at every oscillation, reducing the cloud little by little.

Spherical states ($l = 0$) have a large decay widths due to $\Gamma \sim \alpha^{4l+5}$, leading to the cloud decay much before the resonant transition. There are two scenarios phenomenologically relevant in this context that we will consider in turn - non-resonant mixing with the spherical states $|c\rangle$ far from the resonance; and with a simultaneous resonance $|a\rangle \to |b\rangle$, where $\Gamma_c \gg \Gamma_b \gg |\Gamma_a|$.

There is an alternative description of the cloud sector to the phase-space representation using (σ, δ) which is useful for both analytic understanding as well as numerics and is given by the Feynman-Vernon-Hellwarth representation [199–201]. Let us set the stage by considering a two-level system, with $\Gamma_a, \Gamma_b \neq 0$ (Sec. 7.3.2,8.2) and focusing on the impact of only one overtone. The phase-space dynamics of the cloud takes place on the unit ("Bloch") sphere spanned by $\{u, \nu, \sigma\}$, where the variables $\{|u| \leqslant 1, |\nu| \leqslant 1\}$ have been defined in Eq. (7.43)-Eq. (7.44), and their dynamics is given by

$$\left.\frac{du}{dt}\right|^{lm}_{g,k} = \bar{\Gamma}^{-}_{ab} u\sigma - \nu\left(\Delta\epsilon + \dot{\Sigma}_{g,k}\right) , \tag{8.27}$$

$$\left.\frac{d\nu}{dt}\right|^{lm}_{g,k} = \sigma(2\eta_{g,k} + \bar{\Gamma}^{-}_{ab}\nu) + u\left(\Delta\epsilon + \dot{\Sigma}_{g,k}\right) . \tag{8.28}$$

Although the full cloud description requires knowing the $n_{\rm c}(t)$, in the limit when $|\Gamma_{\rm GW}| \ll |\Gamma_{a,b}|$, the dynamics on the Bloch sphere only implicitly depends on $n_{\rm c}(t)$ via orbital parameters and α. In

the regime where the decay of the state $|b\rangle$ is strong, σ will stay close to unity, because any particles transitioning into this state will immediately decay into the BH and keep the relative occupation of $|b\rangle$ near zero. Hence, in this *perturbative mixing* regime, $|\sigma - 1| \ll 1$, and we can "integrate out" the dynamics on the Bloch sphere.

First, we use Eq. (8.3) and Eq. (8.28) to express ν and u in terms of σ and it's derivatives[VII]

$$\nu = -\frac{\bar{\Gamma}^{-}_{ab} - \bar{\Gamma}^{-}_{ab}\sigma^2 + \dot{\sigma}}{2\eta_{g,k}}\,, \tag{8.29}$$

$$u = \frac{-1}{\Delta_{g,k}}\left(2\eta_{g,k}\sigma + \bar{\Gamma}^{-}_{ab}\nu - \dot{\nu}\right)\,, \tag{8.30}$$

$$\Delta_{g,k} \equiv \Delta\epsilon + \dot{\Sigma}_{g,k}\,. \tag{8.31}$$

Now we consider a perturbative expansion $\sigma = 1 + \varepsilon F$, where $\varepsilon \ll 1$ is a bookkeeping parameter. Expanding the constraint $u^2 + \nu^2 = 1 - \sigma^2$, one can solve for F algebraically and in turn obtain the leading-order behavior of u and ν as

$$F = \frac{2\eta^2_{g,k}}{\Delta^2_{g,k} + (\bar{\Gamma}^{-}_{ab})^2}\,, \quad \nu = \frac{-2\bar{\Gamma}^{-}_{ab}\eta_{g,k}}{\Delta^2_{g,k} + (\bar{\Gamma}^{-}_{ab})^2}\,, \quad u = \frac{-2\Delta_{g,k}\eta_{g,k}}{\Delta^2_{g,k} + (\bar{\Gamma}^{-}_{ab})^2}\,. \tag{8.32}$$

This result agrees with the $\varepsilon \to 0$ asymptotic solution of the "adiabatic following" approximation employed in Ref. [166]. In the regime of validity of the perturbative mixing we partially integrated out the cloud sector and need to solve only for $\{n_c, \alpha, \tilde{a}\}$. In the resulting equations there is no dependence on any of the anomalies left,[VIII] which in the other formalism forces us to solve the problem in the time-domain. Hence, the remaining equations, including Lagrange's equations for the orbital parameters, can be solved in frequency space, which makes it much easier to track the evolution numerically over a large frequency range. From Eq. (8.32) it follows that such an approximation is applicable as long as $\sqrt{\Delta^2_{g,k} + (\bar{\Gamma}^{-}_{ab})^2} \gg \eta_{g,k}$.

These wide resonances can complete the mixing even before $\mathfrak{f}_{g,k}$ is reached i.e., in the *perturbative* regime. In such a case, the decay rate is so strong that the cloud is completely lost before $\mathfrak{f}_{g,k}$ is reached. Some of the previous limits can be understood from the perturbative mixing developed in Eq. (8.32). At the resonance $\Delta_{g,k} = 0$, the perturbative mixing condition reduces to the requirement of the strong-decay regime $v_{g,k} > \sqrt{z_{g,k}}$. In that case, as $\sigma \simeq 1$, the instantaneous state of the cloud is described by $|a\rangle$, but the cloud decay, via $|b\rangle$, can be resonantly enhanced. In contrast, in the weak-decay regime, perturbative results can be applied only in the early stage of the mixing, e.g., to set the appropriate initial conditions for the full numerical evolution at the resonance.

8.5 Phenomenological Prospects

In the last two chapters, we have developed an extended tool-set to understand the inspiral history of a gravitational atom and its companion. While having discussed the most important aspects of

[VII] In fact, one can also formulate the whole system as a third-order equation in σ, cf. Ref. [200].

[VIII] Neglecting the dependence of $\eta_{g,k}$ on anomalies.

the dynamics arising from a full treatment of all orbital parameters, applying this knowledge to fully realistic cases remains challenging. The small eccentricity expansion breaks down when eccentricity grows too much at an early overtone resonance, which imposes challenges even for equatorial orbits. For inclined orbits, the expansion in different inclination overtones works only in a domain where a single term dominates strongly, while important aspects are missed by that. Therefore, for generally inclined orbits, one is forced to use non-expanded equations (either expanded in eccentricity or not). To numerically solve the full equations, without the expansion in eccentricity and including all the terms in the inclination expansion, is computationally expensive. The non-resonant decay to spherical states can be treated far away from the resonance in the frequency domain, but that cannot incorporate any resonance effects; neither with the spherical state itself, nor with any other state.

For phenomenological purposes, the most important aim is to find out until when the cloud survives, and what the orbital parameters, impacted by level mixing, are after it vanished. As the resonance $\Omega_{g,k}$ leads to the most dramatic consequences for gravitation atom-orbit co-evolution, we are interested in answering two questions:

1. Assuming the birth of the cloud at the superradiance-saturated n-th cycle at $f_{\rm GW}^{(n)}$, where f is a GW (peak) frequency, $f_{\rm GW} \simeq \frac{\Omega}{\pi}(1+e)^{1.1954}/(1-e^2)^{3/2}$ [170], does the cloud survive up until $\lesssim f_{\rm GW}(\Omega_{g,k})$? If not, how does the orbital evolution differ from vacuum evolution?

2. If the cloud has survived until being close to the resonance, will the resonance lead to a strong impact on the orbital evolution? Such an impact can either be observed if $f_{\rm GW}(\Omega_{g,k})$ is in the band or lead to the distortion of the orbital parameter distribution for a BH sub-population. Finally, does the cloud survive, either in the original $|a\rangle$ state or the target state $|b\rangle$? If so, one can ask the same questions again for the following resonant overtone.

To leading order, the answer to these questions depends on $\mathrm{sgn}(\Delta\epsilon)$, i.e., the direction of the energy-momentum flow between the gravitational atom and the orbit, and the dimensionless parameters $\{z_{g,k}, b_{g,k}, v_{g,k}, w_{g,k}\}$. To answer the first question, in principle we need to integrate over several decades in frequency, whereas for the second question, the dynamics takes place in the vicinity of $w_{g,k}$. Performing numerical orbital evolution in time over decades in frequency is challenging even in the vacuum case. Simplifying the equations from Sec. 8.4, we find as rough analytic estimate the following matrix that roughly controls whether the cloud survives up to $\mathfrak{f}_{\rm res}$.

	$v_0 \gg w_0$	$v_0 \ll w_0$
$\sqrt{z_0} \ll \min[v_0, w_0]$	$\frac{3}{2}\frac{z_0 w_0}{v_0} \lesssim 1$	$\pi z_0/\lvert g\rvert \lesssim 1$
$\sqrt{z_0} \gg \max[v_0, w_0]$	$1.8\left(\frac{w_0^3 z_0^2}{v_0}\right)^{1/3} \lesssim 1$	$1.8\left(\frac{v_0^3 z_0^2}{w_0 g^4}\right)^{1/3} \lesssim 1$

If the answer to the first question is positive, the cloud does not impact the orbital evolution prior to the resonance. If the cloud seems to decay already far from the resonance, one can use the formalism from Sec. 8.4 to solve the evolution in frequency space numerically and find the impact on orbital parameters.

If the cloud survives until the resonance, the conditions Eq. (8.14) and Eq. (8.16), now dependent on $\{z_{g,k}, v_{g,k}, b_{g,k}\}$, which determine how efficient the floating will be and thus how strong the orbital backreaction to the level mixing will be. Violating Eq. (8.14) means that the resonance will not even start or will break before the completion of the mixing. In that case, the cloud may survive in the initial state $|a\rangle$ even after the resonance. If the mixing has completed, the interplay between Γ_b and the time interval to the next overtone dictates the survival of the cloud. On the other hand, violation of Eq. (8.16) will lead to successful level mixing, but the orbital impact will be significantly weaker in comparison to the efficient floating case.

8.5.1 Imprints of Eccentricity in Light of Non-Resonant Mixing

We will discuss in light of the new results the study done in Ref. [1], i.e., Ch. 5 and Ch. 6. The early overtones that can grow eccentricity are a solid prediction of general orbits. They cannot only be found on equatorial orbits, but also for binaries formed dynamical, with misaligned orbits. However, the non-resonant mixing with spherical states, in our case $|300\rangle$, begs the question if these resonances can be reached. For our population study, we assumed $q \geqslant 0.1$. For this region, the mixing with the $|300\rangle$ strongly depletes the $|322\rangle$-state before any $\mathcal{F}$ resonance can be triggered. We study the evolution with the procedure described in Sec. 8.4, integrating the evolution from birth in the frequency domain incorporating the $|322\rangle \to |300\rangle$ non-resonant mixing. The earliest $\mathcal{F}$ resonance we could encounter are of $|31-1\rangle$. We estimate the adiabaticity at each overtone of a $|31-1\rangle$ resonance and stop the solver there if the overtone seems to experience a resonance. Ideally, we would then solve the resonance with $|31-1\rangle$ in the time-domain, but this is computationally expensive; Depending on the parameters, we usually have to integrate over $\Delta\tau \approx 10^3 - 10^4$ with dimensionless frequencies of $w \gtrsim 10^4$. However, since the resonances with $|31-1\rangle$ are also in the strong decay regime, we can also use the solver in the frequency-domain.

In Ref. [1], we have taken the cloud mass to be $M_c/M = \alpha$, with fixed M and α, which as we have shown in Sec. 8.3 is too optimistic for clouds formed in isolation. Let us note that the accretion onto the BH, from a baryonic or a dark matter environment, can lead to higher masses for the cloud, maximally up to 35% of the original BH [109]. It could therefore be justified to study how the excitation of resonances differs when we treat the cloud mass as a "free parameter", without explicitly tracking the evolutionary dynamics of the BH-cloud-environment, as long as the total extraction bound is satisfied. In the following, we will study the evolution with a cloud mass predicted for isolated BHs as in Sec. 8.3.

As final task in this thesis we want to answer the question if a binary formed at $\Omega_{\rm ini}/\pi = 10^{-4}\,\mathrm{Hz}$ already containing a gravitational atom can really experience overtones of fine resonances that grow the eccentricity?[IX] Due to the strong depletion of the cloud through non-resonant mixing when $q \gtrsim 0.1$, we need to go to slightly larger BH masses, but this can still correspond to resonances in the LISA band. We show an exemplarily evolution of such a BBH in Fig. 8.6.

[IX] Following private discussions with the authors of the draft Ref. [202], for these examples we neglect the $\mathcal{H}$ resonances due to self-gravity corrections which seem to swap the energy hierarchy of the $|32m\rangle$ states for small α and therefore make hyperfine transitions on equatorial orbits impossible.

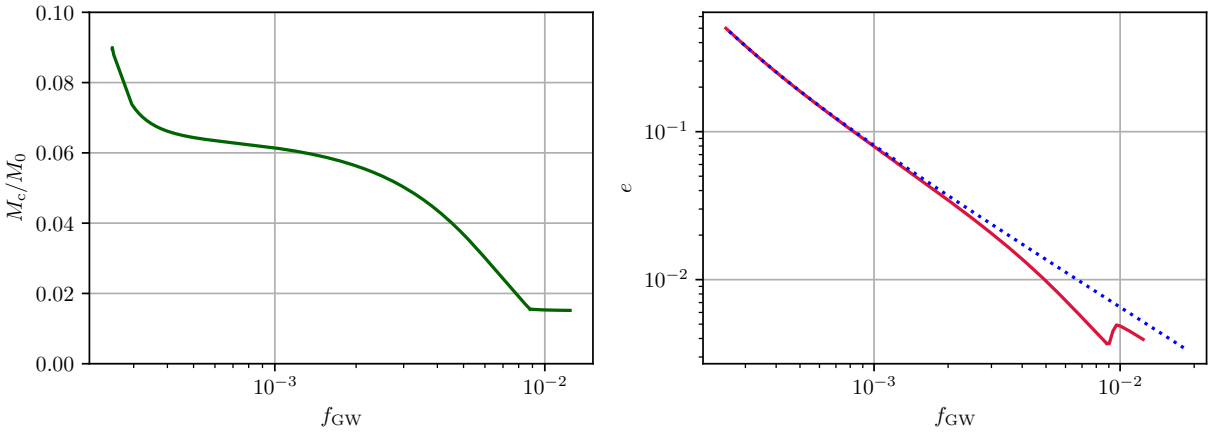

FIG. 8.6: Evolution of a gravitational atom in the $|322\rangle$-state with $M_0 = 50\,M_\odot$ and $\alpha_{\rm sat} = 0.3$ as part of a binary with $q = 0.02$ born at $\Omega_{\rm ini}/\pi = 10^{-4}\,$Hz. These parameters correspond to a boson mass of 2.9×10^{-13} eV. Plotted is peak frequency $f_{\rm GW}$. The initial eccentricity is $e_{\rm ini} = 0.5$ which is the highest initial value of the population studied in Ch. 6. The plot on the left shows the cloud mass over initial BH mass, M_c/M_0, while the right hand side shows eccentricity e. The initial cloud mass is found following Sec. 8.3 and assumes $\tilde{a}_{\rm ini} = 0.99$. One can see that at low frequency, the cloud loses some of its mass due to GW emission, because this small increase in frequency takes the longest time. Later, the non-resonant mixing with $|300\rangle$ kicks in, which reduces eccentricity compared to the evolution in vacuum, the latter shown in dotted blue. At shortly before $f_{\rm GW} = 10^{-2}\,$Hz, right in the center of the LISA band, a $k = -1$ resonance to $|31-1\rangle$ happens, due to the already diminished cloud mass only slightly increasing the eccentricity.

Part IV

Epilogue

Chapter 9 Summary, Conclusions and Outlook

9.1 Summary

In this thesis, we have expanded gravitational atomic physics, referring to BH superradiance in binaries, to include eccentric and inclined orbits. This system was often studied under the premise that the orbits are circular and equatorial. This simplifying assumption makes the dynamics by no means trivial – they contain the most important aspect of gravitational atomic physics, the non-linear Landau-Zener-like transitions between the hydrogenic bound-states, leading to floating and sinking orbits if the backreaction onto the orbit is strong enough. The system also gives rise to transitions to unbound states, a process called ionization. However, the problem reduces the five parameters that define Keplerian orbits of the companion around the gravitational atom to one, the semi-major axis, or equivalently, the orbital frequency. It turned out to be missing several important aspects.

In Part 2 of this thesis, we have shown that abandoning the assumption of circularity leads to a whole new phenomenon: Early and late resonances, far from the main resonance where orbital frequency matches the energy difference of the cloud states. If the energy difference leads to floating orbits, early resonances can grow a small eccentricity, depleted via GW emission during the inspiral, towards a large fixed point. We have found analytical estimates for floating time, eccentricity growth and final cloud population and confirmed with numerical examples in Ch. 5. In all of this, we have incorporated for the first time the decay rate of the states involved in the transition. In Ch. 6, we conducted a semi-analytic population study, using the estimates from Ch. 5 to show how the eccentricity distribution of a population of light mass black holes ($\mathcal{M} \lesssim 10\,M_\odot$) can change drastically when each of the BBHs experiences their individual resonances. We find that these resonances can shift a fraction of the population toward values of $e \gtrsim 10^{-2}$ at $10^{-2}\,\mathrm{Hz}$, which would be readily accessible to further observatories like LISA [7] or planned mid-band [11] and decihertz [12] observatories. The observation of such GW signals would then provide evidence for the existence of an ultralight particle of mass between 5×10^{-13} and 2.5×10^{-12} eV. Similar results as in Ch. 5 and Ch. 6 can be drawn also for neutron star/BH binaries. The presence of

a boson cloud would then again lead to larger-than-expected eccentricities, providing additional evidence for the existence of a new ultralight particle.

Neglecting inclination can be justified for BBHs that were formed in isolation, leading to spins parallel to the angular momentum. To encompass systems formed dynamically or via the common envelope evolution, in Part 3 we have set up a consistent framework to govern the full dynamics of the bosonic cloud and general orbits in a consistent way. From the perspective of the binary companion, the gravitational atom is effectively an object characterized solely by its mass and multipole moments, provided the companion is not inside the cloud. This regime can be accurately described using the worldline Effective Field Theory framework. These multipole moments provide an interacting Hamiltonian that determines the full dynamics of all orbital parameters via Lagrange's planetary equations. The multipole moments of the gravitational atom can be found from the microphysics of the superradiant cloud. Because gravitational atoms are relatively simple objects, we can enlarge our phase space and simultaneously study the coupled dynamics of the orbit as well as the cloud.

We discussed where the balance equation approach used in all literature about superradiance in binaries until now has its limits and which theoretical misconceptions were involved. We illustrated how to obtain the same dynamics by balancing the orbital energy and angular momentum with the energy and spin of the cloud, respectively, in the equatorial case. However, from this approach, it is not straightforward to derive the non-Keplerian flow of χ and ϑ. Among others, it is not clearly known how one could find results from the balance equations in the non-EMRI case or include next-to-leading-order effects like a magnetic quadrupole. Our approach removes the conceptual uncertainties.

We have analyzed the dynamics resulting from Lagrange's equations Eq. (7.13)-Eq. (7.18) in Ch. 8. For equatorial floating resonances, they agreed with the dynamics from the balance equations used in Part 2, while deriving mechanisms for resonance breaking as well as floating timescales became straightforward and was in agreement with the literature. We then discussed the previously overlooked feature that the eccentric overtones also made it possible to experience floating resonances to lower energetic states ($\Delta\epsilon < 0$) on counter-rotating orbits, which were thought to be possible only on co-rotating orbits. Additionally, on counter-rotating orbits, these resonances have no fixed-point feature, meaning that, in principle, their eccentricity can grow without bound. For inclined orbits, we showed that in some parts of the parameter space, the dynamics are enriched due to the appearance of "overlapping resonances", meaning that several terms in the eccentricity and inclination expanded Hamiltonian are active at once. This not only stabilizes orbits near the counter-rotating configuration, but also makes it possible that the orbital companion experiences floating due to the adiabaticity of one term in the expansion, while the eccentricity dynamics are dominated by the backreaction of a different term during the floating.

By describing the cloud with variables on a "Bloch sphere", we were able to integrate out the internal dynamics of the cloud and reduce it to the total occupation number as degree of freedom. This made it possible to study non-resonant mixing with strongly decaying states. This is an effect

on long time scales, and integrating out the cloud degrees of freedom allowed to evolve the system in the frequency-domain. We found that for large relative companion masses $q > 0.1$, the non-resonant mixing makes encountering fine resonances much harder due to the depletion of the cloud state $|322\rangle$ by mixing with $|300\rangle$. For the first time we have also included that mixing with decaying states, that are almost all transitions in gravitational atomic physics, changes the LZ-transition not only by loosing the cloud, but also because the decaying state is fed back into the BH, which changes α and in turn shifts the resonance frequencies during the transition. Consequently, this renders perfect floating to be an idealized effect. However, the imprints on the orbital parameters remain significant.

9.2 Conclusions and Outlook

Recent publications on gravitational atomic physics had a tendency to present their results, typically addressing interesting and previously unexplored aspects, as though they marked the closure of the topic. This thesis takes a different stance: We argue that the field remains full of open questions and opportunities for further exploration.

We developed a consistent tool-set to model the joint dynamics of the gravitational atom and its binary companion. Now it is our task, as well as of the community, to study the resulting phenomenology in more detail and to extend the theoretical framework. To underline our perspective, we outline below a number of open problems, limitations of the work presented in this thesis and possible directions for future research:

- The numerical simulations in the time domain still holds challenges and it would be an important task to speed them up so that realistic parameters can be studied for (hyper)fine transitions, that seem conceptually clean now.

- Contrary to (hyper)fine transitions, Bohr transitions on the other hand happen on short dimensionless timescales, since they are closer to the merger, which would make them easier to study numerically in that regard. However, the expansion Eq. (7.30) does ignore the emission of the scalar to infinity, i.e. the effect of ionization [27, 153, 173]. The latter has thus far been treated using the energy-momentum balance arguments and exclusively in the $q \ll 1$ limit. To study Bohr resonances, this must be included, since it can overcome radiation reaction [154]. Also, inside the cloud, one has to account for the more complicated structure of the overlap of states, which becomes especially involved for eccentric orbits, in which the companion in principle could exit and re-enter the cloud on every orbit.

- The geometry of inclined orbits is complicated and we only showed results for simplified regimes in which either the orbit or the gravitational atom stays (practically) aligned with the reference frame. The intermediate regime would include to track two sets of Euler angles and adjust the overlap accordingly.

- We have assumed that the spin of the central BH and the cloud stay aligned, because the states of the cloud are a solution of the Laplacian in the frame of the BH, so we expect that

the cloud adiabatically adjusts to movement of the BH, and vice versa. However, it is not clear if changes in the spin of one of the constituents of the gravitational atom could be fast enough to break adiabaticity such that cloud and BH get misaligned.

- In this work, we studied leading order effects, but it is straightforward to go further in the worldline EFT approach by systematically including higher-order effects, spin-orbit interaction [192], magnetic multipoles or tidally induced quadrupoles.

- Thus far, most of the literature has focused on superradiance based constraints in connection with stellar-mass and supermassive BHs. However, it is generally expected that a wide distribution of intermediate-mass BHs forms in dynamic environments, that will be probed by LISA and the Einstein Telescope.

- While our results are independent of the question if the bosons in the superradiant cloud make up the universe's dark matter, studies could be extended to clouds formed from ultralight scalar dark matter around the BHs [47, 203, 204].

- In the static limit, self-gravity of the cloud leads to the conservative shift of the energy levels and the scalar wavefunction [89, 205]. Tentative arguments [162, 202] pointing out that the $\mathcal{H}$ (but not $\mathcal{F}$) resonances may be partially or completely disrupted by the self-gravity effects (in parts of the parameter space). However, without a well-defined perturbative framework, one can't access the validity of such statements. Ultimately, this issue may be resolved numerically in the extension of Ref. [205].

- Axion self-interactions will affect both the bound state spectrum as well as the superradiance dynamics of the cloud growth [89, 92, 93]. In order to use superradiance in binaries to probe $f_a \ll M_{\rm Pl}$ range of the axion parameter space, one needs to simultaneously track the dynamics due to the orbital companion and the self-interactions. Although tedious, such a problem is still tractable and solvable in a semi-analytic framework – which would work as a direct "product" of the framework outlined in this work and the one presented in Refs. [89, 92].

- As noted in Ref. [169], if one takes the GW emission of the cloud by itself, this leads to the gravitational atom losing mass and thus tending to outspiral, which can even overcome the RR-driven inspiral in some corners of the parameter space. It would be interesting to study if a hyperfine-resonance could be triggered during the outspiral, which would turn a floating resonance into a resonance that even accelerates the outspiral, and could be called a *breaching orbit*.

- As practical application on the observational side, GW studies could aim to detect the cloud by modeling binary waveforms that incorporate large finite-size effects and quadrupoles [25, 26, 206] or even observables in the pulsar-GA binaries [207]. However for stellar-mass BHs, the one-level atom scenario is not applicable. To take an extreme example, one needs a strong fine-tuning (if possible at all) of the binary-cloud parameters in order for the cloud to survive to the

later binary inspiral stage that LIGO is probing, so that the induced quadrupole deformation (Love numbers) can be used to constraint the bosonic clouds as attempted in Ref. [208].

Appendix A Spin Dynamics

The full resonance condition Eq. (7.32) contains $\dot{\chi}$ and $\dot{\Upsilon}$, which in principle change during the resonance according to Eq. (7.17) and Eq. (7.18) due to the dependence of $H_{\rm I}$ on ι and e. In this appendix, we are going to discuss how spin dynamics given by the worldline EFT approach give rise to precession dynamics, and compare them to the precession dynamics predicted by Lagrange's equations.

The spin dynamics from Eq. (7.20) is given by

$$\begin{aligned} \dot{S}^i{}_{\rm GA} &= \epsilon^{ipq}\sum_{l=1}^{\infty}\frac{M_\star}{l!}Q^{\langle pA\rangle}_{\rm GA}\partial_{\langle qA\rangle}\left(\frac{1}{R_\star}\right), \\ &= \epsilon^{ipq}\sum_{l=2}^{\infty}\frac{M_\star(-1)^l}{R_\star^{l+1}}\sum_{m=-l}^{l}Q^{\rm GA}_{lm}\left[\int d\Omega_{\hat{\boldsymbol{k}}}Y_{lm}(\hat{\boldsymbol{k}})\hat{k}^p\frac{\partial P_l(x)}{\partial x}\Big|_{x=\hat{\boldsymbol{k}}\cdot\hat{\boldsymbol{R}}}\right]\hat{R}^q, \end{aligned} \tag{A.1}$$

where ϵ^{ipq} is the Levi-Civita symbol, P_l is the Legendre polynomial and we skip the details on the derivation of the second line.

A.1 Precession Dynamics

One-level atom. We are going to first discuss the one-level atom setup (Sec. 7.3.2) as it will allow us to analytically understand the role of precession and will generalize in a straightforward manner in the multi-level scenario. Consider the $\boldsymbol{S}$ precession due to the coupling with a Q_{20} (Eq. (7.35)). From Eq. (A.1), one can find, after adiabatic averaging

$$\dot{\boldsymbol{S}} = \boldsymbol{\Omega}_Q \times \boldsymbol{S}_{\rm c}\,, \quad \boldsymbol{\Omega}_Q \equiv \frac{3M_\star}{2a^3\sqrt{1-e^2}^3}\sqrt{\frac{4\pi}{5}}Q_{20}\left(\hat{\boldsymbol{S}}\cdot\hat{\boldsymbol{L}}\right)\frac{\boldsymbol{J}}{LS}\,, \tag{A.2}$$

where $\boldsymbol{J} = \boldsymbol{L} + \boldsymbol{S}$. The only allowable spin dynamics is precession. Radiation reaction makes the system dissipative, $\dot{\boldsymbol{J}} \neq 0$. Let us compare RR and the precession timescales by parameterizing the orbital separation in terms of the "resonances" as a benchmark, i.e. $\Omega \sim \Delta\epsilon$, where $\Delta\epsilon$ is given by Eq. (7.33):

$$\frac{t_{\rm RR}}{t_Q} \sim \frac{\alpha^{(-2p-9)/3}}{(1+q)^{2/3}}\frac{1-e^2}{1+\frac{7}{8}e^2}\,, \quad t_{\rm RR} \equiv L/[\dot{L}]_{\rm RR}\,. \tag{A.3}$$

Thus, on precession timescales one can take $\boldsymbol{J} \approx$ const, generically across the parameter space, which further serves as a constant reference vector for tracking the evolution of the orbit and spin dynamics $\boldsymbol{n} \approx \hat{\boldsymbol{J}}$ (cf. Sec. 7.2.2). From the flux balance of the total angular momentum it follows

$$\dot{\boldsymbol{L}} = \boldsymbol{\Omega}_Q \times \boldsymbol{L} + [\dot{L}]_{\rm RR} \hat{\boldsymbol{L}} \,. \tag{A.4}$$

From Eq. (7.21), one can also find (and orbit average) the quadrupolar potential

$$\langle V_Q \rangle_{20} = \frac{1}{2} \frac{N_{\rm c} \eta_{00}^{(aa|20)}(a)}{\sqrt{1-e^2}^3} \left(2 - 3\sin^2\left[\iota + \angle(\boldsymbol{J},\boldsymbol{S})\right]\right) \,, \tag{A.5}$$

where $\angle(\boldsymbol{J},\boldsymbol{S})$ is the angle between $\boldsymbol{J}$ and $\boldsymbol{S}$. As V_Q depends only on principal elements, only positional elements will exhibit a secular flow.[I] (compare to Eq. (7.13)-Eq. (7.18)). Going back to Eq. (7.31), one finds that $\delta\epsilon_a = \langle V_Q \rangle_{20}$ to leading order in the l-expansion. In other words, in this scenario, tidal deformation acts as a conservative effect that manifests itself as the precession of positional elements in the orbital sector and as energy shift $\delta\epsilon_a$ and wavefunction corrections $\delta\psi_a$ in the cloud sector.[II]

Other conservative PN contributions also lead to the precession of positional elements. Analogously to the estimate in Eq. (A.3), one can show that on timescales of precession induced by the spin-orbit (SO) coupling, one can still take $\boldsymbol{J} \approx$ const [209, 210]. There is an interplay between the (progressive) PN suppression of $V_{\rm 1PN}$, $V_{\rm SO}$, and V_Q, respectively, and the finite-size enhancement of $Q_{\rm c}$ for $\alpha \ll 1$. Again parameterizing $\Omega \sim \Delta\epsilon$:

$$\frac{\langle V_{\rm 1PN} \rangle}{H_{\rm K}} \sim \alpha^{2p/3} \left(\frac{3(1+q)^{2/3}}{\sqrt{1-e^2}} - \frac{15+29q+15q^2}{8(1+q)^{4/3}} \right) \,, \tag{A.6}$$

$$\frac{\langle V_{\rm SO} \rangle}{H_{\rm K}} \sim \alpha^{p} \frac{S\cos\left[\iota + \angle(\boldsymbol{J},\boldsymbol{S})\right]}{\mathcal{M}^2} \frac{(4+3q)}{1+q} \frac{1}{2\,(1-e^2)} \,, \tag{A.7}$$

$$\frac{\langle V_Q \rangle_{20}}{H_{\rm K}} \sim \alpha^{4p/3-3} \frac{n_{\rm c}}{(1+q)^{2/3}} \frac{2 - 3\sin^2\left[\iota + \angle(\boldsymbol{J},\boldsymbol{S})\right]}{2\sqrt{1-e^2}^3} \sqrt{\frac{\pi}{5}} \left[I_r I_\Omega\right]^{(aa|l0)} \,, \tag{A.8}$$

In the $e \ll 1$, $q \lesssim 1$ limit, one finds that in the earlier stages of inspiral, $p = 5, 7$, 1PN precession effects parametrically dominate, respectively, V_Q and $V_{\rm SO}$ contributions, although the separation in α between 1PN and V_Q is small for $p = 5$ regime. Meanwhile, in the later inspiral ($p = 3$), the V_Q contribution will overtake the 1PN effect.

Finally, note that the periastron precession originating from the 1PN potential is always of the same sign, $\dot{\chi}_{\rm 1PN} > 0$, while the signs of $\dot{\chi}_Q$ and $\dot{\chi}_{\rm SO}$ depend on the angular profile of the particular state of the cloud.[III]

[I] e.g. one can check that Eq. (7.18) leads to $\dot{\Upsilon} = \Omega_Q$.

[II] Note also the difference: while in the orbital sector we can track the precession effects non-perturbatively, in the cloud sector we are confined to the regime of validity of time-independent perturbation theory.

[III] As V_Q typically dominates $V_{\rm SO}$, allowing for spin on the companion would lead to a non-trivial difference from the spin-eccentricity interplay in the pure BH-BH scenario [210].

Two-level atom. In addition to the effects considered in Sec. 7.3.2, the $m \neq 0$ terms from Eq. Eq. (7.46) also contribute to the precession of the positional orbital elements. These precession effects influence the position and duration of the resonance as $\Delta\epsilon = -\dot{\Sigma}_{g,k}$, where the non-Keplerian flow of $\dot{\vartheta}$, together with $\{\dot{\chi}, \dot{\Upsilon}\}$, competes with the orbital frequency Ω. Focusing on the apsidal precession as the representative, the relative importance of these effects follows from estimates Eq. (A.6) - Eq. (A.8):

$$\frac{\dot{\chi}}{\Omega}\Big|_{\rm 1PN} \simeq \alpha^{2p/3}\frac{3(1+q)^{2/3}}{1-e^2}\,, \tag{A.9}$$

$$\frac{\dot{\chi}}{\Omega}\Big|_{Q} \simeq \alpha^{4p/3-3}\frac{n_{\rm c}}{(1+q)^{2/3}}\frac{1}{(1-e^2)^3}\sqrt{\frac{\pi}{5}}\sum_m (I_r I_\Omega)_\sigma\,, \tag{A.10}$$

where we ignored the SO contribution, which is always subdominant to the 1PN and V_Q effects (Sec. 7.3.2), and considered the equatorial limit in $\dot{\chi}_Q$ for simplicity. The final term in $\dot{\chi}_Q$ should be calculated for all m multipoles and weighted by the relative occupancies of the states. From the estimate above, it follows that for all resonances in the $\mathcal{H}/\mathcal{F}$ regime, for $q \lesssim 1$ and $e < 1$, this correction is negligible. However, in the $\mathcal{B}$ regime, particularly in the innermost regions, precession effects start influencing the position of the resonance, even more so for highly eccentric orbits.

Projected resonance. Precession effects on inclined orbits can also lead to the novel effect of "projection" of the resonance from one regime to another. Namely, the resonant condition for the $g = 0$ overtone is set by $-m\dot{\Upsilon} = \Delta\epsilon$, but this overtone is triggered at parametrically larger orbital frequencies compared to the other $g \neq 0$ overtones, in order for $\dot{\Upsilon}$ to reach the critical value due to V_Q and $V_{\rm SO}$ interactions. Considering the dominant V_Q contribution to the nodal precession, this roughly allows for triggering $\mathcal{H}$ and $\mathcal{F}$ $g = 0$ overtones in the region between $\mathcal{F}$ and $\mathcal{B}$ transitions.

Appendix B Milanković Equations

Another method to find the equations of motion that only need the cloud's energy, i.e., its averaged Hamiltonian, is using *Milanković equations* [182, 211]. Typically, we are interested in tracking the secular evolution over time scales $\gg 2\pi\Omega^{-1}$. Thus, the Lagrange's equations can be averaged over orbital time-scales. Alternatively, we can orbit-average the non-Keplerian Hamiltonian and use it in the Lagrange's equations [182, 192] as

$$\langle H_{\rm I}\rangle_{2\pi/\Omega} \;=\; \int_0^{2\pi} d\vartheta \frac{H_{\rm I}}{\Omega}\,, \tag{B.1}$$

where we treat $\mathbb{E}\backslash\{\vartheta\}$ in $H_{\rm I}$ as constant on orbital timescales. Successfully orbital averaging of $H_{\rm I}$ automatically implies that $\langle \dot{a}\rangle = 0$ as the dependence on ϑ is lost, see Eq. (7.13). The presence of a frequency higher than Ω will obstruct the orbital averaging. See [193–195, 212] for going beyond the adiabatic approximation for the PN dynamics, especially relevant for $e \lesssim 1$ orbits. For an averaged Hamiltonian, the Milanković equations now allow for the calculation of the fluxes of $\dot{\boldsymbol{e}}$ and $\dot{\boldsymbol{L}}$ from $H_{\rm I} = V_Q$. These equations are

$$\frac{d\boldsymbol{j}}{dt} = -\frac{1}{\Lambda}\left(\boldsymbol{j}\times\frac{\partial}{\partial \boldsymbol{j}}\langle H_{\rm I}\rangle + \boldsymbol{e}\times\frac{\partial}{\partial \boldsymbol{e}}\langle H_{\rm I}\rangle\right)\,, \tag{B.2}$$

$$\frac{d\boldsymbol{e}}{dt} = \frac{1}{\Lambda}\left(\boldsymbol{e}\times\frac{\partial}{\partial \boldsymbol{j}}\langle H_{\rm I}\rangle + \boldsymbol{j}\times\frac{\partial}{\partial \boldsymbol{e}}\langle H_{\rm I}\rangle\right)\,, \tag{B.3}$$

where

$$\boldsymbol{e} = e\begin{pmatrix}\cos\Upsilon\cos\chi - \cos\iota\cos\Upsilon\cos\chi\\ \sin\Upsilon\cos\chi + \cos\iota\cos\Upsilon\sin\chi\\ \sin\iota\sin\chi\end{pmatrix}\,, \tag{B.4}$$

$$\boldsymbol{j} = (1-e^2)^{1/2}\begin{pmatrix}\sin\iota\sin\Upsilon\\ -\sin\iota\sin\Upsilon\\ \sin\iota\end{pmatrix} \tag{B.5}$$

Rewriting Eq. (B.2) in terms of the orbital elements with the help of Eq. (B.4) and simultaneously rewriting the derivatives, gives rise to dynamical equations for orbital elements e, Υ, ι and χ.

Appendix C Numerics

The form of the equations given in Eq. (7.47)-Eq. (7.49), as well as most of the parameter definitions we give assume an expansion in eccentricity overtones $e \ll 1$ using the Jacobi-Anger expansion from Eq. (5.10). This overtone expansion is useful to identify the new tower of resonant transitions and estimate their position and adiabaticity via $\eta_{g,k}$. Floating can lead to the growth of e towards the fixed point $e \simeq 1/2$ even if the pre-resonant eccentricity is small (see Sec. 8.2.2.1 and Ref. [1]), thus invalidating the said approximation. Consequently, we will use the non-expanded form of the mixing sector of V_Q for the numerical results

$$\begin{aligned} V_Q \quad \supset \quad & qM \frac{4\pi}{2l+1} \frac{M_c r_c^l}{R^{l+1}} Y_{lm}\left(\frac{\pi}{2}, 0\right) I_r^{(ba|lm)} I_\Omega^{(ba|lm)} \sqrt{1-\sigma^2} \times \\ & \sum_{g=-l}^{l} d_{mg}^{(l)}(\iota) \cos\left[\delta - (g\varphi_\star + g\chi + m\Upsilon)\right]. \end{aligned} \tag{C.1}$$

The mean anomaly ϑ is unsuitable to describe the orbital dynamics for arbitrary eccentricity, because the true anomaly $\varphi_\star$ that appears in V_q can only be expressed via ϑ in a series expansion in e. To perform calculations with arbitrary eccentricity, we perform the variable change $(\vartheta, e) \to (E, e)$ in the Hamiltonian mechanics approach, where E is the eccentric anomaly, defined via Kepler's equation $\vartheta = E - e \sin E$. This defines a Jacobian $\hat{\mathbb{G}}'$, that is applied to Eq. (7.12), giving a new representation of Lagrange's planetary equations via $\hat{\mathbb{G}}'^{\mathrm{T}} \hat{\mathbb{M}} \hat{\mathbb{G}}'$. The true anomaly $\varphi_\star$ can be expressed in terms of the eccentric anomaly E via trigonometric functions, see Sec. 5.2 for details. This makes it possible to express Eq. (C.1) in terms of E and use this in Lagrange's equations. In this method, all the overtones will be active at once. we verified our results by comparing with numerical as well as analytical results from the k-expanded equations where possible.

For equatorial and counter-rotating orbits, it is sufficient to pick the one term from Eq. (C.1) which has a non-zero Wigner matrix. This makes the computations less computationally expensive. For inclined orbits we will also use the full sum in Eq. (C.1) which can be simplified when l is fixed. However, these simulations remain the most expensive.

We use the `solve_ivp` routine from the *Python*-package *scipy* [213]. As integration method we mostly use *Runge-Kutta-Fehlberg* (RK45). We also made heavy use of the *numpy*-package [214].

Bibliography

[1] Mateja Bošković, Matthias Koschnitzke, and Rafael A. Porto. "Signatures of Ultralight Bosons in the Orbital Eccentricity of Binary Black Holes". In: *Phys. Rev. Lett.* 133.12 (2024), p. 121401. DOI: 10.1103/PhysRevLett.133.121401. arXiv: 2403.02415 [gr-qc].

[2] Aleksandr Chatrchyan et al. "ALP dark matter with non-periodic potentials: parametric resonance, halo formation and gravitational signatures". In: *JCAP* 10 (2023), p. 068. DOI: 10.1088/1475-7516/2023/10/068. arXiv: 2305.03756 [hep-ph].

[3] Shankha Banerjee et al. "Environmental sustainability in basic research: a perspective from HECAP+". In: *JINST* 20 (2025), P03012. DOI: 10.1088/1748-0221/20/03/P03012. arXiv: 2306.02837 [physics.soc-ph].

[4] Günter Sigl. "Astroparticle Physics: Theory and Phenomenology". Atlantis Press, 2017, pp. 295–398,711–752. URL: https://www.springer.com/gp/book/9789462392427.

[5] B. P. Abbott et al. "Observation of Gravitational Waves from a Binary Black Hole Merger". In: *Phys. Rev. Lett.* 116.6 (2016), p. 061102. DOI: 10.1103/PhysRevLett.116.061102. arXiv: 1602.03837 [gr-qc].

[6] R. Abbott et al. "Open Data from the Third Observing Run of LIGO, Virgo, KAGRA, and GEO". In: *Astrophys. J. Suppl.* 267.2 (2023), p. 29. DOI: 10.3847/1538-4365/acdc9f. arXiv: 2302.03676 [gr-qc].

[7] K. G. Arun et al. "New horizons for fundamental physics with LISA". In: *Living Rev. Rel.* 25.1 (2022), p. 4. DOI: 10.1007/s41114-022-00036-9. arXiv: 2205.01597 [gr-qc].

[8] Adrian Abac et al. "The Science of the Einstein Telescope". In: (Mar. 2025). arXiv: 2503.12263 [gr-qc].

[9] Michele Maggiore et al. "Science Case for the Einstein Telescope". In: *JCAP* 03 (2020), p. 050. DOI: 10.1088/1475-7516/2020/03/050. arXiv: 1912.02622 [astro-ph.CO].

[10] David Reitze et al. "Cosmic Explorer: The U.S. Contribution to Gravitational-Wave Astronomy beyond LIGO". In: *Bull. Am. Astron. Soc.* 51.7 (2019), p. 035. arXiv: 1907.04833 [astro-ph.IM].

[11] Sebastian Baum, Zachary Bogorad, and Peter W. Graham. "Gravitational Wave Science in the Mid-Band with Atom Interferometers". In: (Sept. 2023). arXiv: 2309.07952 [gr-qc].

[12] Seiji Kawamura et al. "Current status of space gravitational wave antenna DECIGO and B-DECIGO". In: *PTEP* 2021.5 (2021), 05A105. DOI: 10.1093/ptep/ptab019. arXiv: 2006.13545 [gr-qc].

[13] R. Alves Batista et al. "EuCAPT White Paper: Opportunities and Challenges for Theoretical Astroparticle Physics in the Next Decade". In: (Oct. 2021). arXiv: 2110.10074 [astro-ph.HE].

[14] Serguei Chatrchyan et al. "Observation of a New Boson at a Mass of 125 GeV with the CMS Experiment at the LHC". In: *Phys. Lett. B* 716 (2012), pp. 30–61. DOI: 10.1016/j.physletb.2012.08.021. arXiv: 1207.7235 [hep-ex].

[15] Georges Aad et al. "Observation of a new particle in the search for the Standard Model Higgs boson with the ATLAS detector at the LHC". In: *Phys. Lett. B* 716 (2012), pp. 1–29. DOI: 10.1016/j.physletb.2012.08.020. arXiv: 1207.7214 [hep-ex].

[16] Peter Minkowski. "$\mu \to e\gamma$ at a Rate of One Out of 10^9 Muon Decays?" In: *Phys. Lett. B* 67 (1977), pp. 421–428. DOI: 10.1016/0370-2693(77)90435-X.

[17] Takehiko Asaka, Steve Blanchet, and Mikhail Shaposhnikov. "The nuMSM, dark matter and neutrino masses". In: *Phys. Lett. B* 631 (2005), pp. 151–156. DOI: 10.1016/j.physletb.2005.09.070. arXiv: hep-ph/0503065.

[18] Gianfranco Bertone, Dan Hooper, and Joseph Silk. "Particle dark matter: Evidence, candidates and constraints". In: *Phys. Rept.* 405 (2005), pp. 279–390. DOI: 10.1016/j.physrep.2004.08.031. arXiv: hep-ph/0404175.

[19] P. J. E. Peebles and Bharat Ratra. "The Cosmological Constant and Dark Energy". In: *Rev. Mod. Phys.* 75 (2003). Ed. by Jong-Ping Hsu and D. Fine, pp. 559–606. DOI: 10.1103/RevModPhys.75.559. arXiv: astro-ph/0207347.

[20] Steven Weinberg. "The Cosmological Constant Problem". In: *Rev. Mod. Phys.* 61 (1989). Ed. by Jong-Ping Hsu and D. Fine, pp. 1–23. DOI: 10.1103/RevModPhys.61.1.

[21] H. Georgi, Helen R. Quinn, and Steven Weinberg. "Hierarchy of Interactions in Unified Gauge Theories". In: *Phys. Rev. Lett.* 33 (1974), pp. 451–454. DOI: 10.1103/PhysRevLett.33.451.

[22] Giuseppe Degrassi et al. "Higgs mass and vacuum stability in the Standard Model at NNLO". In: *JHEP* 08 (2012), p. 098. DOI: 10.1007/JHEP08(2012)098. arXiv: 1205.6497 [hep-ph].

[23] Stephen P. Martin. "A Supersymmetry primer". In: *Adv. Ser. Direct. High Energy Phys.* 18 (1998). Ed. by Gordon L. Kane, pp. 1–98. DOI: 10.1142/9789812839657_0001. arXiv: hep-ph/9709356.

[24] Asimina Arvanitaki et al. "String Axiverse". In: *Phys. Rev. D* 81 (2010), p. 123530. DOI: 10.1103/PhysRevD.81.123530. arXiv: 0905.4720 [hep-th].

[25] Daniel Baumann, Horng Sheng Chia, and Rafael A. Porto. "Probing Ultralight Bosons with Binary Black Holes". In: *Phys. Rev. D* 99.4 (2019), p. 044001. DOI: 10.1103/PhysRevD.99.044001. arXiv: 1804.03208 [gr-qc].

[26] Daniel Baumann et al. "Gravitational Collider Physics". In: *Phys. Rev. D* 101.8 (2020), p. 083019. DOI: 10.1103/PhysRevD.101.083019. arXiv: 1912.04932 [gr-qc].

[27] Daniel Baumann et al. "Ionization of gravitational atoms". In: *Phys. Rev. D* 105.11 (2022), p. 115036. DOI: 10.1103/PhysRevD.105.115036. arXiv: 2112.14777 [gr-qc].

[28] Mateja Boskovic, Matthias Koschnitzke, and Rafael A. Porto. "In preparation". In: ().

[29] Bernard Carr et al. "Constraints on primordial black holes". In: *Rept. Prog. Phys.* 84.11 (2021), p. 116902. DOI: 10.1088/1361-6633/ac1e31. arXiv: 2002.12778 [astro-ph.CO].

[30] Bernard Carr and Florian Kuhnel. "Primordial Black Holes as Dark Matter: Recent Developments". In: *Ann. Rev. Nucl. Part. Sci.* 70 (2020), pp. 355–394. DOI: 10.1146/annurev-nucl-050520-125911. arXiv: 2006.02838 [astro-ph.CO].

[31] S. W. Hawking. "Particle Creation by Black Holes". In: *Commun. Math. Phys.* 43 (1975). Ed. by G. W. Gibbons and S. W. Hawking. [Erratum: Commun.Math.Phys. 46, 206 (1976)], pp. 199–220. DOI: 10.1007/BF02345020.

[32] Steven L. Detweiler. "KLEIN-GORDON EQUATION AND ROTATING BLACK HOLES". In: *Phys. Rev. D* 22 (1980), pp. 2323–2326. DOI: 10.1103/PhysRevD.22.2323.

[33] Paulo B. Ferraz, Thomas W. Kephart, and João G. Rosa. "Superradiant pion clouds around primordial black holes". In: *JCAP* 07.07 (2022), p. 026. DOI: 10.1088/1475-7516/2022/07/026. arXiv: 2004.11303 [gr-qc].

[34] John Preskill, Mark B. Wise, and Frank Wilczek. "Cosmology of the Invisible Axion". In: *Phys. Lett. B* 120 (1983). Ed. by M. A. Srednicki, pp. 127–132. DOI: 10.1016/0370-2693(83)90637-8.

[35] L. F. Abbott and P. Sikivie. "A Cosmological Bound on the Invisible Axion". In: *Phys. Lett. B* 120 (1983). Ed. by M. A. Srednicki, pp. 133–136. DOI: 10.1016/0370-2693(83)90638-X.

[36] Michael Dine and Willy Fischler. "The Not So Harmless Axion". In: *Phys. Lett. B* 120 (1983). Ed. by M. A. Srednicki, pp. 137–141. DOI: 10.1016/0370-2693(83)90639-1.

[37] Asimina Arvanitaki and Sergei Dubovsky. "Exploring the String Axiverse with Precision Black Hole Physics". In: *Phys. Rev. D* 83 (2011), p. 044026. DOI: 10.1103/PhysRevD.83.044026. arXiv: 1004.3558 [hep-th].

[38] Gerard 't Hooft. "Symmetry Breaking Through Bell-Jackiw Anomalies". In: *Phys. Rev. Lett.* 37 (1976). Ed. by Mikhail A. Shifman, pp. 8–11. DOI: 10.1103/PhysRevLett.37.8.

[39] Gerard 't Hooft. "Computation of the Quantum Effects Due to a Four-Dimensional Pseudoparticle". In: *Phys. Rev. D* 14 (1976). Ed. by Mikhail A. Shifman. [Erratum: Phys.Rev.D 18, 2199 (1978)], pp. 3432–3450. DOI: 10.1103/PhysRevD.14.3432.

[40] R. J. Crewther et al. "Chiral Estimate of the Electric Dipole Moment of the Neutron in Quantum Chromodynamics". In: *Phys. Lett. B* 88 (1979). [Erratum: Phys.Lett.B 91, 487 (1980)], p. 123. DOI: 10.1016/0370-2693(79)90128-X.

[41] C. A. Baker et al. "An Improved experimental limit on the electric dipole moment of the neutron". In: *Phys. Rev. Lett.* 97 (2006), p. 131801. DOI: 10.1103/PhysRevLett.97.131801. arXiv: hep-ex/0602020.

[42] R. D. Peccei and Helen R. Quinn. "CP Conservation in the Presence of Instantons". In: *Phys. Rev. Lett.* 38 (1977), pp. 1440–1443. DOI: 10.1103/PhysRevLett.38.1440.

[43] Frank Wilczek. "Problem of Strong P and T Invariance in the Presence of Instantons". In: *Phys. Rev. Lett.* 40 (1978), pp. 279–282. DOI: 10.1103/PhysRevLett.40.279.

[44] Steven Weinberg. "A New Light Boson?" In: *Phys. Rev. Lett.* 40 (1978), pp. 223–226. DOI: 10.1103/PhysRevLett.40.223.

[45] F. Englert and R. Brout. "Broken Symmetry and the Mass of Gauge Vector Mesons". In: *Phys. Rev. Lett.* 13 (1964). Ed. by J. C. Taylor, pp. 321–323. DOI: 10.1103/PhysRevLett.13.321.

[46] Peter W. Higgs. "Broken Symmetries and the Masses of Gauge Bosons". In: *Phys. Rev. Lett.* 13 (1964). Ed. by J. C. Taylor, pp. 508–509. DOI: 10.1103/PhysRevLett.13.508.

[47] David J. E. Marsh. "Axion Cosmology". In: *Phys. Rept.* 643 (2016), pp. 1–79. DOI: 10.1016/j.physrep.2016.06.005. arXiv: 1510.07633 [astro-ph.CO].

[48] R. D. Peccei. "The Strong CP problem and axions". In: *Lect. Notes Phys.* 741 (2008). Ed. by Markus Kuster, Georg Raffelt, and Berta Beltran, pp. 3–17. DOI: 10.1007/978-3-540-73518-2_1. arXiv: hep-ph/0607268.

[49] Jihn E. Kim. "Weak Interaction Singlet and Strong CP Invariance". In: *Phys. Rev. Lett.* 43 (1979), p. 103. DOI: 10.1103/PhysRevLett.43.103.

[50] Mikhail A. Shifman, A. I. Vainshtein, and Valentin I. Zakharov. "Can Confinement Ensure Natural CP Invariance of Strong Interactions?" In: *Nucl. Phys. B* 166 (1980), pp. 493–506. DOI: 10.1016/0550-3213(80)90209-6.

[51] Michael Dine, Willy Fischler, and Mark Srednicki. "A Simple Solution to the Strong CP Problem with a Harmless Axion". In: *Phys. Lett. B* 104 (1981), pp. 199–202. DOI: 10.1016/0370-2693(81)90590-6.

[52] A. R. Zhitnitsky. "On Possible Suppression of the Axion Hadron Interactions. (In Russian)". In: *Sov. J. Nucl. Phys.* 31 (1980), p. 260.

[53] Andreas Ringwald. "Exploring the Role of Axions and Other WISPs in the Dark Universe". In: *Phys. Dark Univ.* 1 (2012), pp. 116–135. DOI: 10.1016/j.dark.2012.10.008. arXiv: 1210.5081 [hep-ph].

[54] Anson Hook. "TASI Lectures on the Strong CP Problem and Axions". In: *PoS* TASI2018 (2019), p. 004. arXiv: 1812.02669 [hep-ph].

[55] Michael B. Green, J. H. Schwarz, and Edward Witten. "Superstring Theory. Vol.2: Loop Amplitudes, Anomalies and Phenomenology". Cambridge Monographs on Mathematical Physics. July 1988. ISBN: 978-0-521-35753-1.

[56] Michael B. Green, J. H. Schwarz, and Edward Witten. "Superstring Theory. Vol.1: Introduction". Cambridge Monographs on Mathematical Physics. July 1988. ISBN: 978-0-521-35752-4.

[57] John H. Schwarz. "Lectures on superstring and M theory dualities: Given at ICTP Spring School and at TASI Summer School". In: *Nucl. Phys. B Proc. Suppl.* 55 (1997). Ed. by C. Efthimiou and B. Greene, pp. 1–32. DOI: 10.1016/S0920-5632(97)00070-4. arXiv: hep-th/9607201.

[58] P. Candelas et al. "Vacuum Configurations for Superstrings". In: *Nucl. Phys. B* 258 (1985), pp. 46–74. DOI: 10.1016/0550-3213(85)90602-9.

[59] K. Becker, M. Becker, and J. H. Schwarz. "String theory and M-theory: A modern introduction". Cambridge University Press, Dec. 2006. ISBN: 978-0-511-25486-4, 978-0-521-86069-7.

[60] Th. Kaluza. "Zum Unitätsproblem der Physik". In: *Sitzungsber. Preuss. Akad. Wiss. Berlin (Math. Phys.)* 1921 (1921), pp. 966–972. DOI: 10.1142/S0218271818700017. arXiv: 1803.08616 [physics.hist-ph].

[61] Oskar Klein. "Quantum Theory and Five-Dimensional Theory of Relativity. (In German and English)". In: *Z. Phys.* 37 (1926). Ed. by J. C. Taylor, pp. 895–906. DOI: 10.1007/BF01397481.

[62] Liam McAllister, Eva Silverstein, and Alexander Westphal. "Gravity Waves and Linear Inflation from Axion Monodromy". In: *Phys. Rev. D* 82 (2010), p. 046003. DOI: 10.1103/PhysRevD.82.046003. arXiv: 0808.0706 [hep-th].

[63] Liam McAllister et al. "Runaway Relaxion Monodromy". In: *JHEP* 02 (2018), p. 124. DOI: 10.1007/JHEP02(2018)124. arXiv: 1610.05320 [hep-th].

[64] Peter Svrcek and Edward Witten. "Axions In String Theory". In: *JHEP* 06 (2006), p. 051. DOI: 10.1088/1126-6708/2006/06/051. arXiv: hep-th/0605206.

[65] Michele Cicoli, Mark Goodsell, and Andreas Ringwald. "The type IIB string axiverse and its low-energy phenomenology". In: *JHEP* 10 (2012), p. 146. DOI: 10.1007/JHEP10(2012)146. arXiv: 1206.0819 [hep-th].

[66] Nima Arkani-Hamed et al. "The String landscape, black holes and gravity as the weakest force". In: *JHEP* 06 (2007), p. 060. DOI: 10.1088/1126-6708/2007/06/060. arXiv: hep-th/0601001.

[67] Edward Witten. "Some Properties of O(32) Superstrings". In: *Phys. Lett. B* 149 (1984), pp. 351–356. DOI: 10.1016/0370-2693(84)90422-2.

[68] Joseph P. Conlon. "The QCD axion and moduli stabilisation". In: *JHEP* 05 (2006), p. 078. DOI: 10.1088/1126-6708/2006/05/078. arXiv: hep-th/0602233.

[69] Mehmet Demirtas et al. "The Kreuzer-Skarke Axiverse". In: *JHEP* 04 (2020), p. 138. DOI: 10.1007/JHEP04(2020)138. arXiv: 1808.01282 [hep-th].

[70] Viraf M. Mehta et al. "Superradiance in string theory". In: *JCAP* 07 (2021), p. 033. DOI: 10.1088/1475-7516/2021/07/033. arXiv: 2103.06812 [hep-th].

[71] R. Penrose and R. M. Floyd. "Extraction of rotational energy from a black hole". In: *Nature* 229 (1971), pp. 177–179. DOI: 10.1038/physci229177a0.

[72] Ya. B. Zel'Dovich. "Generation of Waves by a Rotating Body". In: *Soviet Journal of Experimental and Theoretical Physics Letters* 14 (Aug. 1971), p. 180.

[73] Ya. B. Zel'Dovich. "Amplification of Cylindrical Electromagnetic Waves Reflected from a Rotating Body". In: *Soviet Journal of Experimental and Theoretical Physics* 35 (Jan. 1972), p. 1085.

[74] William H. Press and Saul A. Teukolsky. "Floating Orbits, Superradiant Scattering and the Black-hole Bomb". In: *Nature* 238 (1972), pp. 211–212. DOI: 10.1038/238211a0.

[75] A. A. Starobinsky. "Amplification of waves reflected from a rotating "black hole"." In: *Sov. Phys. JETP* 37.1 (1973), pp. 28–32.

[76] Sam R. Dolan. "Instability of the massive Klein-Gordon field on the Kerr spacetime". In: *Phys. Rev. D* 76 (2007), p. 084001. DOI: 10.1103/PhysRevD.76.084001. arXiv: 0705.2880 [gr-qc].

[77] William E. East. "Massive Boson Superradiant Instability of Black Holes: Nonlinear Growth, Saturation, and Gravitational Radiation". In: *Phys. Rev. Lett.* 121.13 (2018), p. 131104. DOI: 10.1103/PhysRevLett.121.131104. arXiv: 1807.00043 [gr-qc].

[78] Paolo Pani et al. "Black hole bombs and photon mass bounds". In: *Phys. Rev. Lett.* 109 (2012), p. 131102. DOI: 10.1103/PhysRevLett.109.131102. arXiv: 1209.0465 [gr-qc].

[79] K. Belczynski et al. "Evolutionary roads leading to low effective spins, high black hole masses, and O1/O2 rates for LIGO/Virgo binary black holes". In: *Astron. Astrophys.* 636 (2020), A104. DOI: 10.1051/0004-6361/201936528. arXiv: 1706.07053 [astro-ph.HE].

[80] Masha Baryakhtar, Robert Lasenby, and Mae Teo. "Black Hole Superradiance Signatures of Ultralight Vectors". In: *Phys. Rev. D* 96.3 (2017), p. 035019. DOI: 10.1103/PhysRevD.96.035019. arXiv: 1704.05081 [hep-ph].

[81] William E. East and Frans Pretorius. "Superradiant Instability and Backreaction of Massive Vector Fields around Kerr Black Holes". In: *Phys. Rev. Lett.* 119.4 (2017), p. 041101. DOI: 10.1103/PhysRevLett.119.041101. arXiv: 1704.04791 [gr-qc].

[82] Nils Siemonsen and William E. East. "Gravitational wave signatures of ultralight vector bosons from black hole superradiance". In: *Phys. Rev. D* 101.2 (2020), p. 024019. DOI: 10.1103/PhysRevD.101.024019. arXiv: 1910.09476 [gr-qc].

[83] Daniel Baumann et al. "The Spectra of Gravitational Atoms". In: *JCAP* 12 (2019), p. 006. DOI: 10.1088/1475-7516/2019/12/006. arXiv: 1908.10370 [gr-qc].

[84] Nils Siemonsen et al. "Dark photon superradiance: Electrodynamics and multimessenger signals". In: *Phys. Rev. D* 107.7 (2023), p. 075025. DOI: 10.1103/PhysRevD.107.075025. arXiv: 2212.09772 [astro-ph.HE].

[85] William E. East. "Superradiant instability of massive vector fields around spinning black holes in the relativistic regime". In: *Phys. Rev. D* 96.2 (2017), p. 024004. DOI: 10.1103/PhysRevD.96.024004. arXiv: 1705.01544 [gr-qc].

[86] William E. East and Nils Siemonsen. "Instability and backreaction of massive spin-2 fields around black holes". In: *Phys. Rev. D* 108.12 (2023), p. 124048. DOI: 10.1103/PhysRevD.108.124048. arXiv: 2309.05096 [gr-qc].

[87] Richard Brito, Vitor Cardoso, and Paolo Pani. "Superradiance: New Frontiers in Black Hole Physics". In: *Lect. Notes Phys.* 906 (2015), pp.1–237. DOI: 10.1007/978-3-319-19000-6. arXiv: 1501.06570 [gr-qc].

[88] Asimina Arvanitaki, Masha Baryakhtar, and Xinlu Huang. "Discovering the QCD Axion with Black Holes and Gravitational Waves". In: *Phys. Rev. D* 91.8 (2015), p. 084011. DOI: 10.1103/PhysRevD.91.084011. arXiv: 1411.2263 [hep-ph].

[89] Masha Baryakhtar et al. "Black hole superradiance of self-interacting scalar fields". In: *Phys. Rev. D* 103.9 (2021), p. 095019. DOI: 10.1103/PhysRevD.103.095019. arXiv: 2011.11646 [hep-ph].

[90] Horng Sheng Chia et al. "Self-interacting gravitational atoms in the strong-gravity regime". In: *JCAP* 04 (2023), p. 018. DOI: 10.1088/1475-7516/2023/04/018. arXiv: 2212.11948 [gr-qc].

[91] Hidetoshi Omiya et al. "Impact of multiple modes on the evolution of self-interacting axion condensate around rotating black holes". In: *JCAP* 06 (2023), p. 016. DOI: 10.1088/1475-7516/2023/06/016. arXiv: 2211.01949 [gr-qc].

[92] Samuel J. Witte and Andrew Mummery. "Stepping Up Superradiance Constraints on Axions". In: (Dec. 2024). arXiv: 2412.03655 [hep-ph].

[93] Andrei Gruzinov. "Black Hole Spindown by Light Bosons". In: (Apr. 2016). arXiv: 1604.06422 [astro-ph.HE].

[94] Hirotaka Yoshino and Hideo Kodama. "The bosenova and axiverse". In: *Class. Quant. Grav.* 32.21 (2015), p. 214001. DOI: 10.1088/0264-9381/32/21/214001. arXiv: 1505.00714 [gr-qc].

[95] Mateja Boskovic et al. "Axionic instabilities and new black hole solutions". In: *Phys. Rev. D* 99.3 (2019), p. 035006. DOI: 10.1103/PhysRevD.99.035006. arXiv: 1811.04945 [gr-qc].

[96] Taishi Ikeda, Richard Brito, and Vitor Cardoso. "Blasts of Light from Axions". In: *Phys. Rev. Lett.* 122.8 (2019), p. 081101. DOI: 10.1103/PhysRevLett.122.081101. arXiv: 1811.04950 [gr-qc].

[97] João G. Rosa and Thomas W. Kephart. "Stimulated Axion Decay in Superradiant Clouds around Primordial Black Holes". In: *Phys. Rev. Lett.* 120.23 (2018), p. 231102. DOI: 10.1103/PhysRevLett.120.231102. arXiv: 1709.06581 [gr-qc].

[98] Thomas F. M. Spieksma et al. "Superradiance: Axionic couplings and plasma effects". In: *Phys. Rev. D* 108.6 (2023), p. 063013. DOI: 10.1103/PhysRevD.108.063013. arXiv: 2306.16447 [gr-qc].

[99] Yifan Chen, Xiao Xue, and Vitor Cardoso. "Black Holes as Neutrino Factories". In: (Aug. 2023). arXiv: 2308.00741 [hep-ph].

[100] Albert Einstein. "The Field Equations of Gravitation". In: *Sitzungsber. Preuss. Akad. Wiss. Berlin (Math. Phys.)* 1915 (1915), pp. 844–847.

[101] Karl Schwarzschild. "On the gravitational field of a mass point according to Einstein's theory". In: *Sitzungsber. Preuss. Akad. Wiss. Berlin (Math. Phys.)* 1916 (1916), pp. 189–196. arXiv: physics/9905030.

[102] Roy P. Kerr. "Gravitational field of a spinning mass as an example of algebraically special metrics". In: *Phys. Rev. Lett.* 11 (1963), pp. 237–238. DOI: 10.1103/PhysRevLett.11.237.

[103] David L. Wiltshire, Matt Visser, and Susan M. Scott. "The Kerr spacetime: Rotating black holes in general relativity". Cambridge University Press, Jan. 2009. ISBN: 978-0-521-88512-6.

[104] Robert H. Boyer and Richard W. Lindquist. "Maximal analytic extension of the Kerr metric". In: *J. Math. Phys.* 8 (1967), p. 265. DOI: 10.1063/1.1705193.

[105] R. Penrose. "Gravitational collapse: The role of general relativity". In: *Riv. Nuovo Cim.* 1 (1969), pp. 252–276. DOI: 10.1023/A:1016578408204.

[106] James M. Bardeen, B. Carter, and S. W. Hawking. "The Four laws of black hole mechanics". In: *Commun. Math. Phys.* 31 (1973), pp. 161–170. DOI: 10.1007/BF01645742.

[107] Jun John Sakurai and Jim Napolitano. "Modern Quantum Mechanics". 3rd ed. Quantum physics, quantum information and quantum computation. Cambridge University Press, Oct. 2020. ISBN: 978-0-8053-8291-4, 978-1-108-52742-2, 978-1-108-58728-0. DOI: 10.1017/9781108587280.

[108] T. J. M. Zouros and D. M. Eardley. "INSTABILITIES OF MASSIVE SCALAR PERTURBATIONS OF A ROTATING BLACK HOLE". In: *Annals Phys.* 118 (1979), pp. 139–155. DOI: 10.1016/0003-4916(79)90237-9.

[109] Lam Hui et al. "Black hole superradiance with dark matter accretion". In: *Phys. Rev. D* 107.10 (2023), p. 104018. DOI: 10.1103/PhysRevD.107.104018. arXiv: 2208.06408 [gr-qc].

[110] Ken K. Y. Ng et al. "Constraints on Ultralight Scalar Bosons within Black Hole Spin Measurements from the LIGO-Virgo GWTC-2". In: *Phys. Rev. Lett.* 126.15 (2021), p. 151102. DOI: 10.1103/PhysRevLett.126.151102. arXiv: 2011.06010 [gr-qc].

[111] Jeffrey E. McClintock, Ramesh Narayan, and James F. Steiner. "Black Hole Spin via Continuum Fitting and the Role of Spin in Powering Transient Jets". In: *Space Sci. Rev.* 183 (2014), pp. 295–322. DOI: 10.1007/s11214-013-0003-9. arXiv: 1303.1583 [astro-ph.HE].

[112] R. R. Ross and A. C. Fabian. "A Comprehensive range of x-ray ionized reflection models". In: *Mon. Not. Roy. Astron. Soc.* 358 (2005), pp. 211–216. DOI: 10.1111/j.1365-2966.2005.08797.x. arXiv: astro-ph/0501116.

[113] Andrzej A. Zdziarski et al. "What Is the Black Hole Spin in Cyg X-1?" In: *Astrophys. J. Lett.* 967.1 (2024), p. L9. DOI: 10.3847/2041-8213/ad43ed. arXiv: 2402.12325 [astro-ph.HE].

[114] R. Abbott et al. "Population of Merging Compact Binaries Inferred Using Gravitational Waves through GWTC-3". In: *Phys. Rev. X* 13.1 (2023), p. 011048. DOI: 10.1103/PhysRevX.13.011048. arXiv: 2111.03634 [astro-ph.HE].

[115] R. Abbott et al. "GWTC-3: Compact Binary Coalescences Observed by LIGO and Virgo during the Second Part of the Third Observing Run". In: *Phys. Rev. X* 13.4 (2023), p. 041039. DOI: 10.1103/PhysRevX.13.041039. arXiv: 2111.03606 [gr-qc].

[116] Jenny E. Greene, Jay Strader, and Luis C. Ho. "Intermediate-Mass Black Holes". In: *Ann. Rev. Astron. Astrophys.* 58 (2020), pp. 257–312. DOI: 10.1146/annurev-astro-032620-021835. arXiv: 1911.09678 [astro-ph.GA].

[117] Hirotaka Yoshino and Hideo Kodama. "Gravitational radiation from an axion cloud around a black hole: Superradiant phase". In: *PTEP* 2014 (2014), 043E02. DOI: 10.1093/ptep/ptu029. arXiv: 1312.2326 [gr-qc].

[118] Cristiano Palomba et al. "Direct constraints on ultra-light boson mass from searches for continuous gravitational waves". In: *Phys. Rev. Lett.* 123 (2019), p. 171101. DOI: 10.1103/PhysRevLett.123.171101. arXiv: 1909.08854 [astro-ph.HE].

[119] Sylvia J. Zhu et al. "Characterizing the continuous gravitational-wave signal from boson clouds around Galactic isolated black holes". In: *Phys. Rev. D* 102.6 (2020), p. 063020. DOI: 10.1103/PhysRevD.102.063020. arXiv: 2003.03359 [gr-qc].

[120] Richard Brito et al. "Gravitational wave searches for ultralight bosons with LIGO and LISA". In: *Phys. Rev. D* 96.6 (2017), p. 064050. DOI: 10.1103/PhysRevD.96.064050. arXiv: 1706.06311 [gr-qc].

[121] Asimina Arvanitaki et al. "Black Hole Mergers and the QCD Axion at Advanced LIGO". In: *Phys. Rev. D* 95.4 (2017), p. 043001. DOI: 10.1103/PhysRevD.95.043001. arXiv: 1604.03958 [hep-ph].

[122] Richard Brito et al. "Stochastic and resolvable gravitational waves from ultralight bosons". In: *Phys. Rev. Lett.* 119.13 (2017), p. 131101. DOI: 10.1103/PhysRevLett.119.131101. arXiv: 1706.05097 [gr-qc].

[123] Michele Maggiore. "Gravitational Waves. Vol. 1: Theory and Experiments". Oxford University Press, 2007. ISBN: 978-0-19-171766-6, 978-0-19-852074-0. DOI: 10.1093/acprof:oso/9780198570745.001.0001.

[124] Albert Einstein. "Explanation of the Perihelion Motion of Mercury from the General Theory of Relativity". In: *Sitzungsber. Preuss. Akad. Wiss. Berlin (Math. Phys.)* 1915 (1915), pp. 831–839.

[125] P. C. Peters and J. Mathews. "Gravitational radiation from point masses in a Keplerian orbit". In: *Phys. Rev.* 131 (1963), pp. 435–439. DOI: 10.1103/PhysRev.131.435.

[126] P. C. Peters. "Gravitational Radiation and the Motion of Two Point Masses". In: *Phys. Rev.* 136 (1964), B1224–B1232. DOI: 10.1103/PhysRev.136.B1224.

[127] Krzysztof Belczynski, Vassiliki Kalogera, and Tomasz Bulik. "A Comprehensive study of binary compact objects as gravitational wave sources: Evolutionary channels, rates, and physical properties". In: *Astrophys. J.* 572 (2001), pp. 407–431. DOI: 10.1086/340304. arXiv: astro-ph/0111452.

[128] I. Kowalska et al. "The eccentricity distribution of compact binaries". In: *Astronomy & Astrophysics* 527 (Jan. 2011), A70. ISSN: 1432-0746. DOI: 10.1051/0004-6361/201015777. URL: http://dx.doi.org/10.1051/0004-6361/201015777.

[129] Katelyn Breivik et al. "Distinguishing Between Formation Channels for Binary Black Holes with LISA". In: *Astrophys. J. Lett.* 830.1 (2016), p. L18. DOI: 10.3847/2041-8205/830/1/L18. arXiv: 1606.09558 [astro-ph.GA].

[130] Atsushi Nishizawa et al. "eLISA eccentricity measurements as tracers of binary black hole formation". In: *Phys. Rev. D* 94.6 (2016), p. 064020. DOI: 10.1103/PhysRevD.94.064020. arXiv: 1605.01341 [gr-qc].

[131] Atsushi Nishizawa et al. "Constraining stellar binary black hole formation scenarios with eLISA eccentricity measurements". In: *Mon. Not. Roy. Astron. Soc.* 465.4 (2017), pp. 4375–4380. DOI: 10.1093/mnras/stw2993. arXiv: 1606.09295 [astro-ph.HE].

[132] Carl L. Rodriguez et al. "Illuminating Black Hole Binary Formation Channels with Spins in Advanced LIGO". In: *Astrophys. J. Lett.* 832.1 (2016), p. L2. DOI: 10.3847/2041-8205/832/1/L2. arXiv: 1609.05916 [astro-ph.HE].

[133] Carl L. Rodriguez et al. "Post-Newtonian Dynamics in Dense Star Clusters: Highly-Eccentric, Highly-Spinning, and Repeated Binary Black Hole Mergers". In: *Phys. Rev. Lett.* 120.15 (2018), p. 151101. DOI: 10.1103/PhysRevLett.120.151101. arXiv: 1712.04937 [astro-ph.HE].

[134] Carl L. Rodriguez et al. "Post-Newtonian Dynamics in Dense Star Clusters: Formation, Masses, and Merger Rates of Highly-Eccentric Black Hole Binaries". In: *Phys. Rev. D* 98.12 (2018), p. 123005. DOI: 10.1103/PhysRevD.98.123005. arXiv: 1811.04926 [astro-ph.HE].

[135] Marcus E. Lower et al. "Measuring eccentricity in binary black hole inspirals with gravitational waves". In: *Phys. Rev. D* 98.8 (2018), p. 083028. DOI: 10.1103/PhysRevD.98.083028. arXiv: 1806.05350 [astro-ph.HE].

[136] Lisa Randall and Zhong-Zhi Xianyu. "Eccentricity without Measuring Eccentricity: Discriminating among Stellar Mass Black Hole Binary Formation Channels". In: *Astrophys. J.* 914.2 (2021), p. 75. DOI: 10.3847/1538-4357/abfd2c. arXiv: 1907.02283 [astro-ph.HE].

[137] Xiao Fang, Todd A. Thompson, and Christopher M. Hirata. "The Population of Eccentric Binary Black Holes: Implications for mHz Gravitational Wave Experiments". In: *Astrophys. J.* 875.1 (2019), p. 75. DOI: 10.3847/1538-4357/ab0e6a. arXiv: 1901.05092 [astro-ph.HE].

[138] Isobel M. Romero-Shaw et al. "GW190521: orbital eccentricity and signatures of dynamical formation in a binary black hole merger signal". In: *Astrophys. J. Lett.* 903.1 (2020), p. L5. DOI: 10.3847/2041-8213/abbe26. arXiv: 2009.04771 [astro-ph.HE].

[139] Manuel Arca Sedda. "Dissecting the properties of neutron star - black hole mergers originating in dense star clusters". In: *Commun. Phys.* 3 (2020), p. 43. DOI: 10.1038/s42005-020-0310-x. arXiv: 2003.02279 [astro-ph.GA].

[140] Hila Glanz and Hagai B. Perets. "Common envelope evolution of eccentric binaries". In: *Monthly Notices of the Royal Astronomical Society* 507.2 (Oct. 2021), pp. 2659–2670. DOI: 10.1093/mnras/stab2291. arXiv: 2105.02227 [astro-ph.SR].

[141] Michael Zevin et al. "Implications of Eccentric Observations on Binary Black Hole Formation Channels". In: *Astrophys. J. Lett.* 921.2 (2021), p. L43. DOI: 10.3847/2041-8213/ac32dc. arXiv: 2106.09042 [astro-ph.HE].

[142] Alessia Gualandris et al. "Eccentricity evolution of massive black hole binaries from formation to coalescence". In: *Monthly Notices of the Royal Astronomical Society* 511.4 (Jan. 2022), 4753–4765. ISSN: 1365-2966. DOI: 10.1093/mnras/stac241. URL: http://dx.doi.org/10.1093/mnras/stac241.

[143] Mudit Garg et al. "The minimum measurable eccentricity from gravitational waves of LISA massive black hole binaries". In: (July 2023). arXiv: 2307.13367 [astro-ph.GA].

[144] Pankaj Saini. "Resolving the eccentricity of stellar mass binary black holes with next generation ground-based gravitational wave detectors". In: (Aug. 2023). DOI: 10.1093/mnras/stae037. arXiv: 2308.07565 [astro-ph.HE].

[145] Rahul Dhurkunde and Alexander H. Nitz. "Search for eccentric NSBH and BNS mergers in the third observing run of Advanced LIGO and Virgo". In: (Oct. 2023). arXiv: 2311.00242 [astro-ph.HE].

[146] F. Acernese et al. "Advanced Virgo: a second-generation interferometric gravitational wave detector". In: *Class. Quant. Grav.* 32.2 (2015), p. 024001. DOI: 10.1088/0264-9381/32/2/024001. arXiv: 1408.3978 [gr-qc].

[147] T. Akutsu et al. "Overview of KAGRA: Detector design and construction history". In: *PTEP* 2021.5 (2021), 05A101. DOI: 10.1093/ptep/ptaa125. arXiv: 2005.05574 [physics.ins-det].

[148] Gabriella Agazie et al. "The NANOGrav 15 yr Data Set: Evidence for a Gravitational-wave Background". In: *Astrophys. J. Lett.* 951.1 (2023), p. L8. DOI: 10.3847/2041-8213/acdac6. arXiv: 2306.16213 [astro-ph.HE].

[149] R. Cole. "Gwplotter". 2019. URL: https://github.com/robsci/GWplotter/tree/master.

[150] L. Landau. "Zur Theorie der Energieubertragung. II". 1932. URL: https://cir.nii.ac.jp/crid/1370290617742844819.

[151] Clarence Zener. "Nonadiabatic crossing of energy levels". In: *Proc. Roy. Soc. Lond. A* 137 (1932), pp. 696–702. DOI: 10.1098/rspa.1932.0165.

[152] Daniel Baumann et al. "Sharp Signals of Boson Clouds in Black Hole Binary Inspirals". In: *Phys. Rev. Lett.* 128.22 (2022), p. 221102. DOI: 10.1103/PhysRevLett.128.221102. arXiv: 2206.01212 [gr-qc].

[153] Giovanni Maria Tomaselli, Thomas F. M. Spieksma, and Gianfranco Bertone. "Dynamical friction in gravitational atoms". In: *JCAP* 07 (2023), p. 070. DOI: 10.1088/1475-7516/2023/07/070. arXiv: 2305.15460 [gr-qc].

[154] Giovanni Maria Tomaselli, Thomas F. M. Spieksma, and Gianfranco Bertone. "The resonant history of gravitational atoms in black hole binaries". In: (Mar. 2024). arXiv: 2403.03147 [gr-qc].

[155] Xi Tong, Yi Wang, and Hui-Yu Zhu. "Termination of superradiance from a binary companion". In: *Phys. Rev. D* 106.4 (2022), p. 043002. DOI: 10.1103/PhysRevD.106.043002. arXiv: 2205.10527 [gr-qc].

[156] Steven L. Detweiler and Eric Poisson. "Low multipole contributions to the gravitational selfforce". In: *Phys. Rev. D* 69 (2004), p. 084019. DOI: 10.1103/PhysRevD.69.084019. arXiv: gr-qc/0312010.

[157] Richard Brito and Shreya Shah. "Extreme mass-ratio inspirals into black holes surrounded by scalar clouds". In: *Phys. Rev. D* 108.8 (2023), p. 084019. DOI: 10.1103/PhysRevD.108.084019. arXiv: 2307.16093 [gr-qc].

[158] Francisco Duque et al. "Extreme-Mass-Ratio Inspirals in Ultralight Dark Matter". In: *Phys. Rev. Lett.* 133.12 (2024), p. 121404. DOI: 10.1103/PhysRevLett.133.121404. arXiv: 2312.06767 [gr-qc].

[159] Emanuele Berti et al. "Ultralight boson cloud depletion in binary systems". In: *Phys. Rev. D* 99.10 (2019), p. 104039. DOI: 10.1103/PhysRevD.99.104039. arXiv: 1904.03131 [gr-qc].

[160] Takuya Takahashi, Hidetoshi Omiya, and Takahiro Tanaka. "Evolution of binary systems accompanying axion clouds in extreme mass ratio inspirals". In: *Phys. Rev. D* 107.10 (2023), p. 103020. DOI: 10.1103/PhysRevD.107.103020. arXiv: 2301.13213 [gr-qc].

[161] V. M. Akulin and W. P. Schleich. "Landau-Zener transition to a decaying level". In: *Phys. Rev. A* 46 (7 1992), pp. 4110–4113. DOI: 10.1103/PhysRevA.46.4110. URL: https://link.aps.org/doi/10.1103/PhysRevA.46.4110.

[162] Takuya Takahashi, Hidetoshi Omiya, and Takahiro Tanaka. "Axion cloud evaporation during inspiral of black hole binaries: The effects of backreaction and radiation". In: *PTEP* 2022.4 (2022), 043E01. DOI: 10.1093/ptep/ptac044. arXiv: 2112.05774 [gr-qc].

[163] Giuseppe Ficarra, Paolo Pani, and Helvi Witek. "Impact of multiple modes on the black-hole superradiant instability". In: *Phys. Rev. D* 99.10 (2019), p. 104019. DOI: 10.1103/PhysRevD.99.104019. arXiv: 1812.02758 [gr-qc].

[164] Richard Brito, Vitor Cardoso, and Paolo Pani. "Black holes as particle detectors: evolution of superradiant instabilities". In: *Class. Quant. Grav.* 32.13 (2015), p. 134001. DOI: 10.1088/0264-9381/32/13/134001. arXiv: 1411.0686 [gr-qc].

[165] Nils Siemonsen, Taillte May, and William E. East. "Modeling the black hole superradiance gravitational waveform". In: *Phys. Rev. D* 107.10 (2023), p. 104003. DOI: 10.1103/PhysRevD.107.104003. arXiv: 2211.03845 [gr-qc].

[166] N. V. Vitanov and S. Stenholm. "Pulsed excitation of a transition to a decaying level". In: 55.4 (Apr. 1997), pp. 2982–2988. DOI: 10.1103/PhysRevA.55.2982.

[167] N. V. Vitanov. "Transition times in the Landau-Zener model". In: *Phys. Rev. A* 59 (1999), p. 988. DOI: 10.1103/PhysRevA.59.988. arXiv: quant-ph/9811066.

[168] Wolfram Research, Inc. "Mathematica, Version 13.2". Champaign, IL, 2022. URL: https://www.wolfram.com/mathematica.

[169] Yan Cao and Yong Tang. "Signatures of ultralight bosons in compact binary inspiral and outspiral". In: *Phys. Rev. D* 108.12 (2023), p. 123017. DOI: 10.1103/PhysRevD.108.123017. arXiv: 2307.05181 [gr-qc].

[170] Linqing Wen. "On the eccentricity distribution of coalescing black hole binaries driven by the Kozai mechanism in globular clusters". In: *Astrophys. J.* 598 (2003), pp. 419–430. DOI: 10.1086/378794. arXiv: astro-ph/0211492.

[171] Giovanni Maria Tomaselli, Thomas F. M. Spieksma, and Gianfranco Bertone. "Legacy of Boson Clouds on Black Hole Binaries". In: *Phys. Rev. Lett.* 133.12 (2024), p. 121402. DOI: 10.1103/PhysRevLett.133.121402. arXiv: 2407.12908 [gr-qc].

[172] Kaiyuan Fan et al. "Modulating binary dynamics via the termination of black hole superradiance". In: *Phys. Rev. D* 109.2 (2024), p. 024059. DOI: 10.1103/PhysRevD.109.024059. arXiv: 2311.17013 [gr-qc].

[173] Conor Dyson et al. "Environmental effects in extreme mass ratio inspirals: perturbations to the environment in Kerr". In: (Jan. 2025). arXiv: 2501.09806 [gr-qc].

[174] Riccardo Della Monica and Richard Brito. "Detectability of gravitational atoms in black hole binaries with the Einstein Telescope". In: (Mar. 2025). arXiv: 2503.23419 [gr-qc].

[175] Walter D. Goldberger and Ira Z. Rothstein. "An Effective field theory of gravity for extended objects". In: *Phys. Rev. D* 73 (2006), p. 104029. DOI: 10.1103/PhysRevD.73.104029. arXiv: hep-th/0409156.

[176] Walter D. Goldberger and Ira Z. Rothstein. "Dissipative effects in the worldline approach to black hole dynamics". In: *Phys. Rev. D* 73 (2006), p. 104030. DOI: 10.1103/PhysRevD.73.104030. arXiv: hep-th/0511133.

[177] Walter D. Goldberger. "Effective Field Theory for Compact Binary Dynamics". In: (Dec. 2022). DOI: $10.1007/978-981-19-3079-9_2-1$. arXiv: 2212.06677 [hep-th].

[178] Rafael A. Porto. "Post-Newtonian corrections to the motion of spinning bodies in NRGR". In: *Phys. Rev. D* 73 (2006), p. 104031. DOI: 10.1103/PhysRevD.73.104031. arXiv: gr-qc/0511061.

[179] Rafael A. Porto. "Absorption effects due to spin in the worldline approach to black hole dynamics". In: *Phys. Rev. D* 77 (2008), p. 064026. DOI: 10.1103/PhysRevD.77.064026. arXiv: 0710.5150 [hep-th].

[180] Rafael A. Porto. "The effective field theorist's approach to gravitational dynamics". In: *Phys. Rept.* 633 (2016), pp. 1–104. DOI: 10.1016/j.physrep.2016.04.003. arXiv: 1601.04914 [hep-th].

[181] Walter D. Goldberger, Jingping Li, and Ira Z. Rothstein. "Non-conservative effects on spinning black holes from world-line effective field theory". In: *JHEP* 06 (2021), p. 053. DOI: 10.1007/JHEP06(2021)053. arXiv: 2012.14869 [hep-th].

[182] Scott Tremaine. "Dynamics of Planetary Systems". 2023.

[183] Michael A. Morrison and Gregory A. Parker. "A guide to rotations in quantum mechanics". In: *Australian Journal of Physics* 40 (Jan. 1987), p. 465. DOI: 10.1071/PH870465.

[184] Adrien Kuntz, Francesco Serra, and Enrico Trincherini. "Effective two-body approach to the hierarchical three-body problem". In: *Phys. Rev. D* 104.2 (2021), p. 024016. DOI: 10.1103/PhysRevD.104.024016. arXiv: 2104.13387 [hep-th].

[185] J. A. Burns. "Elementary derivation of the perturbation equations of celestial mechanics". In: *American Journal of Physics* 44.10 (Oct. 1976), pp. 944–949. DOI: 10.1119/1.10237.

[186] Theocharis A. Apostolatos et al. "Spin induced orbital precession and its modulation of the gravitational wave forms from merging binaries". In: *Phys. Rev. D* 49 (1994), pp. 6274–6297. DOI: 10.1103/PhysRevD.49.6274.

[187] Barton Zwiebach. "Mastering quantum mechanics: essentials, theory, and applications". 2022. URL: https://mitpress.mit.edu/9780262046138/mastering-quantum-mechanics/.

[188] Taishi Ikeda et al. "Black hole binaries and light fields: Gravitational molecules". In: *Phys. Rev. D* 103.2 (2021), p. 024020. DOI: 10.1103/PhysRevD.103.024020. arXiv: 2010.00008 [gr-qc].

[189] Vitor Cardoso, Francisco Duque, and Taishi Ikeda. "Tidal effects and disruption in superradiant clouds: a numerical investigation". In: *Phys. Rev. D* 101.6 (2020), p. 064054. DOI: 10.1103/PhysRevD.101.064054. arXiv: 2001.01729 [gr-qc].

[190] Josu C. Aurrekoetxea et al. "Effect of Wave Dark Matter on Equal Mass Black Hole Mergers". In: *Phys. Rev. Lett.* 132.21 (2024), p. 211401. DOI: 10.1103/PhysRevLett.132.211401. arXiv: 2311.18156 [gr-qc].

[191] S. Raghavan et al. "Coherent oscillations between two weakly coupled Bose-Einstein condensates: Josephson effects, π oscillations, and macroscopic quantum self-trapping". In: *Phys. Rev. A* 59 (1 1999), pp. 620–633. DOI: 10.1103/PhysRevA.59.620. URL: https://link.aps.org/doi/10.1103/PhysRevA.59.620.

[192] Bernard M. Nabet and Barak Kol. "Leading anomalies, the drift Hamiltonian and the relativistic two-body system". In: (Aug. 2014). arXiv: 1408.2628 [gr-qc].

[193] Thibault Damour, Achamveedu Gopakumar, and Bala R. Iyer. "Phasing of gravitational waves from inspiralling eccentric binaries". In: *Phys. Rev. D* 70 (2004), p. 064028. DOI: 10.1103/PhysRevD.70.064028. arXiv: gr-qc/0404128.

[194] Adam Pound and Eric Poisson. "Osculating orbits in Schwarzschild spacetime, with an application to extreme mass-ratio inspirals". In: *Phys. Rev. D* 77 (2008), p. 044013. DOI: 10.1103/PhysRevD.77.044013. arXiv: 0708.3033 [gr-qc].

[195] Giulia Fumagalli et al. "Non-adiabatic dynamics of eccentric black-hole binaries in post-Newtonian theory". In: (Feb. 2025). arXiv: 2502.06952 [gr-qc].

[196] Antonios Kyriazis and Fengwei Yang. "Gravitational Waves from Resonant Transitions of Tidally Perturbed Gravitational Atoms". In: (Mar. 2025). arXiv: 2503.18121 [hep-ph].

[197] Dmitry Budker et al. "A generic formation mechanism of ultralight dark matter solar halos". In: *JCAP* 12 (2023), p. 021. DOI: 10.1088/1475-7516/2023/12/021. arXiv: 2306.12477 [hep-ph].

[198] Majed Khalaf et al. "Boson Cloud Atlas: Direct Observation of Superradiance Clouds". In: (Aug. 2024). arXiv: 2408.16051 [astro-ph.CO].

[199] Richard P. Feynman, Frank L. Vernon Jr., and Robert W. Hellwarth. "Geometrical Representation of the Schrödinger Equation for Solving Maser Problems". In: *Journal of Applied Physics* 28.1 (Jan. 1957), pp. 49–52. DOI: 10.1063/1.1722572.

[200] N. V. Vitanov and B. M. Garraway. "Landau-Zener model: Effects of finite coupling duration". In: 53.6 (June 1996), pp. 4288–4304. DOI: 10.1103/PhysRevA.53.4288.

[201] Enrico Martello et al. "Coexistence of stable and unstable population dynamics in a nonlinear non-Hermitian mechanical dimer". In: 107.6, 064211 (June 2023), p. 064211. DOI: 10.1103/PhysRevE.107.064211. arXiv: 2302.03572 [cond-mat.mes-hall].

[202] Hyungjin Kim and Alessandro Lenoci. "work in progress". In: *work in progress* ().

[203] Lam Hui et al. "Ultralight scalars as cosmological dark matter". In: *Phys. Rev. D* 95.4 (2017), p. 043541. DOI: 10.1103/PhysRevD.95.043541. arXiv: 1610.08297 [astro-ph.CO].

[204] Lam Hui. "Wave Dark Matter". In: *Ann. Rev. Astron. Astrophys.* 59 (2021), pp. 247–289. DOI: 10.1146/annurev-astro-120920-010024. arXiv: 2101.11735 [astro-ph.CO].

[205] Taillte May, William E. East, and Nils Siemonsen. "Self-gravity effects of ultralight boson clouds formed by black hole superradiance". In: *Phys. Rev. D* 111.4 (2025), p. 044062. DOI: 10.1103/PhysRevD.111.044062. arXiv: 2410.21442 [gr-qc].

[206] Horng Sheng Chia and Thomas D. P. Edwards. "Searching for General Binary Inspirals with Gravitational Waves". In: *JCAP* 11 (2020), p. 033. DOI: 10.1088/1475-7516/2020/11/033. arXiv: 2004.06729 [astro-ph.HE].

[207] Boye Su, Zhong-Zhi Xianyu, and Xingyu Zhang. "Probing Ultralight Bosons with Compact Eccentric Binaries". In: *Astrophys. J.* 923.1 (2021), p. 114. DOI: 10.3847/1538-4357/ac2d91. arXiv: 2107.13527 [gr-qc].

[208] Horng Sheng Chia et al. "In Pursuit of Love: First Templated Search for Compact Objects with Large Tidal Deformabilities in the LIGO-Virgo Data". In: (May 2023). arXiv: 2306.00050 [gr-qc].

[209] Jeremy D. Schnittman. "Spin-orbit resonance and the evolution of compact binary systems". In: *Phys. Rev. D* 70 (2004), p. 124020. DOI: 10.1103/PhysRevD.70.124020. arXiv: astro-ph/0409174.

[210] Giulia Fumagalli and Davide Gerosa. "Spin-eccentricity interplay in merging binary black holes". In: *Phys. Rev. D* 108.12 (2023), p. 124055. DOI: 10.1103/PhysRevD.108.124055. arXiv: 2310.16893 [gr-qc].

[211] R. R. Allan and G. N. Ward. "Planetary equations in terms of vectorial elements". In: *Mathematical Proceedings of the Cambridge Philosophical Society* 59.3 (1963), 669–677. DOI: 10.1017/S0305004100037336.

[212] Chad R. Galley and Ira Z. Rothstein. "Deriving analytic solutions for compact binary inspirals without recourse to adiabatic approximations". In: *Phys. Rev. D* 95.10 (2017), p. 104054. DOI: 10.1103/PhysRevD.95.104054. arXiv: 1609.08268 [gr-qc].

[213] Pauli Virtanen et al. "SciPy 1.0: Fundamental Algorithms for Scientific Computing in Python". In: *Nature Methods* 17 (2020), pp. 261–272. DOI: 10.1038/s41592-019-0686-2.

[214] Charles R. Harris et al. "Array programming with NumPy". In: *Nature* 585.7825 (2020), pp. 357–362. DOI: 10.1038/s41586-020-2649-2. arXiv: 2006.10256 [cs.MS].